이학박사 학위논문

Atomic-Scale Study of Density of States Modulation on Cuprate Superconductor $Bi_2Sr_2CaCu_2O_{8+\delta}$

구리 초전도체 $Bi_2Sr_2CaCu_2O_{8+\delta}$의 상태 밀도 변조의 원자 단위 연구

2020년 2월

서울대학교 대학원

물리 · 천문 학부

이 경 석

Atomic-Scale Study of Density of States Modulation on Cuprate Superconductor $Bi_2Sr_2CaCu_2O_{8+\delta}$

지도교수 이 진 호

이 논문을 이학박사 학위 논문으로 제출함

2020년 2월

서울대학교 대학원
물리 · 천문 학부

이 경 석

이경석의 이학박사 학위 논문을 인준함

2019년 12월

Chair	김 기 훈	(Seal)
Vice Chair	이 진 호	(Seal)
Examiner	유 재 준	(Seal)
Examiner	최 석 봉	(Seal)
Examiner	정 창 욱	(Seal)

Abstract

The high-temperature superconductivity has been considered as an important research topic in condensed matter physics since its discovery in 1986. To obtain insight into the mechanism of the high-temperature superconductivity, I conducted spectroscopic imaging scanning tunneling microscopy (SI-STM) experiments while breaking the superconductivity. In this thesis, I will discuss two studies where the superconductivity is broken in different conditions.

First is the study in the magnetic field. I introduce SI-STM experiments on two different doping levels of $Bi_2Sr_2CaCu_2O_8$ on an atomic-scale under the magnetic fields in chapter 4. I found the particle-hole asymmetrically dispersing density of states modulation (DOSM) in vortices on the slightly underdoped $Bi_2Sr_2CaCu_2O_{8+\delta}$ and in the almost entire field of view of the highly underdoped $Bi_2Sr_2CaCu_2O_{8+\delta}$. Based on this observation, I suggest an alternative model of quantum oscillations (QO) in real space and explain QO using DOSM of $Bi_2Sr_2CaCu_2O_{8+\delta}$ to unify the results of the different experimental instruments in chapter 5.

Second is the study above the superconducting critical temperature. My SI-STM study on the highly underdoped $Bi_2Sr_2CaCu_2O_{8+\delta}$ in the pseudogap phase revealed a similar DOSM – comparable wavelength and energy-dependence – observed in the magnetic field experiments. Besides, DOSM above T_c has remarkable properties distinct from those of charge density wave (CDW) and usual quasiparticle interference (QPI) in the last chapter.

Keyword: high-temperature superconductor, the density of states modulation,

pseudogap, magnetic field (within 6 words)

Student Number: 2012-20377

Contents

List of Figures

List of Abbreviations

SI-STM	spectroscopic imaging scanning tunneling microscopy
ARPES	angle-resolved photoemission spectroscopy
ULV	ultra low vibration
LDOS	local density of states
PID	proportional–integral–derivative
FE	field emission
DOS	density of states
FT	Fourier transform
HDC	high-density concrete
BCS	Bardeen–Cooper–Schrieffer
LBCO	lanthanum barium copper oxide
YBCO	yttrium barium copper oxide
HBCCO	mercury barium calcium copper oxide
BSCCO	bismuth strontium calcium copper oxide
AFI	antiferromagnetic insulator
UD	underdoped
SUD	slightly underdoped
HUD	highly underdoped
OD	overdoped
PG	pseudogap
DOSM	density of states modulation
FOV	field of view
QO	quantum oscillations
LL	Landau level

CDW	charge density wave
PDW	pair density wave
QPI	quasiparticle interference
VR	vortex region
NVR	non-vortex region
AC	autocorrelation
ACR	autocorrelation in real space
ACF	autocorrelation using Fourier transform

Chapter 1.

Spectroscopic Imaging Scanning Tunneling Microscopy

Scanning tunneling microscopy (STM) is an instrument that can scan the surface of a material with atomic-scale resolution in various environments (not only in an ultra-high vacuum but in the liquid or gas state). STM has been one of the most effective and useful machines in condensed matter physics for nearly 40 years since Gerd Binnig and Heinrich Rohrer first invented it at IBM Zürich in 1981[1].

The two leading technologies of STM are the piezoelectric unit and quantum tunneling. The piezoelectric unit has made STM work in an atomic-scale. Also, it could control the tip-sample distance, which is exponentially sensitive to the tunneling current. Blocking all kinds of noise is crucial for successful STM experiments on an atomic-scale.

There are many kinds of STM depending on the objects being measured and the development environments. I have used spectroscopic imaging STM (SI-STM) operating at a low-temperature vacuum. In this chapter, I introduce the basic principles of SI-STM and the ultra-low vibration (ULV) system in Seoul national university.

1.1. Introduction

First, I introduce a basic SI-STM operating configuration (Fig. 1.1). SI-STM takes advantage of quantum tunneling, which is a quantum property that occurs when a sample and tip are close enough while applying the voltage between them. Since the order of the intensity of a tunneling current is as small as pA, a current pre-amplifier is needed. Besides, there is a feedback loop to maintain the tunneling current, varying on the distance of the tip and sample. The overall system of the SI-STM is controlled using an electronic computer unit (ECU). The tunneling current varying with the position of the tip on the sample surface provides information on the topography of the surface. At each point, I can obtain dI/dV by sweeping the tip-sample bias. Since dI/dV is proportional to the local density of states (LDOS) of the material at low energy, the electronic structure of the material can be imaged by SI-STM in real space.

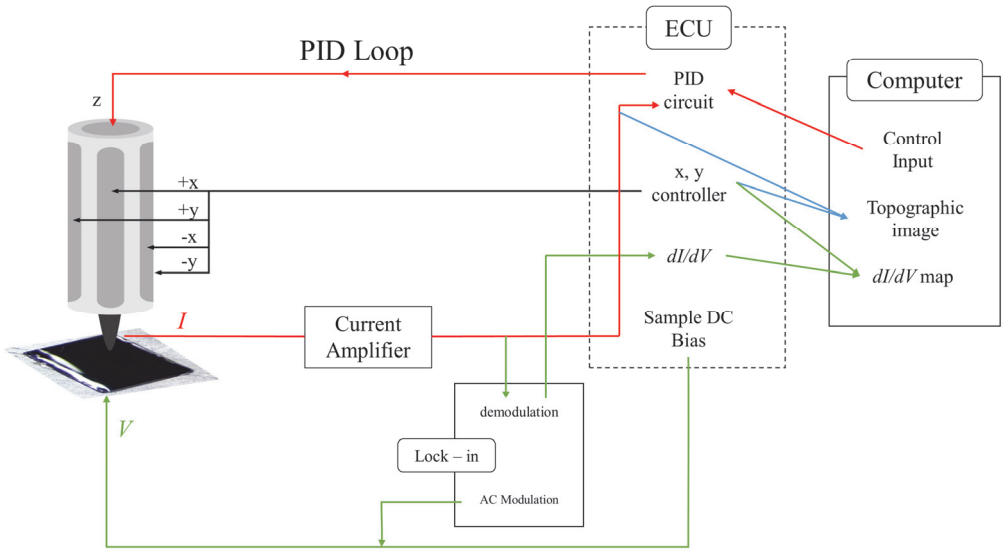

Figure 1.1: The schematic picture of an STM.

Proportional–integral–derivative (PID) loop is represented by red color, the loop for the topographic image by blue color, and the *dI/dV* image by green color.

1.2. Electron tunneling of an STM

In 1960, Ivar Giaever performed the first metal-superconductor junction tunneling experiment[2]. The junction used in this experiment was Metal (Al) – insulator (Al_2O_3) – superconductor (Pb) junction, and measuring temperature was below 7.2 K, a T_c of Pb. J. Bardeen solved this junction problem with two subsystems stationary Schrodinger equations and calculated the transmission rate of the electron using time-dependent perturbation theory. Bardeen's tunneling matrix element is written by

$$M_{\mu\nu} = -\frac{\hbar^2}{2m}\int_{z=z_0}\left[\psi_\mu\frac{\partial\chi_\nu}{\partial z} - \chi_\nu\frac{\partial\psi_\mu}{\partial z}\right]dxdy \quad \ldots \quad (1.2.1)$$

From the Bardeen's matrix form and with a bias voltage V between two electrodes, the tunneling current I is written by

$$I = \frac{4\pi e}{\hbar}\int_{-\infty}^{\infty}[f(E_F - eV + \varepsilon) - f(E_F + \varepsilon)] \times \rho_T(E_F - eV + \varepsilon)\rho_S(E_F + \varepsilon)|M|^2 d\varepsilon \quad \ldots \quad (1.2.2)$$

where $f(E)$ is the Fermi-Dirac distribution function, $\rho_{T(S)}$ is the density of states (DOS) of a tip (sample). Using the assumption that the matrix element does not vary significantly at low energy (high-temperature (high-T_c) superconducting gap = tens of meV), and using the matrix element of the *s*-wave tip by Tersoff and Hamann[3], then the tunneling matrix is written by

$$|M|^2 \propto \exp\left(-2\frac{\sqrt{2m\varphi}}{\hbar}z\right) \quad \ldots \quad (1.2.3)$$

where m is the electron mass, z is the distance between the tip and sample, and φ is the work function.

If the high field emission (FE) is performed to the tip, the surface of the tip is reconstructed that the DOS of the tip would be constant[4]. Therefore, the equation (1.2.2) is written by

$$I \propto \exp\left(-2\frac{\sqrt{2m\varphi}}{\hbar}z\right)\rho_T \int_0^{eV} \rho_S(E_F+\varepsilon)d\epsilon \quad \ldots \quad (1.2.4)$$

Differential conductance is the derivative of the given current with a voltage.

$$g(z,V) \;=\; \frac{dI}{dV}(z,V) \propto \exp\left(-2\frac{\sqrt{2m\varphi}}{\hbar}z\right)\rho_T\rho_S(eV) \quad \ldots \quad (1.2.5)$$

For fixed z and φ, a differential conductance is proportional to the LDOS of the sample.

1.3. Topography

There are two modes of topography measurement of STM. One is a constant height mode, and another is a constant current mode. The constant height mode holds the **z** value (the feedback loop is turned off) of the piezo tube while recording the current that varies according to the corrugation of the sample surface. If the amplitude of the sample surface corrugation is larger than the fixed tip-sample distance, the tip can crash. Therefore, this mode is only possible when the sample has a smooth surface within the few angstroms. According to the equation (1.2.4), the tunneling current *I* varies by the local work function. Thus it is difficult to image the quantitative topographic features. However, it has a strong point that the fast scan is possible since this mode of scanning is not with the feedback loop.

The constant current mode is a method to image topography with maintaining the tunneling current between the tip and sample constantly.

According to the equation (1.2.4), the tunneling current I exponentially depends on the tip-sample distance. Thus, the z-value of the tip changes by the surface corrugation (Tunneling current is an integration of DOS up to the applied sample voltage so that a constant current mode can be considered as the constant integrated of DOS). Since the current changes continuously according to the surface corrugation, the speed of the scan speed is limited by the bandwidth of the feedback circuit - typically kilohertz range.

1.4. Spectroscopy

The spectroscopy of STM is a very effective method to reveal the LDOS. At first, move the tip to the desired location and then set a certain tip-sample distance - fix the current I_s and voltage V_s. After that, turn off the feedback loop and sweep the bias range you want to measure. I can obtain the dI/dV value from the direct derivative of the measured I-V or using the lock-in method. The energy range could be selected from near the Fermi energy (0 meV) to several eV. STM can also measure dI/dV of the unoccupied state (the hole state) as well as the occupied state (the electron state).

1.4.1. Lock–in method

The lock-in technique is mainly used to obtain the dI/dV because the direct derivative of the measured I-V value is usually very noisy. The green loop in Fig. 1.1 shows the way of obtaining differential conductance to use the lock-in

method. First, add an alternating current (AC) modulation, which is smaller to the energy resolution you want to know, to the sample direct current (DC) bias ($V_s \rightarrow \ V_s + V_{ac}Cos(wt)$). To reduce the noise from the outside, I chose the modulation frequency of 937 Hz ($f = \frac{2\pi}{w}$), which is not generally used in electronics or communications. Then, I can expand measured tunneling current as follows,

$$I \ = \ I(V = V_s) \ + \ \frac{dI}{dV}Cos(wt) \ + O({V_{ac}}^2) \ \ldots \ (1.4.1)$$

By demodulating the measured current using the modulation frequency of 937 Hz, I can obtain the *dI/dV*. I used the Stanford SR830 lock-in amplifier.

1.4.2. Spectroscopic imaging

When scanning the sample using the STM tip, I can obtain the information about the topography and LDOS simultaneously (Fig. 1.2). At this time, using the collected topographic and spectroscopic information, I can research electronic structure with STM resolution, an order of Å. The measuring time of one-point spectroscopy is about 4-5s. Since usually one data set is 200 *x* 200 or 256 *x* 256 pixels, it takes about three to four days for obtaining one data set.

SI-STM is used for various studies because it can image the electronic structure in real space. The Fourier transform (FT) method to the obtained topographic or spectroscopic image is proper for studying the properties such as wavelength, correlation length of dominating modulation in real space. Charge density wave (CDW)[5,6] and quasiparticle interference (QPI) study[7–9] are

the representative research of the FT method. Due to the property that topographic and spectroscopic images can be imaged simultaneously, it is advantageous for the study of cuprates of local electronic structures such as impurity[10,11], vortex[12–14], dopant[15,16], and spatially inhomogeneous gap[17].

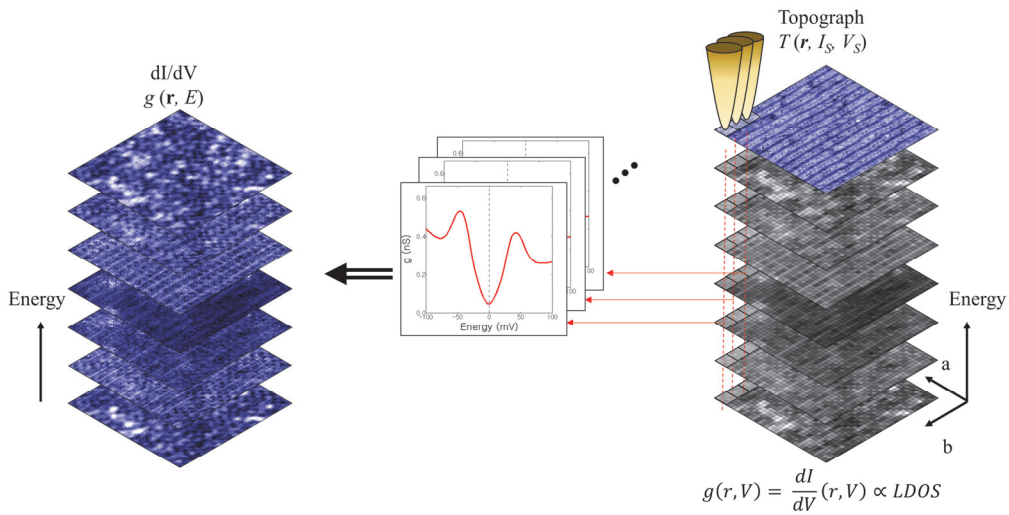

Figure 1.2: The schematic picture of an SI-STM.

As the tip moves through a specific area, it collects the electronic information of the point by sweeping the voltage. Based on the collected point spectra for each energy in the *x*-*y* plane, it is possible to make the topographic and electronic structures in real space simultaneously.

1.5. Set-up effect

The set-up effect comes from the point-dependent element that belongs to tunneling current *I* and *dI/dV*. From the definition of *I* and *g(=dI/dV)*,

$$I(\mathbf{r}, eV) = I_S \frac{\int_0^{eV} n(\mathbf{r}, \epsilon) d\epsilon}{\int_0^{eV_S} n(\mathbf{r}, \epsilon) d\epsilon} \quad \dots \quad (1.5.1)$$

$$g(\mathbf{r}, eV) = I_S \frac{n(\mathbf{r}, \epsilon)}{\int_0^{eV_S} n(\mathbf{r}, \epsilon) d\epsilon} \quad \dots \quad (1.5.2)$$

The denominator of $g(\mathbf{r}, eV)$ and $I(\mathbf{r}, eV)$, $\int_0^{eV_S} n(\mathbf{r}, \epsilon) d\epsilon$ is the point dependent element. This factor could make point-dependent modulation on the *I-V* and *dI/dV* images. Such modulation must be non-dispersive in energy.

1.6. Experimental Equipment

1.6.1. Ultra-low vibration laboratory

To obtain successful data, the condition of the tip must not change while measuring. Since the tunneling current is exponentially proportional to the tip-sample distance, blocking any source of the vibrations - mechanical and electrical - is very crucial for obtaining high-quality data. I built an ultra-low vibration (ULV) system for SI-STM at Seoul national university to minimize external influences during the measurement. Our ULV system is based on the

design of J. C. Seamus Davis laboratory at Brookhaven national laboratory, one of the world-class SI-STM laboratories. However, due to the small installation space, the design of our ULV room must be compact.

The configuration of the ULV room is in Fig. 1.3. First, six air springs are above a concrete base below 3 m underground. A high-density concrete (HDC) block with a central pit of 90 cm *x* 240 cm is placed on top of it. The liquid helium experimental Dewar goes up and down through this pit. On top of the HDC block, the acoustic room and the STM Frame (Frame leg + main table) are installed. Cryostat and Dewar connect to the main table. The main table is placed on three air springs on the top of the frame legs. The main table and frame leg are filled with lead shots to increase the mass of the system. The density of the HDC concrete block is 3.35t/m^3, and the total weight is about 24 tons. The contact between the STM and the outside of the ULV room is only by two stages of air springs, as shown in Fig. 1.3. The first one is the air spring under the HDC block, and the second one is between the frame leg and the main table. Experimental results of the vibration isolation effect of the ULV room are shown in Fig. 1.4. Two air springs reduce the vibration to an order of 10^{-2} and make the velocity spectral density of $1\,\mathrm{nm/s}\cdot\sqrt{Hz}$ enables the SI-STM experiment successfully.

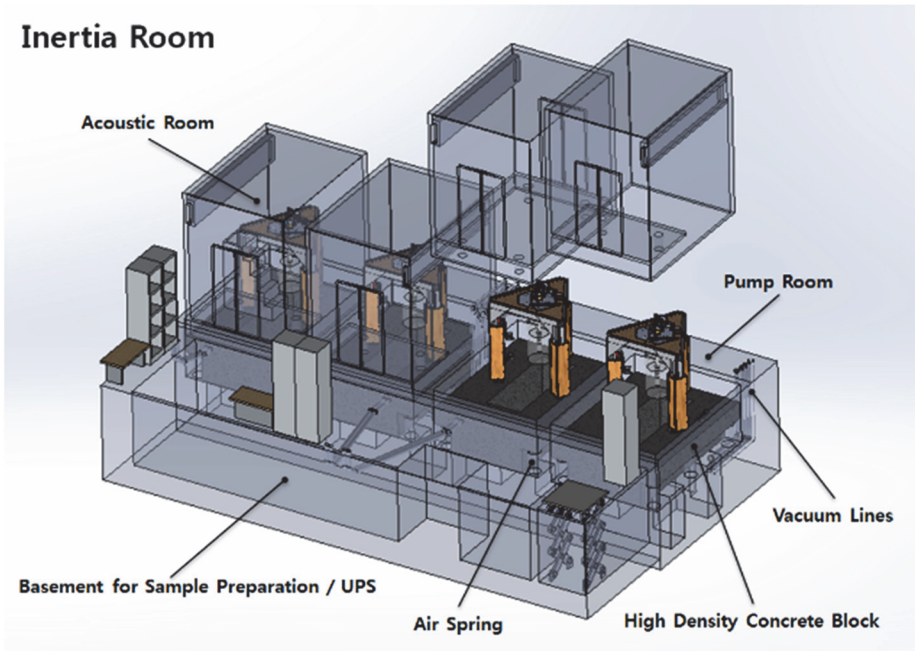

Figure 1.3: The drawing of the Seoul national university SI-STM laboratory.

There are two stages of air spring to block the vibration directly and acoustic room to block the vibration through the air.

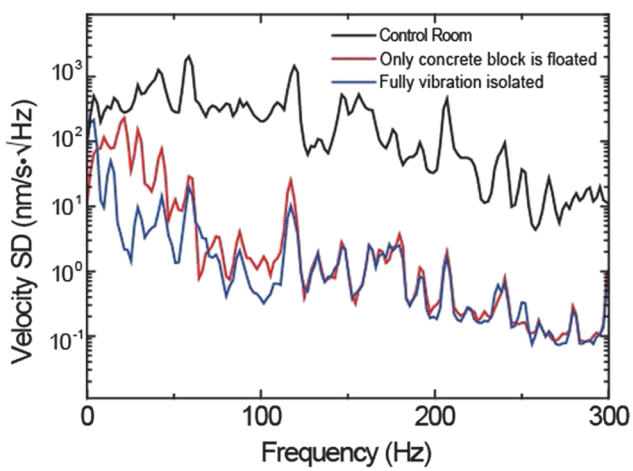

Figure 1.4: The measuring spectral density (SD) in the ULV room with and without air springs.

The black curve shows that none of the air spring is working. The red curve shows that

only the air spring of the concrete block is working. The blue curve shows that both air springs are working.

1.6.2. STM head

The STM experiment is conducted on the STM head. To obtain data in this thesis, I used a homemade STM head. The STM head is made based on a Pan-type STM head, which has a body with a tip holder of a triangular sapphire prism moving by two sets of three piezo walkers[18] The STM head has a rotator stage to make the tip treatment quickly (Fig. 1.5).

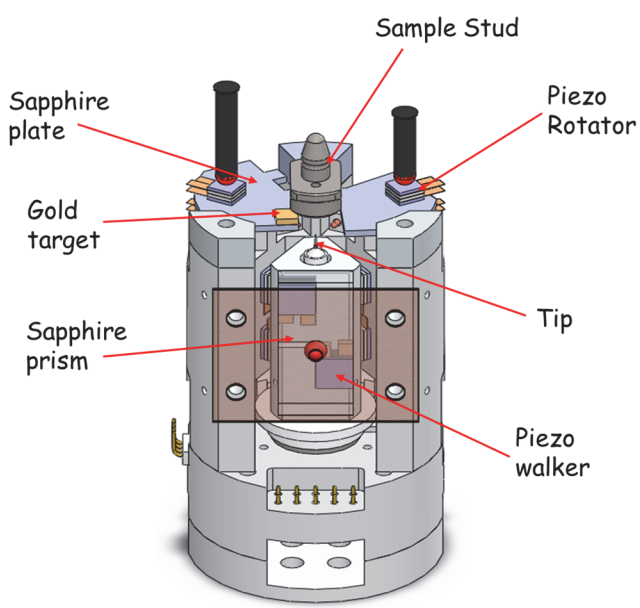

Figure 1.5: The drawing of the STM head.

The Pan-type STM head requires a long time to change the tip since warming up the system is the only way. Thus, it is essential for exchanging the tip *in-situ* in low temperatures to reduce the unnecessary time. Installing a gold stage for doing FE inside the head makes this possible.

Tip treatment processing is as follows. When the tip treatment is required, I rotate the gold-attached sapphire plate by applying the voltage to piezo rotators. After the plate is located between the sample stud and tip, I approach the tip to the gold and recover it with atomic resolution by doing high FE. If the tip achieves an atomic resolution, I withdraw the tip from the gold and return the sapphire plate to its original position. Then, I approach the tip to the sample and experiment again. It could reduce the time, about 24 hours, for tip treatment to three to four hours[19]. Besides, since there is no process of replacing the sample with the gold, tip treatment is possible while preserving the state when the sample cleaving is successful.

1.6.3. 14 T Superconducting magnet system

I used a 14 T superconducting magnet system of American magnetics, Inc. (AMI) for magnetic field experiments. The magnet system consists of two parts, liquid He Dewar and the superconducting magnet. The cryostat is inserted into Dewar, and the STM head in the cryostat is located in the magnet coil center. Figure 1.5 shows the schematic figure of a 14 T superconducting magnet system.

The operation of the superconducting magnet is as follows. The liquid He Dewar is precooled with liquid nitrogen. After draining the liquid nitrogen, Dewar is filled with liquid He to make the STM head and superconducting

magnet to the temperature of 4.2 K. When the temperature of the magnet reaches below the transition temperature, start the magnet operation. At first, turn on the heater of the magnet circuit to break the superconductivity. Next, use the magnet power supply to energize the magnet. When the current is reached to the target value, turn off the heater to make the magnet in persistent mode, and experiment.

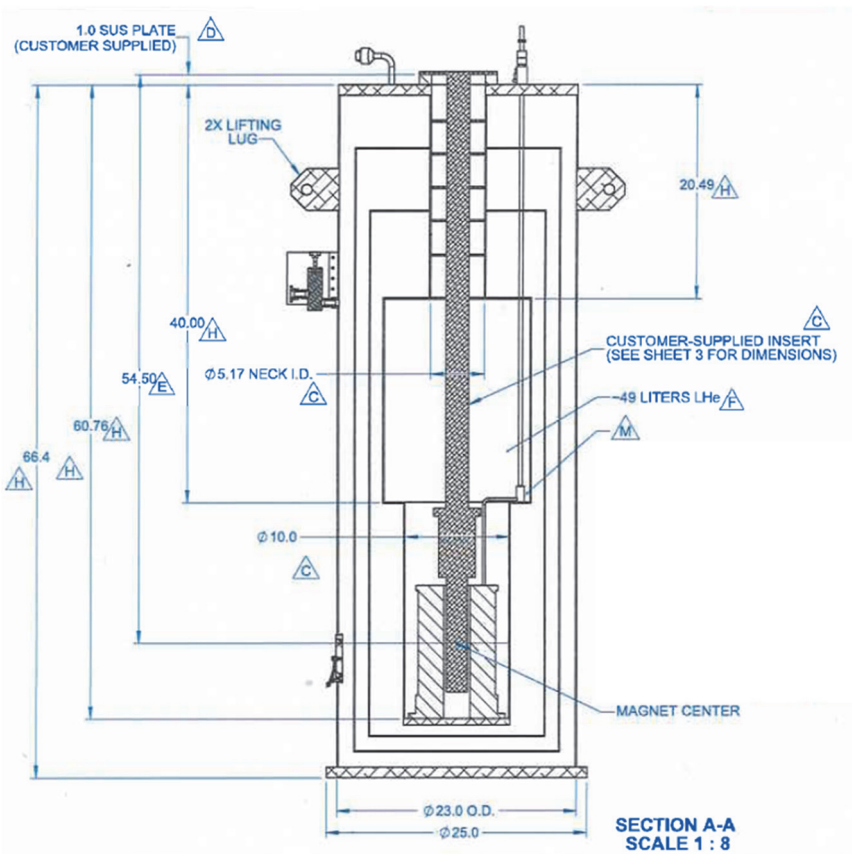

Figure 1.6: The drawing of 14 T superconducting magnet system.

During magnetic field experiments, the magnet must always be in liquid helium. Dewar could store about 50 liters of liquid helium in the belly, and it takes about one week for liquid helium to evaporate until above the magnet location.

Chapter 2.

Cuprate Superconductor: $Bi_2Sr_2CaCu_2O_{8+\delta}$

Superconductivity is a representative phenomenon in which quantum mechanical properties appear in the macroscopic world. Superconducting materials have two properties: Perfect conductivity and perfect diamagnetism (Fig 2.1). Superconductivity could be broken by raising the temperature above the critical temperature (T_c), applying an electric current above the critical current (J_c), or applying a magnetic field above the critical magnetic field (H_c).

Unlike conventional superconductors, which are well explained by the Bardeen–Cooper–Schrieffer (BCS) theory, high-T_c superconductors are not explained entirely by the single theory. Over thirty years later after its discovery, the principle of high-T_c superconductivity is still in the veil. In particular, cuprates are the first discovered materials and has the highest critical temperature

of high-T_c superconductors. One of the cuprates family, bismuth strontium calcium copper oxide (BSCCO), plays an essential role in surface physics due to its excellent cleaving property. In this thesis, I used a $Bi_2Sr_2CaCu_2O_{8+\delta}$ to conduct a study of the high-T_c superconductivity. In this chapter, I briefly introduce the research material $Bi_2Sr_2CaCu_2O_{8+\delta}$.

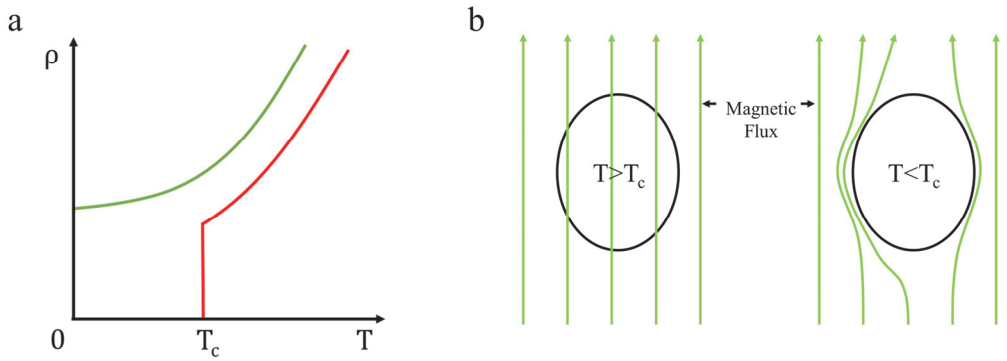

Figure 2.1: Properties of superconductors.

(a) Perfect conductivity (ρ=0), (b) Perfect diamagnetism (expel the magnetic flux totally).

2.1. History of superconductors

After Heike Kamerlingh Onnes discovered superconductivity in mercury after liquefying helium-4 in 1911[20], superconducting properties have been discovered in many pure metals. Nonetheless, the highest critical temperature of the materials was near 20 K of Nb_3Ge for nearly 70 years[21]. In 1986, a

significant rise in critical temperature was caused by Muller and Bednorz[22]. They found that lanthanum barium copper oxide (LBCO) has a very high T_c of 35 K, which is not explained by the BCS theory. A year later, M. K. Wu and Paul Chul's team found yttrium barium copper oxide (YBCO) with a T_c of 93 K[23]. A T_c of 154 K and 166 K was reported at 25 GPa in mercury barium calcium copper oxide (HBCCO)[24,25], and remains as the highest critical temperature of cuprates until 2019. In 2008, superconducting properties were also found in ferromagnetic iron-based compounds[26–28]. In these materials, when a single layer FeSe is grown on $SrTiO_3$[29], it shows 100 K of a T_c. Most recently, superconductivity was also found in bilayer graphene with a specific angle (called a magic anglV) between the top and bottom layers[30]. Moreover, it was found that H_2S and LaH_{10} above 100 GPa have a critical temperature of over 200 K[31,32].

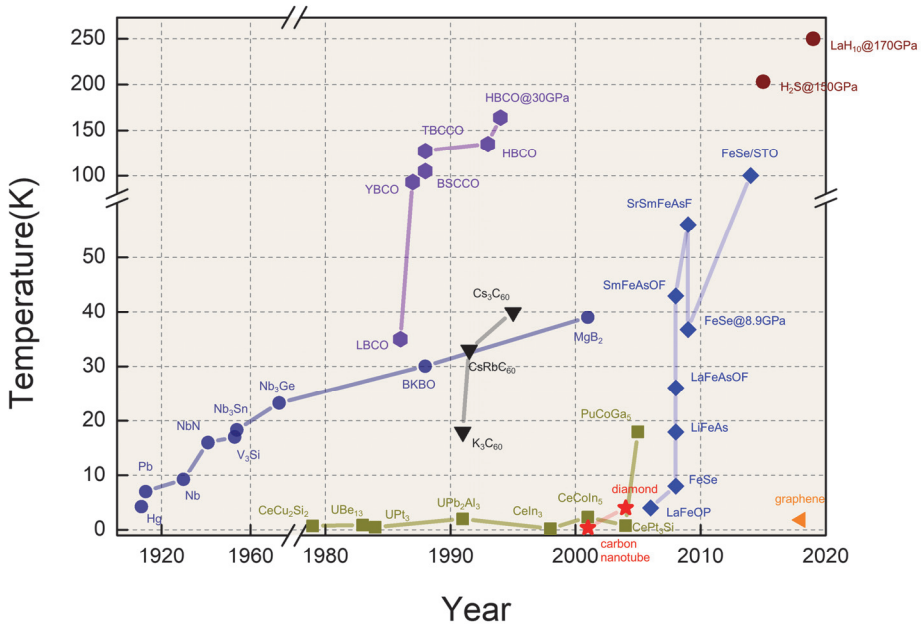

Figure 2.2: The history of superconductors.

The discovery year and transition temperature of representative superconductors are presented in the figure.

2.2. Cuprate superconductors

Cuprate superconductor is a type of high-T_c superconductors with one or more CuO_2 planes. Karl Alexander Müller and Johannes Georg Bednorz first discovered superconducting properties at LBCO and won the Nobel Prize in 1987[23]. Since then, superconducting properties have been reported in many other cuprates such as YBCO, TBCCO, and BSCCO[23,33,34].

The parent materials of the cuprates are antiferromagnetic Mott insulators

(AFI) (Fig. 2.3). Since its energy band is half-filled, it is supposed to be metal by the band theory, but it shows insulating properties. This is because of the strong repulsion force between electrons, which was ignored when the band calculation. The phase of cuprates varies by the hole-doping to the parent materials. If the hole density per Cu atom (p) of cuprates exceeds a certain value, cuprates become superconductors. It shows AFI up to p = 2 ~ 5 % and superconducting property from p = 5 ~ 10 % to p = 25 ~ 30 %. The superconducting critical temperature of hole-doped cuprates appears dome-like in the p-T phase diagram. T_c increases with doping until a certain value p = 18 ~ 20 % and decreases after this value. The value of p, where hole-doped cuprates shown the maximum T_c, is called optimal doping. In the range of the superconducting dome, the lower then the optimal doping level is called underdope (UD), and higher is called overdope (OD). Besides, in the region of approximately p < 20%, there is a novel phase called the pseudogap (PG), which has unusual electronic excitations below a specific temperature (T*). The doping dependence of T* is presented in Fig. 2.4 and, it is above the superconducting critical temperature in the underdoped range.

One of the main properties of cuprates superconductivity is the d-wave superconductor. The gap function of the d-wave superconductor has four-fold symmetry in **k** space, where the node has a maximum superconducting gap, and the anti-node has a zero-gap (Fig. 2.5).

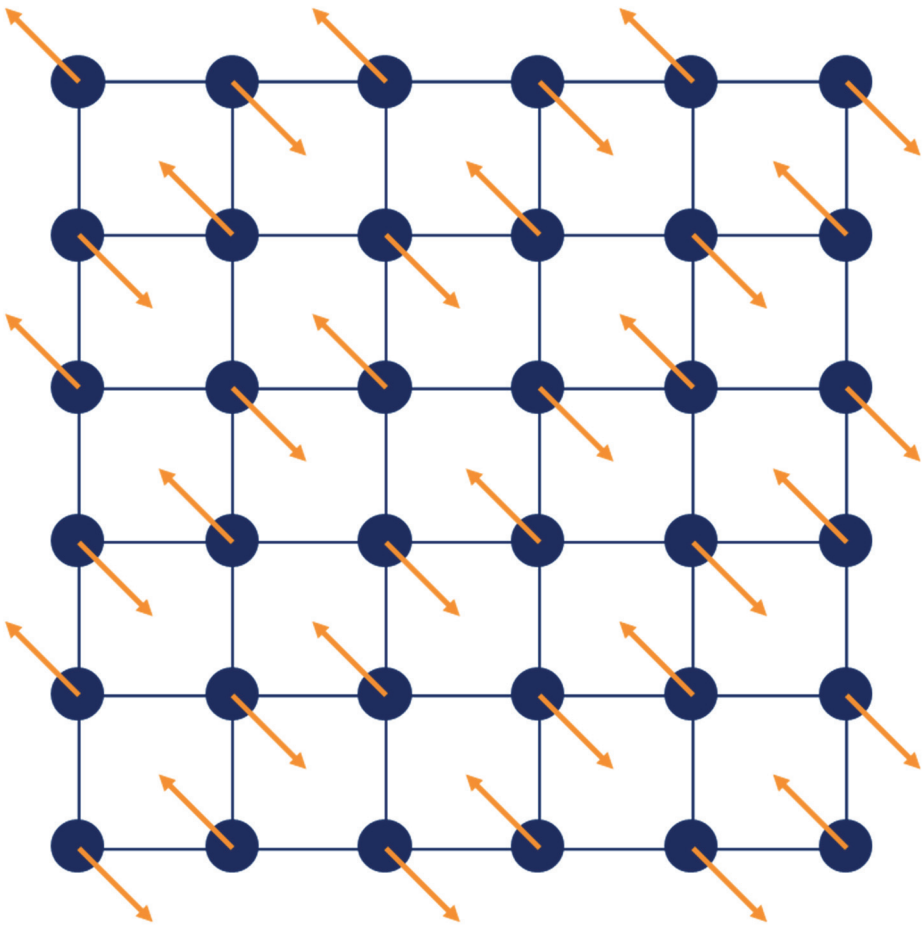

Figure 2.3: The picture of spins of AFI.

The spins (orange arrows) of atoms (navy circles) in the nearest neighbors are the opposite direction.

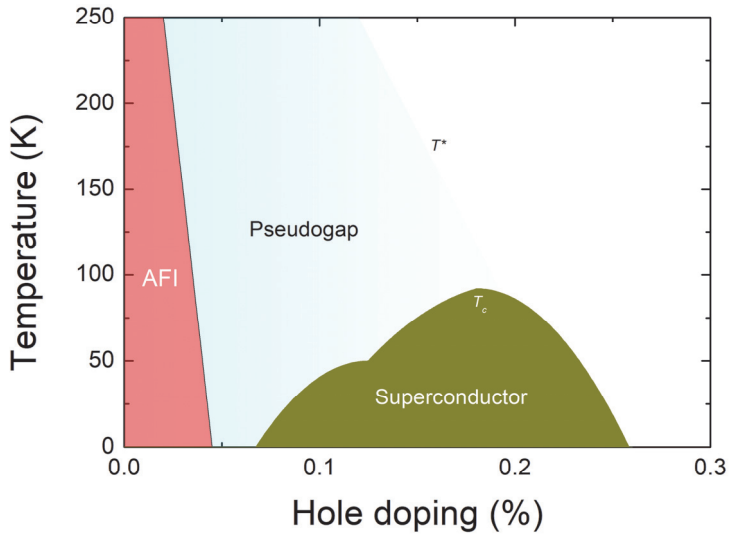

Figure 2.4: The doping (*p*) – temperature (*T*) phase diagram of hole-doped cuprates.

*T**: Pseudogap transition temperature, T_c: Superconducting transition temperature.

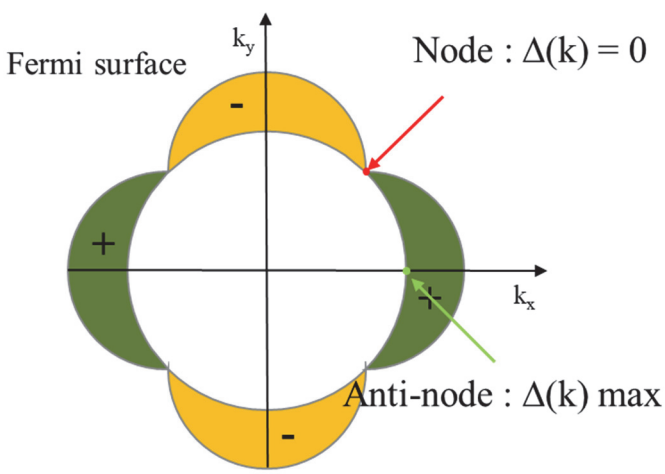

Figure 2.5: The Fermi surface of *d*-wave superconductors.

Yellow and green show the opposite signs of the order parameter of the d-wave superconductors. *Δ(k)* is a gap function in **k** space.

2.3. $Bi_2Sr_2CaCu_2O_{8+\delta}$

BSCCO is a type of cuprates having a perovskite structure. Its chemical formula is $Bi_2Sr_2Ca_{n-1}Cu_nO_{2n+4+\delta}$, the number *n* is determined by the number of CuO_2 plane per unit cell. Since the atomically flat surface of BSCCO is obtainable by *in-situ* cold cleaving, it is suitable for angle-resolved photoemission spectroscopy (ARPES) or STM, which are very sensitive to the sample surface. In general, the superconducting critical temperature increases as the number of CuO_2 planes increases (33 K for the $Bi_2Sr_2CuO_{6+\delta}$, 96 K for the $Bi_2Sr_2CaCu_2O_{8+\delta}$, and 108 K for the $Bi_2Sr_2Ca_2Cu_3O_{10+\delta}$). Due to the difficulty of synthesizing samples that have more CuO_2 planes, $Bi_2Sr_2CaCu_2O_{8+\delta}$ or $Bi_2Sr_2CuO_{6+\delta}$ are frequently used in experiments. The samples used in this thesis are $Bi_2Sr_2CaCu_2O_{8+\delta}$.

Hiroshi Maeda first discovered superconductivity in $Bi_2Sr_2CaCu_2O_{8+\delta}$ in 1998[35]. The crystal structure of $Bi_2Sr_2CaCu_2O_{8+\delta}$ is shown in Fig. 2.6. There are two ways to determine lattice constants of $Bi_2Sr_2CaCu_2O_{8+\delta}$ depending on the direction. The first way is to choose the *x* and *y* axes to the direction of the Cu-O-Cu bonding in the CuO_2 plane. With this orientation, the lattice constant is $x = y = 3.8$ Å. Another method is to hold *a* and *b* in the 45 degrees to the direction of the Cu-O-Cu bonding. In this case, $a = b = 5.4$ Å and the other lattice constant becomes c = 30.7 Å in perpendicular to the CuO_2 plane. In this thesis, the lattice constants of *x* and *y* are used, and the measuring direction of electron tunneling by STM is in the *c* direction.

When STM image the cleaved Bi-O plane of BSCCO, not only atoms but repeating horizontal lines in *b* direction are also observed. The atom is bismuth

not oxygen, which was well explained by Pb doped sample experiments[36]. The horizontal line is the supermodulation with a size of 26 Å approximately, which was first revealed by STM by Kirk *et al.* in 1988[37]. Since then, various models have been suggested to explain for supermodulation[38–40]. However, such models failed to explain the supermodulation entirely. This supermodulation is a structure-property that is strong enough to affect the superconducting gap[41].

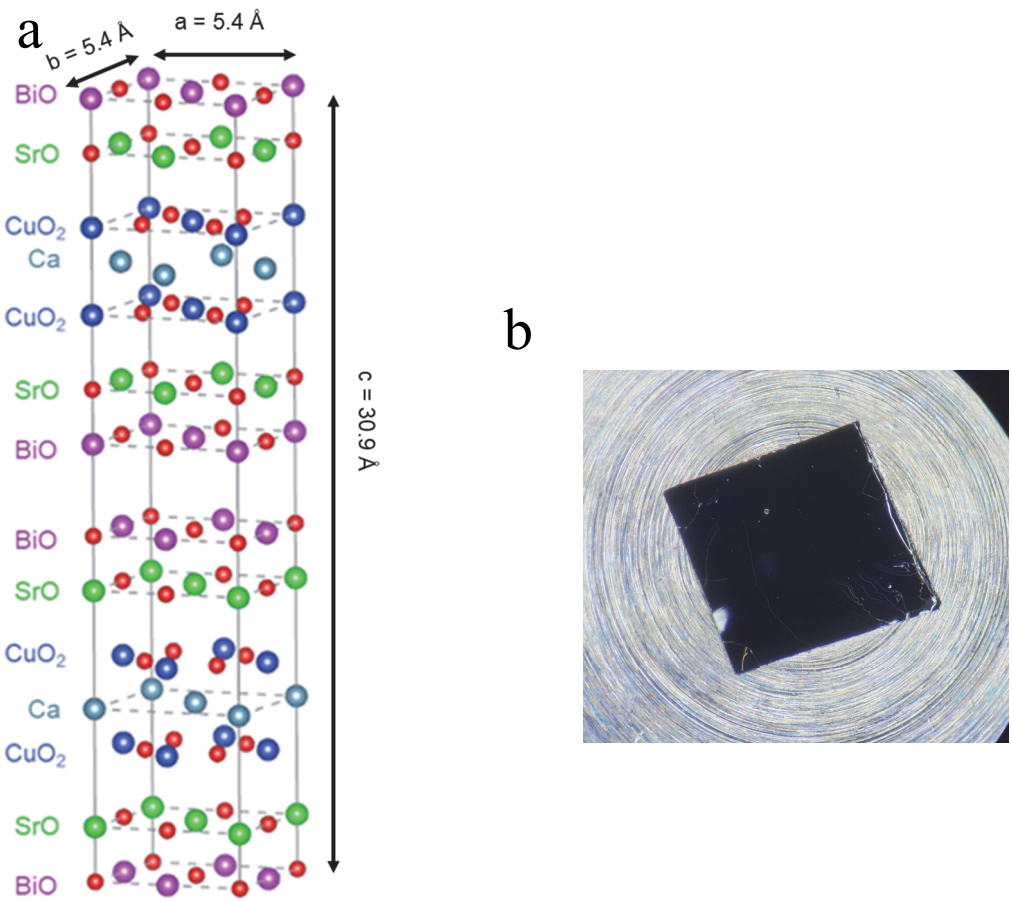

Figure 2.6: (a) An unit cell of $Bi_2Sr_2CaCu_2O_{8+\delta}$ and (b) cleaved $Bi_2Sr_2CaCu_2O_{8+\delta}$
Due to the weak bonding force between the Bi-O planes, the Bi-O plane (b) is exposed under *in-situ* cold cleaving.

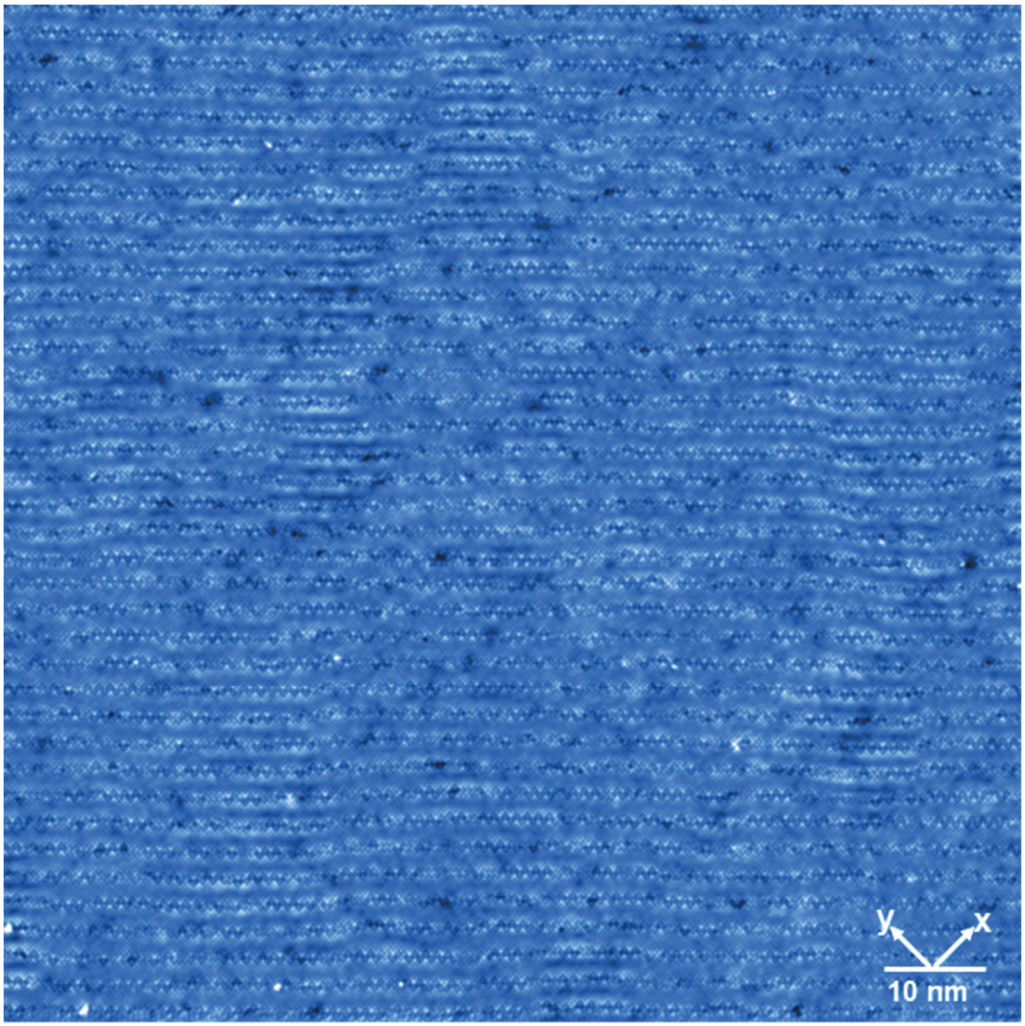

Figure 2.7: The topographic image of the Bi-O plane of $Bi_2Sr_2CaCu_2O_{8+\delta}$.

The horizontal lines with dollar signs are supermodulations. The size is 100 nm *x* 100 nm with 512 *x* 512 pixels.

Chapter 3.

SI-STM Research on Cuprate Superconductors under the Magnetic Field

SI-STM has been an essential instrument for studying cuprate superconductors, which are layered materials. Especially, SI-STM has made the study of local properties of cuprates successful in real space such as the spatial inhomogeneity of gap, impurity, dopant and superconducting vortex. In this chapter, I introduce the magnetic field study of $Bi_2Sr_2CaCu_2O_{8+\delta}$ by SI-STM.

3.1. Two types of superconductors

The interior of a superconductor is not penetrated by the magnetic flux, as Walther Meissner and Robert Ochsenfeld discovered[42]. However, if the applied magnetic field is larger than a particular value, superconductivity is broken. Superconductivity can be classified into two types, depending on how they break by magnetic fields. In type-I superconductors, the magnetization is proportional to the field until it reaches the critical value, H_c, where superconductivity is destroyed (Fig 3.1). Most type-I superconductors are pure metal (e.g., mercury, lead and aluminum).

On the other hand, type-II superconductors have an intermediate phase between H_{c1} and H_{c2}. In this phase, type-II superconductors have vortices that allow passing the magnetic flux. In the vortex, supercurrent, which is a flow of electron pairs circulating the vortex, makes potential barrier resulting in localized non-superconducting electrons in the vortex, and allow to pass the quantized superconducting magnetic flux, Φ_0. The area except for vortices is the superconducting state. When the applied magnetic field strong enough that vortices occupy the whole material, superconductivity is broken. The magnetic field where such a phase transition occurs is H_{c2}. In type-II superconductors, the magnetization is proportional to the magnetic field until the lower critical field, H_{c1}. Then, it decreases to zero until reaching a higher critical magnetic field, H_{c2}.

All known high-T_c superconductors are type-II superconductors. The application of high-T_c superconductors is extensive from not only its higher critical temperature but its higher critical magnetic field. However, due to the adversity of obtaining a good sample surface, the vortex study by scanning

probes has not worked well.

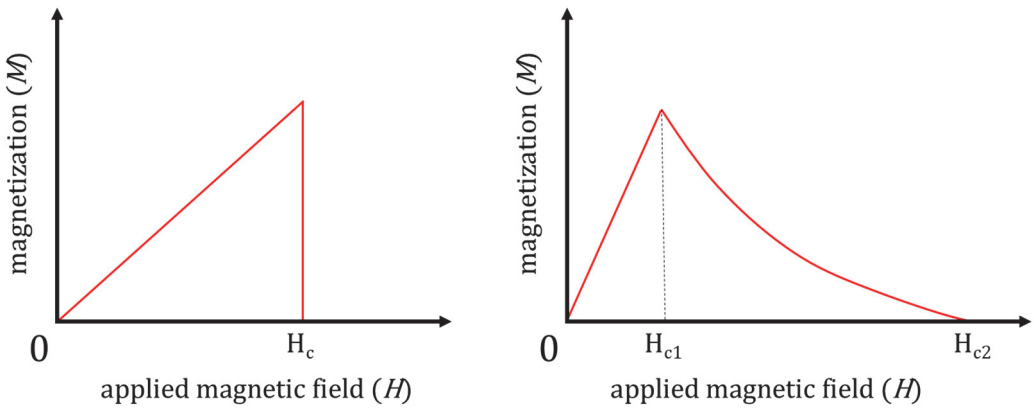

Figure 3.1: The field-dependence of the magnetization of two types of superconductors.

A magnetization of (a) type-I superconductors and (b) type-II superconductors. In type-II superconductors, there is an intermediate field range where the magnetization decreases as the magnetic field increases.

3.2. Superconducting vortex

Type-II superconductors have vortices where the quantized magnetic flux passed under a magnetic field. Alexei Alexeyevich Abrikosov predicted superconducting vortex theoretically in 1957[43]. The quantized superconducting magnetic flux has a value of $\Phi_0 = \frac{h}{2e}$.

There are two length scales in the superconducting vortex (Fig. 3.2). One is the superconducting coherence length ξ that the distance of the superconductivity breaks in the vortex. Another is the magnetic penetration depth λ that the distance of the circulating supercurrents of the vortices extends around the core. The coherence length and penetrations depth of type-II superconductors are, by definition, meet the following condition: $\lambda > \frac{\xi}{\sqrt{2}}$ [44].

Due to the flux passing through the vortex, there is a repulsive force between vortices forming Abrikosov lattice. Usually, vortices form a triangular lattice, but other shapes are possible. Vortex also has the property of being pinned for unknown reasons (one of the possible candidates is the impurity). The pinned vortex moves out of the pinned site when the energy is applied more than the pinning energy (e.g., thermal energy).

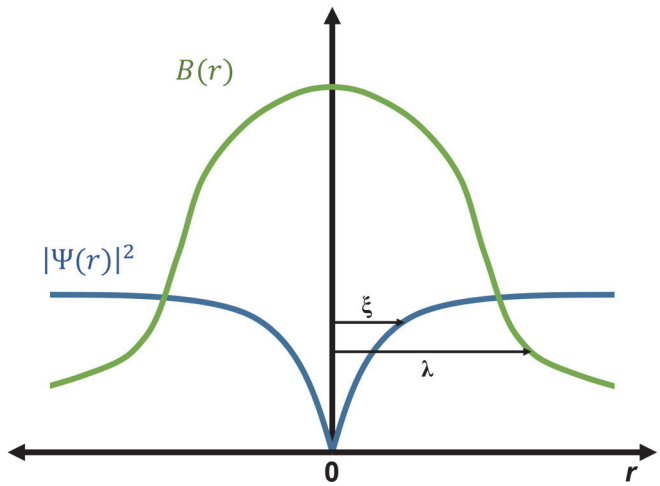

Figure 3.2: Two length scales in the vortex.

The magnetic penetration depth λ is larger than the superconducting coherence length ξ.

3.3. Advantages of SI-STM to the vortex research

The superconducting vortex consists of a core, where the pair wave function (or superfluid density n_s) vanishes. Since cuprates are strong type-II superconductors, in-plane λ is an order of hundreds of nm[45–48] while ξ is an order of nm[49]. Most of the experimental probes that image vortex in real space measures the magnetic profile. (e.g., scanning superconducting quantum interference device microscopy, magnetic force microscopy (MFM)) As the magnetic field gets strong, the variation of the magnetic profile in type-II superconductors becomes much smaller than the variation of DOS. The resolution of SI-STM, which measures the local DOS, is much better than other probes, which measure the magnetic profile. Therefore, SI-STM is the only

apparatus capable of imaging vortex in all magnetic fields range in real space.

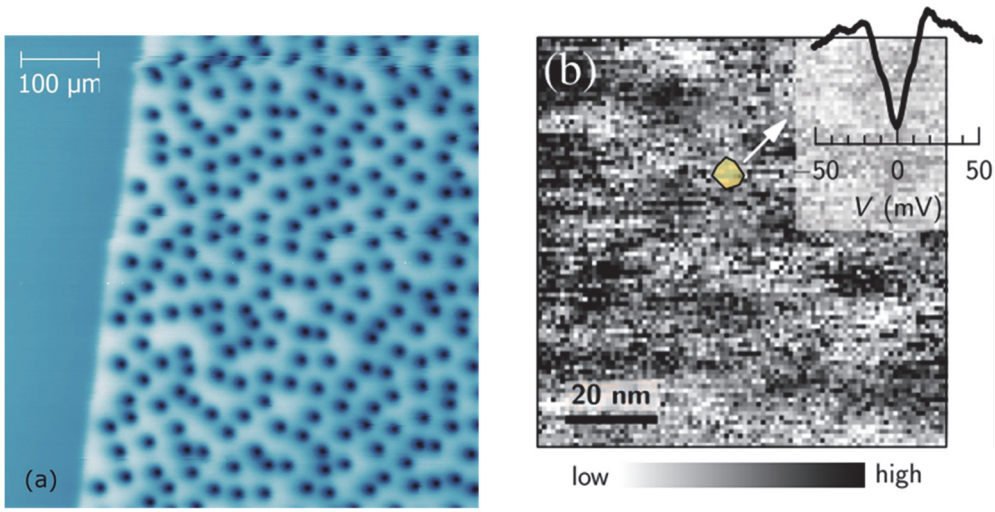

Figure 3.3: Images of the vortex of YBCO in real space by different probes.
(a) Scanning SQUID microscopy and (b) SI-STM. Black dots in (a) and black regions in (b) are vortices. The size of the vortex is much larger in (a) than (b). Therefore, the resolution for imaging the vortex is much better in SI-STM than scanning SQUID microscopy. Reproduce from (a)[50] and (b)[51].

3.4. Reported vortex studies of BSCCO using SI-STM

Due to the advantages above, SI-STM has been the most effective probes in imaging the core of the superconducting vortex. Hess *et al.* have succeeded in imaging the vortex using SI-STM for the first time in conventional superconductor $NbSe_2$[52]. Hess not only observed the vortex lattice directly but

also the quantized bound states in the vortex predicted by Caroli-de Gennes-Matricon[53]. The Caroli-de Gennes-Matricon bound state predicted that the zero-bias conductance peak appears at the center of the vortex core, and this peak is divided into two peaks as gone away from the core.

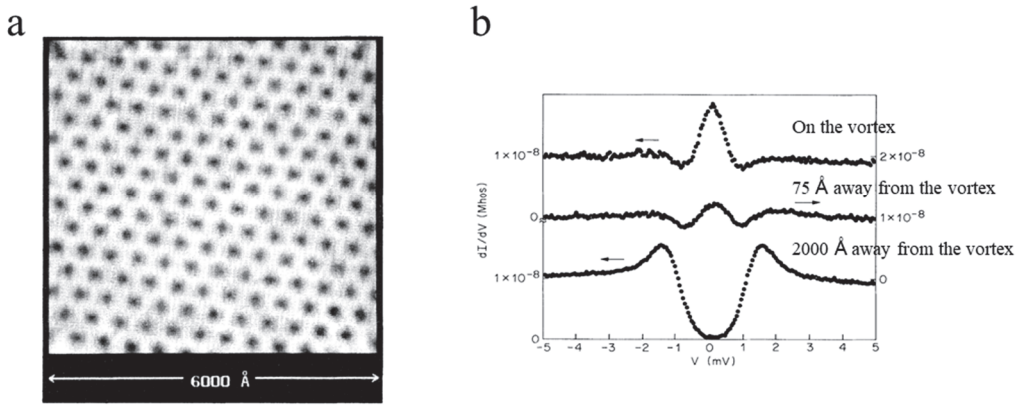

Figure 3.4: The SI-STM image of the vortex in a conventional superconductor $NbSe_2$.

(a) It shows perfect triangular lattice. (b) The zero-bias peak is shown at the vortex center. As away from the vortex core, the zero-bias peak is divided. Reproduced from [52].

The first observation of the superconducting vortex of BSCCO is on the OD BSCCO in the negative energy region[12]. While vortices of YBCO form the lattice structure, those of BSCCO do not. The reason is that BSCCO shows a nearly two-dimensional electronic structure with weak interactions between the adjacent layers, and the inhomogeneity of BSCCO easily pins the vortex.

In 2000, Shuheng Pan *et al.* measured the vortex of BSCCO over a large field of view (FOV) by SI-STM[13]. They reported that vortices pinned by impurities, and calculated the coherence length of the vortex core by analyzing impurity-free vortices. Two years later, Jennifer E. Hoffman *et al.* observed that the vortex core had four-unit cells checkboard structures[14]. In the following decade, several additional papers have appeared on the vortex core structure of BSCCO. Tadashi Machida *et al.* reported that the vortex core structure is the enhanced Bogoliubov QPI using the Z image[54] in 2016. Recently, Stephen Edkins *et al.* revealed that four-unit cells checkboard patterns, as well as eight-unit cells pair density wave (PDW), exist in the vortex halo in 2019[55].

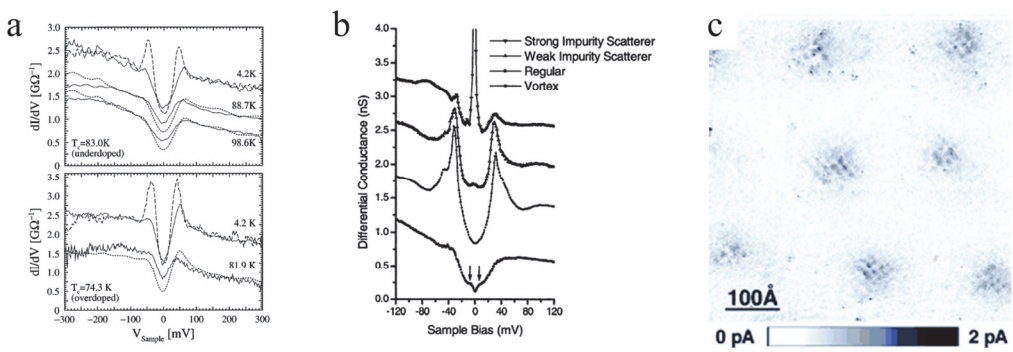

Figure 3.5: Reported vortex studies of BSCCO.

(a) The first spectroscopy in the vortex core. (b) Research for imaging vortices in the large FOV. (c) The first reported checkerboard patterns in the vortex core. Reproduced from (a)[12], (b)[13], and (c)[14]

Chapter 4.

Density of states Modulation of $Bi_2Sr_2CaCu_2O_{8+\delta}$ in the Magnetic Fields

In this chapter, I introduce the density of states modulation (DOSM) of $Bi_2Sr_2CaCu_2O_{8+\delta}$ in the magnetic field experiments. Two different doping samples - a slightly underdoped (SUD) and highly underdoped (HUD) $Bi_2Sr_2CaCu_2O_{8+\delta}$ - were used. I show the features of DOSM in each magnetic field experiment and discuss commonalities and differences between the two experiments.

4.1. SI-STM images of the slightly underdoped $Bi_2Sr_2CaCu_2O_{8+\delta}$

It has been reported several times that the nearly optimal doped $Bi_2Sr_2CaCu_2O_{8+\delta}$ shows distinct vortex signs and core structures in SI-STM data[12–14,54–57]. For this reason, I chose a slightly underdoped (SUD) $Bi_2Sr_2CaCu_2O_{8+\delta}$ with T_c = 91 K to study the superconducting vortex. I performed an STM experiment at 4.2 K with applying magnetic fields of 0 T, 2 T, 4 T, and 5 T to the sample. The magnetic fields are applied perpendicular to CuO_2 planes of the samples. The sample was cleaved *in-situ* at low-temperature ultra-high vacuum and revealed an atomically clean and flat Bi-O plane. I obtained the differential conductance image $g(\mathbf{r}, E, B)$ using a standard lock-in method with modulation bias of two meV. Whenever applied magnetic field changes, the sample was heated up to 30 K to make vortices located uniformly.

Figure 4.1a-d show topographic images of the cleaved Bi-O plane of an SUD $Bi_2Sr_2CaCu_2O_{8+\delta}$ with changing magnetic fields from 0 to 5 T, respectively. All images are 38 nm *x* 38 nm in size and 200 *x* 200 pixels. Figure 4.1e-h are gap-images of the same FOV in Fig. 4.1a–d, respectively, showing similar gap distributions (Fig. 4.2) for all four FOV's shown. Figure 4.3 show differential conductance images $g(\mathbf{r}, E, B)$ at different energy with and without magnetic fields. Superconducting vortices are discernible by the well-known four unit cell checkerboard-like core structures[14] on the images in low energies ($|E| < 12$ meV) in the magnetic fields. As the magnetic field is increased, the number of vortices also increases. Wu *et al.*[58] suggested that the vortex core structure of four-unit cell periodicity[14] comes from a static charge order while Machida *et al.*[54] reported that the vortex core structures are the enhanced Bogoliubov QPI. I observed that the vortex core structure is not static but varies as the sample bias

changes, and the period of this pattern is about four-unit cells at $E = 8$ meV (Fig. 4.3).

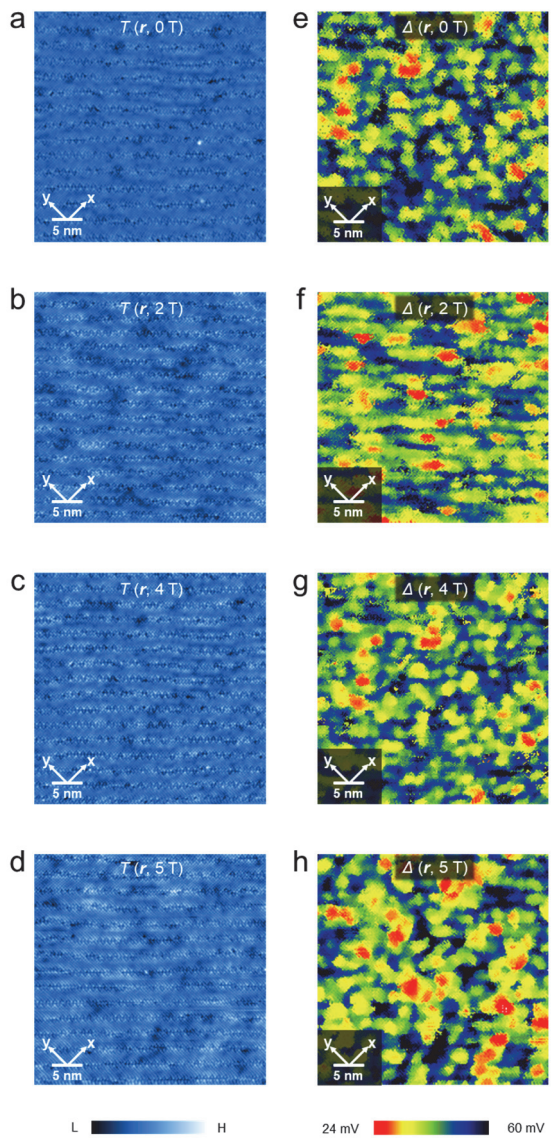

Figure 4.1: Topographic and gap images of the SUD $Bi_2Sr_2CaCu_2O_{8+\delta}$ in various magnetic fields.

(a)-(d) Topographic images $T(\mathbf{r}, B)$ of the SUD $Bi_2Sr_2CaCu_2O_{8+\delta}$ in magnetic fields 0 T, 2 T, 4 T, and 5 T, respectively. Each image shows the different FOV and the size of 38 nm *x* 38 nm. Supermodulation in the cleaved Bi-O surface is visible. *x* and *y* are Cu-O-Cu bonding directions. (e)-(h) Gap images $\Delta(\mathbf{r}, B)$ in the same FOVs as (a)-(d), respectively. Gaps are inhomogeneously distributed. There is no clear field dependence on the gap images. The average gaps are from 43 meV to 47 meV (Figure 4.2).

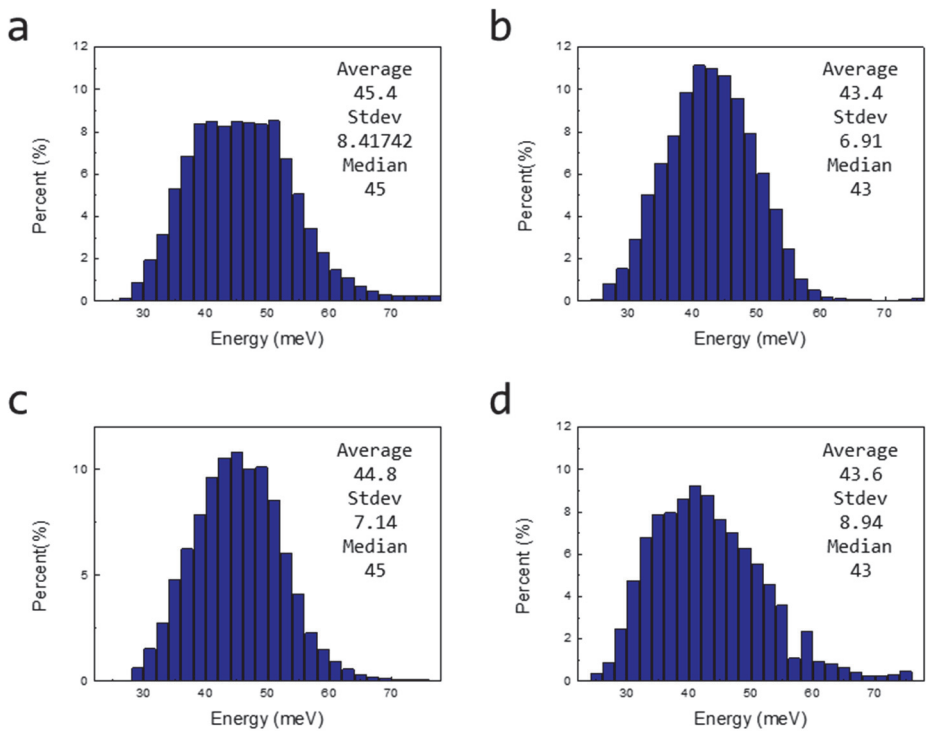

Figure 4.2: The histograms of gap images in the magnetic fields.

(a) 0 T, (b) 2 T, (c) 4 T, (d) 5 T. Means, standard deviations and medians are presented in each figure. Due to the different FOV, the average gaps vary from 43.4 to 45.4 by the images.

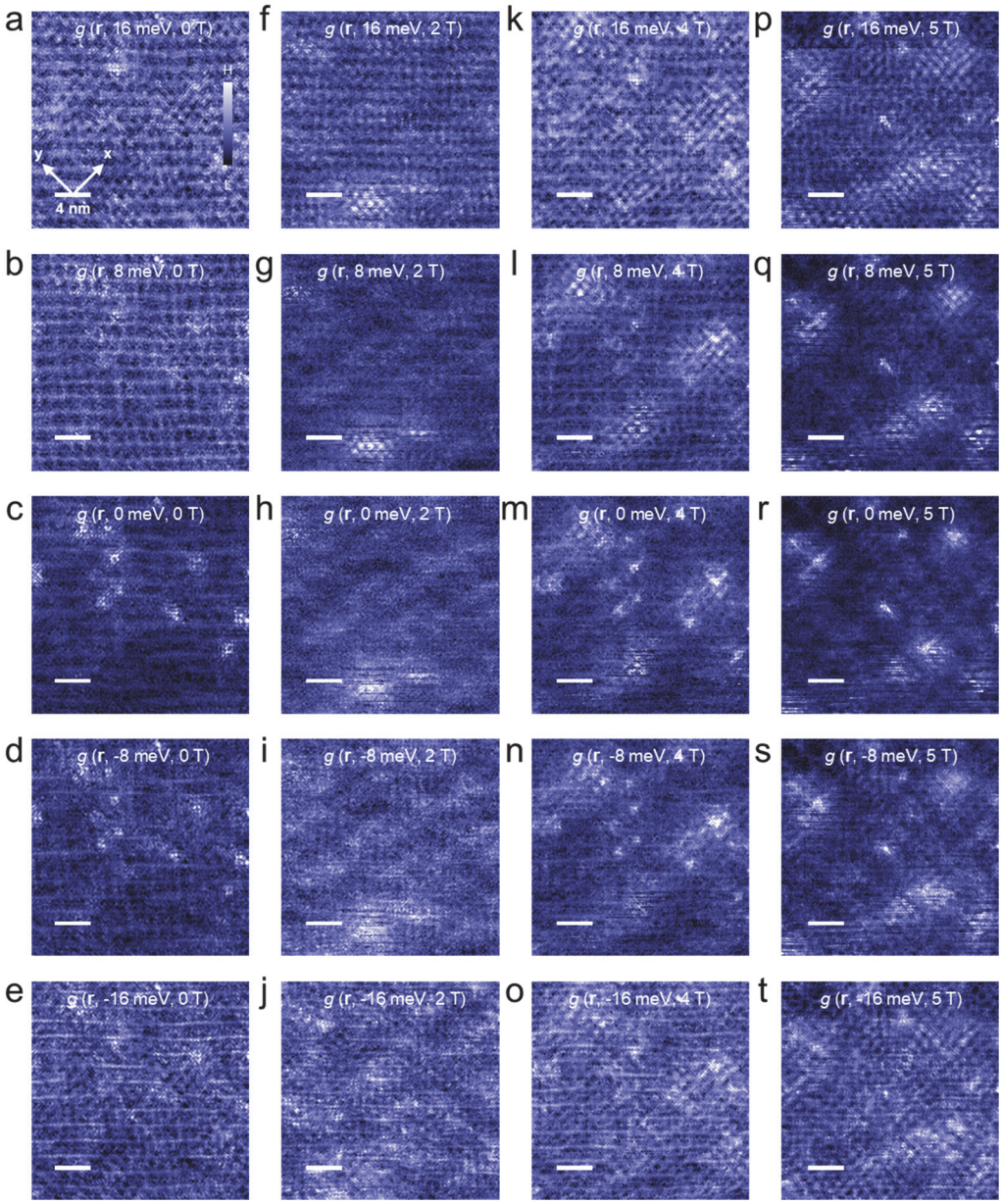

Figure 4.3: Differential conductance images *g(*r, *E*, *B*) at different energies with and without magnetic fields.

(a)–(e) *g(***r**, *E*, *B* = 0 T), (f)–(j) *g(***r**, *E*, *B* = 2 T), (k)–(o) *g(***r**, *E*, *B*= 4 T), (p)–(t) *g(***r**, *E*, *B* = 5 T). Except for zero field images, superconducting vortices and its core structures are presented in all images under magnetic fields. One can also see that the patterns

inside the vortex change as the energy varies, and the shape of the checkerboard in the vortex core region is more evident in the positive energy. As the magnetic field increases, the number of vortices also increases. The radius of each vortex varies from 8 nm to 10 nm, but, has no dependence on the energy. If $|\boldsymbol{E}| >$ 16 meV, vortices become indistinguishable from the $g(\mathbf{r}, E, B)$ images, except near coherent peak energy.

4.2. Superconducting flux quantum in a single vortex

Figure 4.4 shows a differential conductance image $g(\mathbf{r}, E = 6$ meV, $B = 5$ T) with a FOV of 150 nm x 150 nm. The total number of vortices in the FOV is 52 ± 3. According to the total flux that is the multiplication of the magnetic field and the area, I can calculate the flux through a single vortex.

$$\frac{BA}{the\ \ number\ \ of\ \ vortices} = \frac{5 \times 150^2}{52 \pm 3} Wb = 2.05 \sim 2.30 \times 15^{-15}$$

Since the value of a superconducting magnetic flux quantum is $\Phi_0 = \frac{hc}{2e} = 2.1\ x\ 10^{-15}$Wb, I can see that each vortex has a superconducting magnetic flux quantum. There are intervals between the vortices due to the repulsive force between the fluxes passing through the vortices. However, the $Bi_2Sr_2CaCu_2O_{8+\delta}$ does not establish the Abrikosov lattice as in conventional superconductors[52].

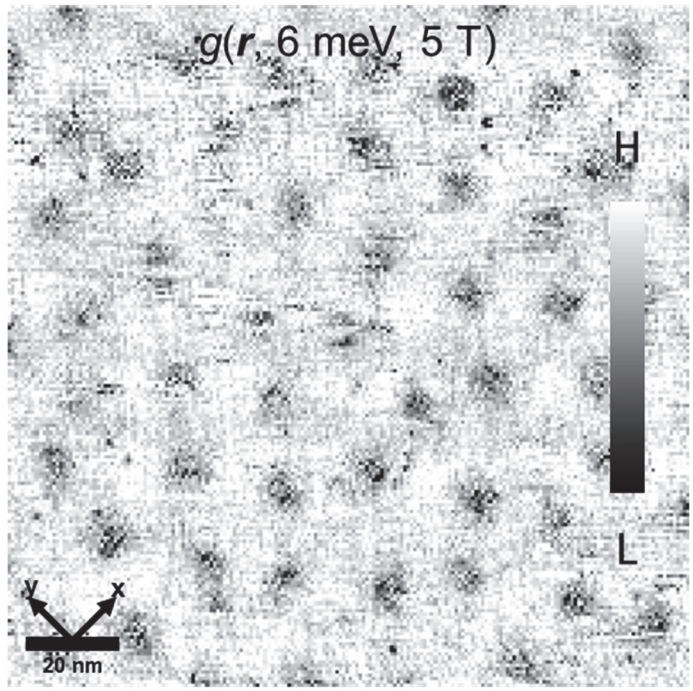

Figure 4.4: The *g*(r, *E* = 6 meV , *B* = 5 T) of the SUD $Bi_2Sr_2CaCu_2O_{8+\delta}$.
The size of the FOV is 150 nm *x* 150 nm. The number of vortices, which have enhanced *dI/dV*, is about 52. Abrikosov lattice is not formed.

4.3. Electronic structures in the vortex

To study the electronic structures in the vortex, masking the images to divide the vortex region (VR) and non-vortex region (NVR) using the Fourier filter. After masking, I performed two-dimensional Fourier transformation (2DFT) to the masked images to find the property of DOSM in the vortex.

4.3.1. Masking method

I used a Fourier filter method to divide VR and NVR. Low-pass filtered differential conductance image $g(\mathbf{r}, E = 10\ \text{meV}, B = 5\ \text{T})$ is used to filter (Fig. 4.5) where the cut-off **q** value is chosen to be $0.05\frac{2\pi}{a_0}$. (a_0 is a lattice constant of 3.8 Å). I created a circle around the center of the FT image with the determined **q** value and made the value 0 except for the inner value of the circle. This is a kind of low-pass filter that smoothes the original *dI/dV* data. In this low pass filtered image, the VR has a higher intensity, but the NVR has a lower one. Next, using the histogram of the low-pass filtered $g(\mathbf{r}, 10\ \text{meV}, 5\ \text{T})$, I assigned the regions with the amplitude above 84 % as VR and the regions with the amplitude below 60 % as NVR, respectively. In this scheme, VR accounts for 13.5% of the total FOV and NVR 50%. The masked areas of VR and NVR are shown in Fig. 4.5.

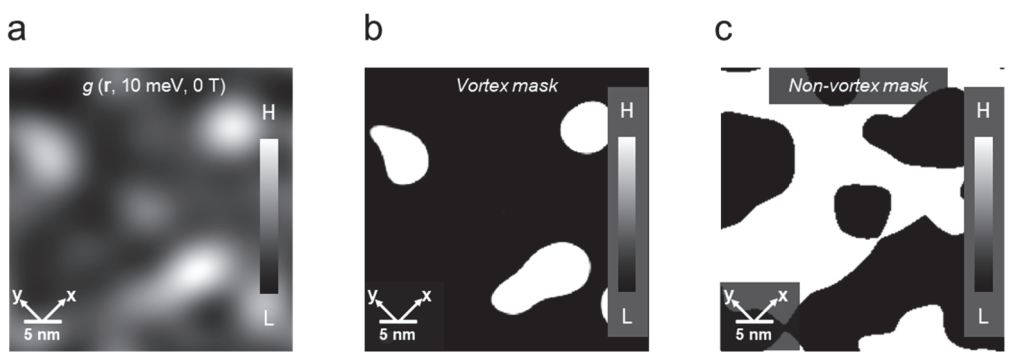

Figure 4.5: The low-pass filter created by the Fourier method to divide VR and NVR.

A filtered image of (a) $g(\mathbf{r}, 10\ \text{meV}, 5\ \text{T})$, (b) masked image of VR and (c) NVR.

4.3.2. FT images of VR and NVR

I performed a 2DFT to each masked conductance image, and the results are shown in Fig. 4.6a-d. In VR, $\mathbf{q_1}$* peaks have the strongest intensity at the low energy (red circle in Fig. 4.6c) while in NVR, $\mathbf{q_1}$* peaks are much weaker (Fig. 4.6d). 2D image plots of the line-cut along the $\mathbf{q_x}$ direction (Fig. 4.7a-b) show that the vortex core pattern associated with $\mathbf{q_1}$* is neither a non-dispersing static order nor an enhanced QPI. The $\mathbf{q_1}$* from VR disperses from -12 meV to 12 meV, where the vortex checkerboard is observable. Remarkably, instead of showing a *particle-hole* symmetric dispersion as in the QPI following an octet model in the superconducting phase[8], the dispersion showed a *particle-hole* asymmetric behavior. Notably, the $\mathbf{q_1}$* follows the electron-like dispersion, which $\mathbf{q_1}$* increases with energy, near the Fermi energy. On the other hand, the $\mathbf{q_1}$* in NVR shows a dispersion similar to the $\mathbf{q_1}$*'s in the 0 T field: a *particle-hole* symmetric QPI (Fig. 4.8).

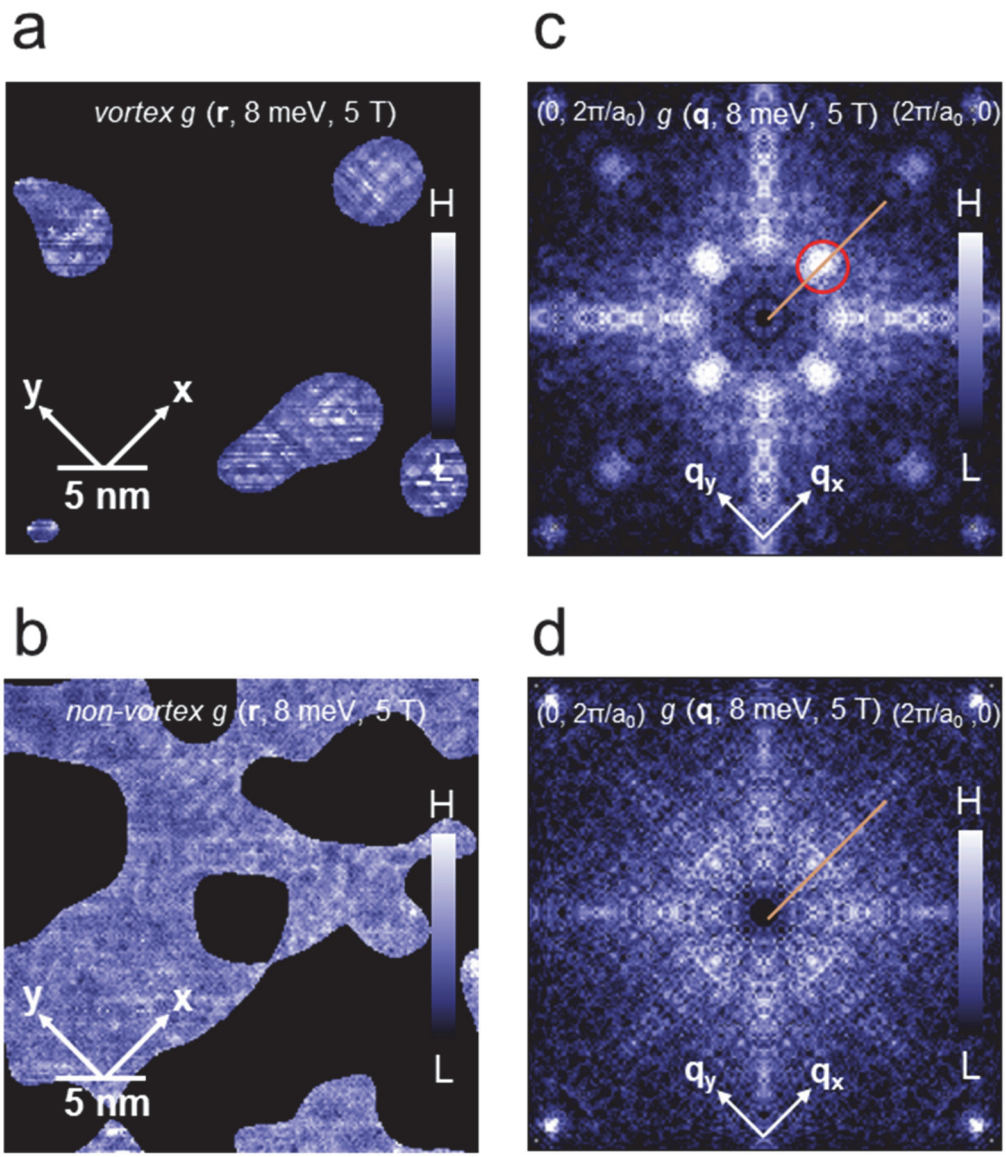

Figure 4.6: Masked differential conductance images and their 2DFT images.

An intermediate area located between VR and NVR is removed from both images. Masked images of (a) the vortex and (b) non-vortex at E = 8 meV. (c)-(d) 2DFT images of (a)-(b). $\mathbf{q}_1$* peak (red circle) corresponding to the core structures in vortices is marked in (c). There is no clear peak in the 2DFT image of NVR. Bragg peaks are presented in (c) and (d).

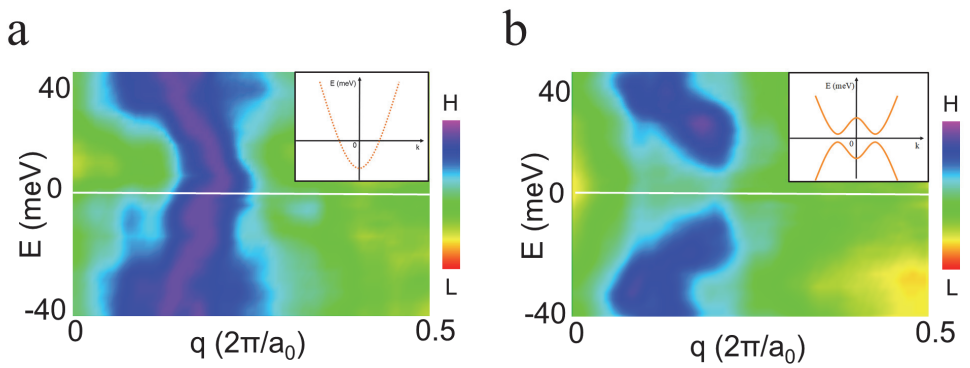

Figure 4.7: Dispersions in VR and NVR of the SUD $Bi_2Sr_2CaCu_2O_{8+\delta}$.

(a)-(b) Two-dimensional images of the energy-dependence of the line-cut data along the $\mathbf{q}_x$ direction. In VR, $\mathbf{q}_1$* shows a *particle-hole* asymmetric and electron-like dispersion near the Fermi energy. In NVR, $\mathbf{q}_1$* shows a *particle-hole* symmetric dispersion, following the octet model Bogoliubov QPI [8] . Each value of the line-cut is divided by the maximum value in (a) and the average value in (b) to show the dispersion clearly (raw images in Fig. 4.11). Schematic plots of a *particle-hole* asymmetric and symmetric dispersion curves in **k** space are presented ((a)–(b), inset).

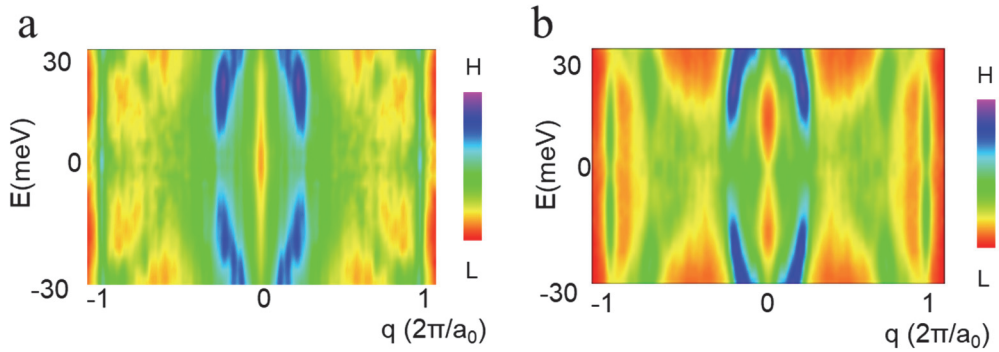

Figure 4.8: Two-dimensional plots of q_1 of the SUD $Bi_2Sr_2CaCu_2O_{8+\delta}$

Images (a) of the non-magnetic field and (b) in NVR in 5 T. $\mathbf{q}_{1*}$ in both images show the same energy dependence: *particle-hole* symmetric dispersions.

4.4. SI-STM images of the HUD $Bi_2Sr_2CaCu_2O_{8+\delta}$

Figure 4.9 shows spectroscopic imaging results on the HUD $Bi_2Sr_2CaCu_2O_{8+\delta}$ at 0 T and 13 T at the same FOV at 4.2 K. Since each vortex has a superconducting magnetic flux quantum (Fig. 4.4), one can expect about four or five vortices within FOV. Unlike the SUD experiment, however, no vortex was found within my instrumental limit. Furthermore, on the HUD $Bi_2Sr_2CaCu_2O_{8+\delta}$, the checkerboard-like pattern spanned to an extended area and showed a similar *particle-hole* asymmetric dispersion in both measurements with and without magnetic fields (Fig. 4.9 a-b).

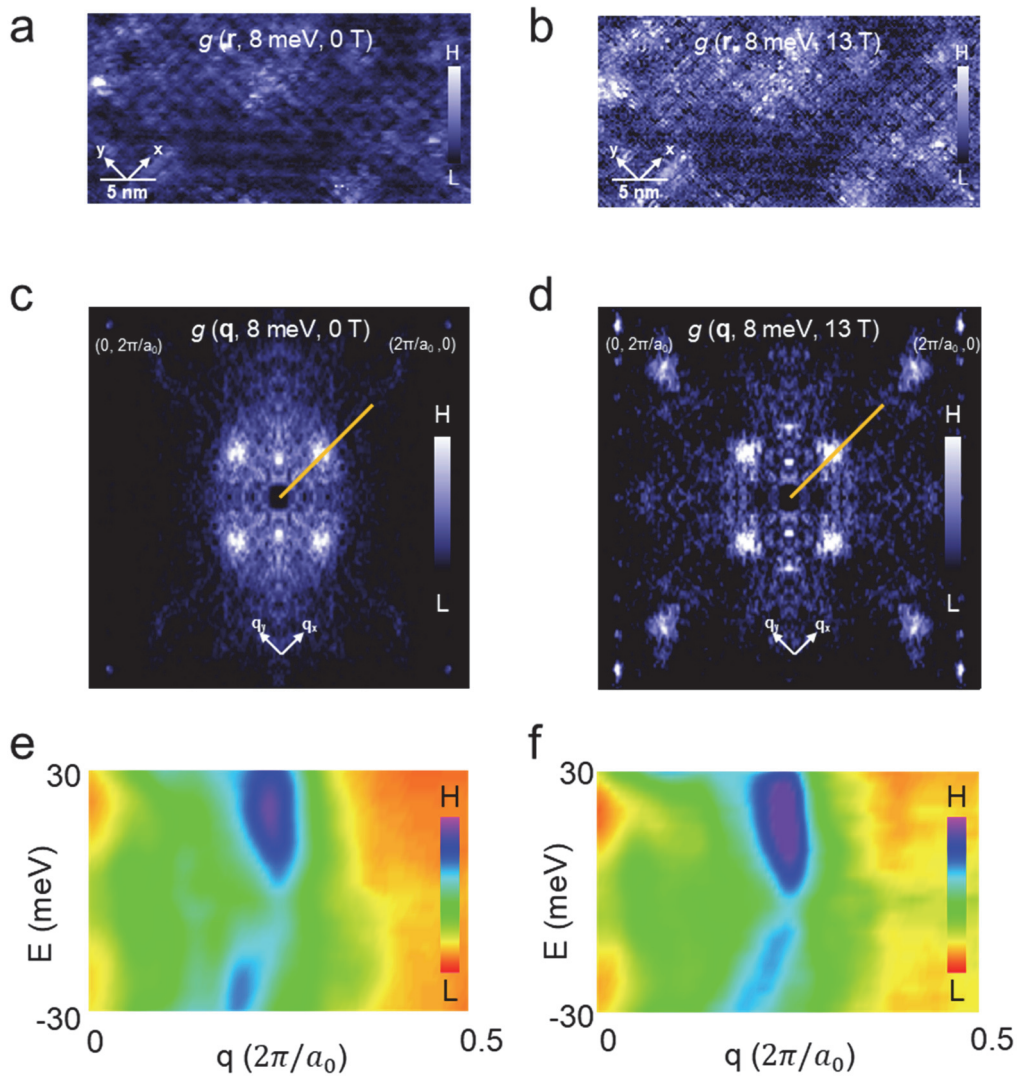

Figure 4.9: SI-STM images of the HUD $Bi_2Sr_2CaCu_2O_{8+\delta}$

(a)-(b) Differential conductance images *g*(**r**, *E*, *B*) of the HUD (T_c = 40 K) $Bi_2Sr_2CaCu_2O_{8+\delta}$ on the same FOV at E = 8 meV in magnetic fields of 0 T and 13 T. The FOV is 20 nm *x* 40 nm. Unlike SUD images, there is no sign of the vortex on the 13 T image. However, patterns similar to the ones observed inside vortices exist over a wide area of the FOV. (c)-(d) 2DFT images of (a)-(b) under 0 T and 13 T. Both images show $\mathbf{q_1}$* peaks clearly. There is a noticeable difference between the **q** images at 0 T

and 13 T of the intensity of the $\mathbf{q_1}$* and $\mathbf{q_5}$*. Bragg peaks are presented in (c) and (d). (e)-(f) Energy-dependence line-cut data (orange lines in (c) and (d)) along the $\mathbf{q_x}$ direction. The energy dependence of the $\mathbf{q_1}$* peaks displays electron-like dispersions in both images of 0 T and 13 T.

4.5. Change of DOSM of the HUD $Bi_2Sr_2CaCu_2O_{8+\delta}$ in the magnetic fields

Figure 4.10 is the energy-dependent difference images created by subtracting the $g(\mathbf{r}, E, 0\ \mathrm{T})$ from $g(\mathbf{r}, E, 13\ \mathrm{T})$ at the same FOV. 2DFT of the difference images are also shown. The difference was calculated after each $g(\mathbf{r}, E, B)$ was divided by the average value for each energy to minimize the error due to the tip condition. $\mathbf{q_1}$* and $\mathbf{q_5}$* modulations and its 2DFT peaks are shown in **r** and **q** space difference images. Both modulations become stronger when the magnetic field is applied. Among the Bogoliubov QPI peaks, the peaks corresponding to $\mathbf{q_1}$, $\mathbf{q_4}$ and $\mathbf{q_5}$ are reported to get stronger with magnetic field since they are originated from the scattering between the bands with the same phase in order parameter[54], while Parker *et al.* reported that $\mathbf{q_1}$* and $\mathbf{q_5}$* in an underdoped $Bi_2Sr_2CaCu_2O_{8+\delta}$ are different from the octet-model Bogoliubov QPI[59]. The **k** space origin of the $\mathbf{q_1}$* and $\mathbf{q_5}$* modulations requires further study.

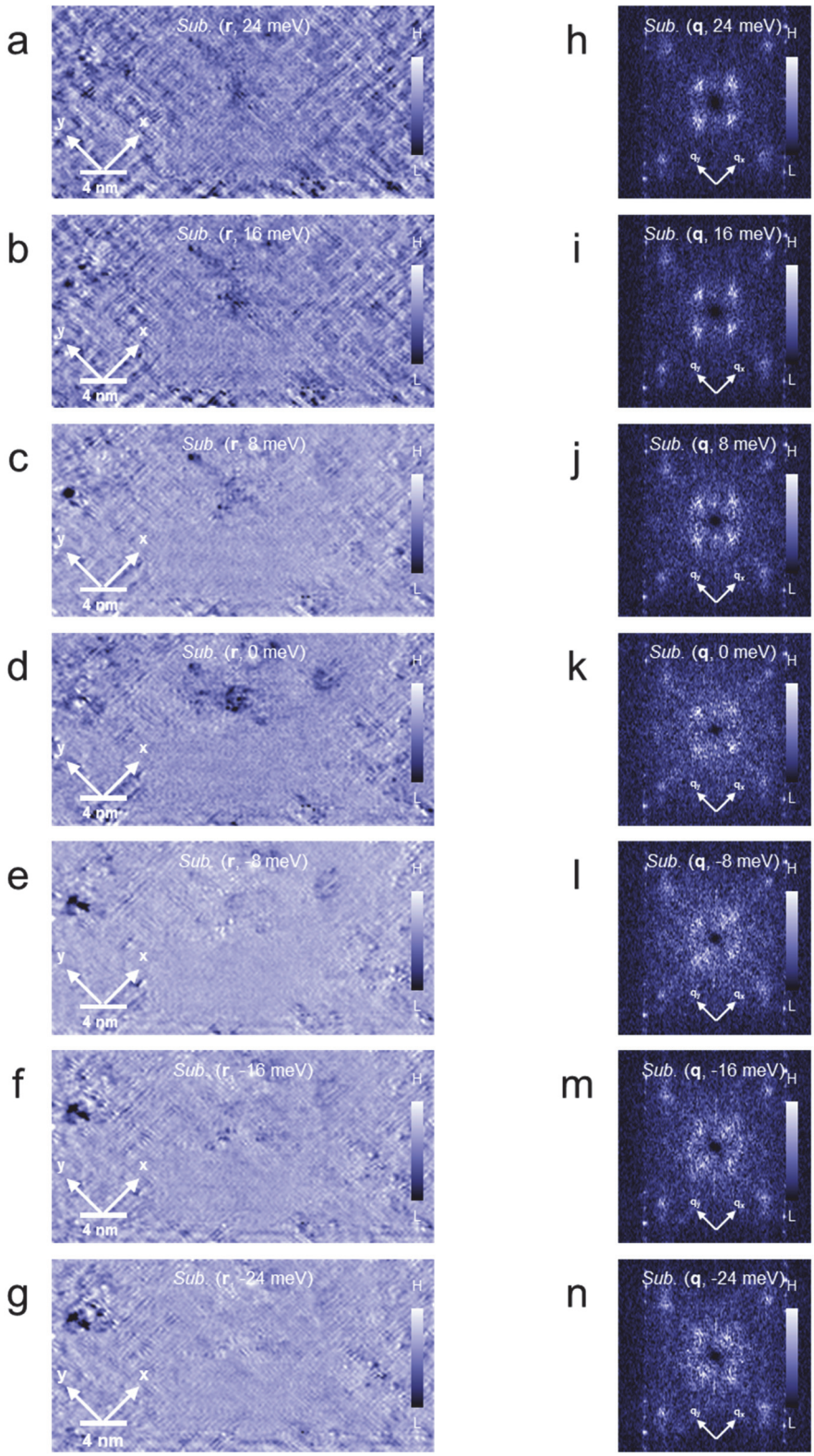
a
Sub. (r, 24 meV)
H
L
y
x
4 nm
h
Sub. (q, 24 meV)
H
L
q_y
q_x
b
Sub. (r, 16 meV)
i
Sub. (q, 16 meV)
c
Sub. (r, 8 meV)
j
Sub. (q, 8 meV)
d
Sub. (r, 0 meV)
k
Sub. (q, 0 meV)
e
Sub. (r, -8 meV)
l
Sub. (q, -8 meV)
f
Sub. (r, -16 meV)
m
Sub. (q, -16 meV)
g
Sub. (r, -24 meV)
n
Sub. (q, -24 meV)

Figure 4.10: Difference images *g(*r, *E*, *B* = 13 T) - *g(*r, *E*, *B* = 0 T) of the HUD $Bi_2Sr_2CaCu_2O_{8+\delta}$.

$\mathbf{q_1}$* and $\mathbf{q_5}$* modulations are discernible clearly in all images. As energy increases, the amplitude of both peaks also increases.

4.6. Relation between DOSM in the vortex and of the HUD $Bi_2Sr_2CaCu_2O_{8+\delta}$

To check if the dispersion in VR and HUD are related, I plotted the $\mathbf{q_1}$* in different doping levels and magnetic field conditions in Fig. 4.11 and 4.12. Figure 4.11 displays the line-cut along the $\mathbf{q_x}$ direction in *g(***q**, *E*, *B*) after a symmetrization in the *x* and *y* axis. To make plots, I used a Lorentzian fitting. One-dimensional Lorentzian fitting was performed to the line-cut in $\mathbf{q_x}$ direction for each energy. Each line-cut was box-car (9 pixels by 9 pixels) averaged before the fitting. Due to the four-fold symmetry, I used the **q** images symmetrized to the *x* and *y* axis. Moreover, each line-cut data was normalized by the data to the average value at each energy to make the **q** peaks more visible. The dispersion slopes of the peaks near $\mathbf{q_1}$ in VR ($\mathbf{q_1}$*) and NVR ($\mathbf{q_1}$) are different. Also, the relative intensity of the $\mathbf{q_1}$* is stronger in positive energies (hole state) for both in VR and HUD $Bi_2Sr_2CaCu_2O_{8+\delta}$.

In Fig 4.12, all three $\mathbf{q_1}$* except in NVR showed an electron-like dispersion. My result shows the similar *particle-hole* asymmetrically dispersing DOSM in VR on the SUD $Bi_2Sr_2CaCu_2O_{8+\delta}$ as well as in an extended area on the HUD $Bi_2Sr_2CaCu_2O_{8+\delta}$'s case at 13 T as well as 0 T without a trace of vortices, which

have a striking resemblance to the dispersing patterns reported on the underdoped $Bi_2Sr_2CaCu_2O_{8+\delta}$ above T_c[59]. Only NVR shows a *particle-hole* symmetric QPI dispersion following an octet model[8] at $\mathbf{q_1}$ location. From this observation, I concluded that, as the magnetic field is increased and the doping level is lowered, the *particle-hole* asymmetric DOSM became stronger and expanded in an area rather than localized at the vortex core.

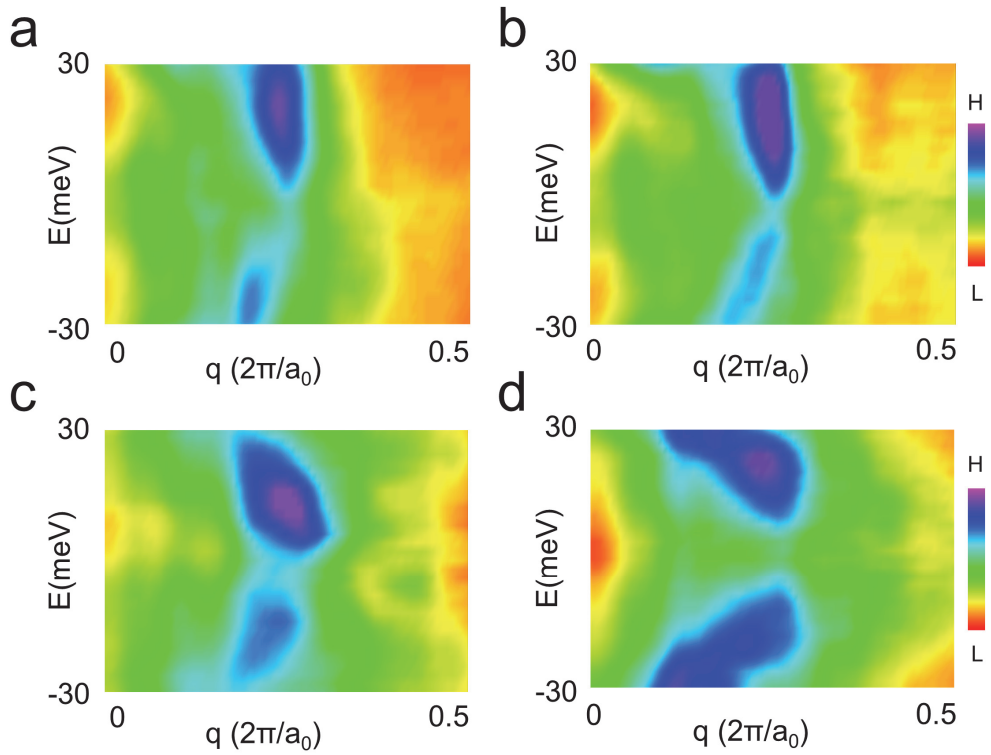

Figure 4.11: Two-dimensional plots of q_1* of the SUD and HUD $Bi_2Sr_2CaCu_2O_{8+\delta}$. Two-dimensional plots of (a) the HUD $Bi_2Sr_2CaCu_2O_{8+\delta}$ in 0 T, (b) the HUD $Bi_2Sr_2CaCu_2O_{8+\delta}$ in 13 T, and (c) in VR of the SUD $Bi_2Sr_2CaCu_2O_{8+\delta}$ (d) in NVR of the SUD $Bi_2Sr_2CaCu_2O_{8+\delta}$

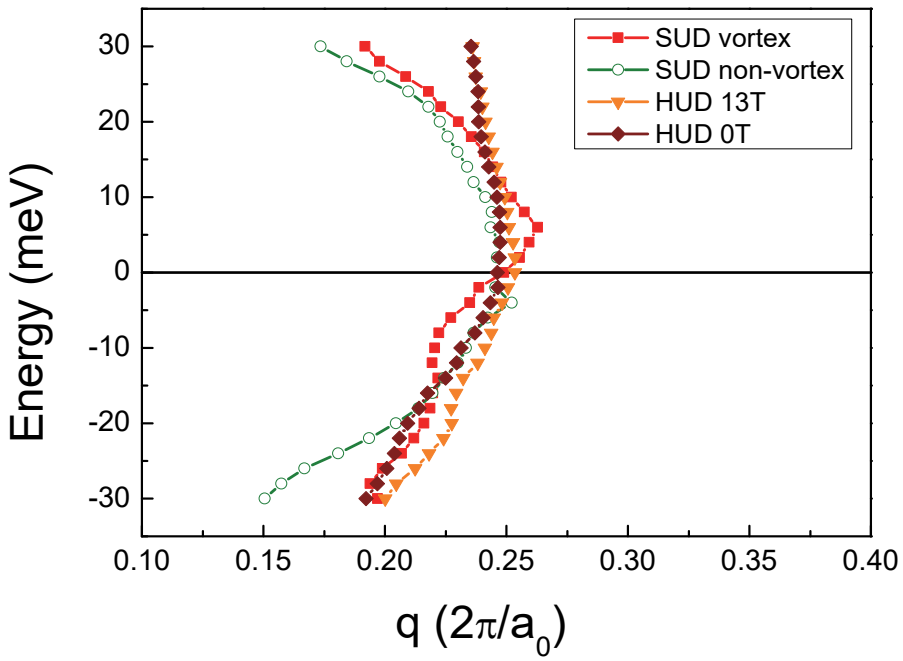

Figure 4.12: The E vs. q plots of the q_1* peaks from the SUD and HUD $Bi_2Sr_2CaCu_2O_{8+\delta}$.

Except for the $\mathbf{q_1}$* in NVR on the SUD $Bi_2Sr_2CaCu_2O_{8+\delta}$, other **q** peaks show *particle-hole* asymmetric dispersions. $\mathbf{q_1}$* in HUD sample and $\mathbf{q_1}$* in VR of SUD sample show *particle-hole* asymmetric and electron–like dispersions at the energies near E_F: $E < 10$ meV, while $\mathbf{q_1}$* in NVR exhibits a *particle-hole* symmetric dispersion.

4.7. Comparison of DOSM with CDW

CDW and charge orders have been reported in various experimental studies in underdoped cuprate superconductors[60–62]. I integrated differential conductance images g(**r**, *E*, *B*) in the negative energy region (filled states) in

order to compare the results with other experimental results (Fig. 4.13). This is a conventional way to obtain a charge distribution near the Fermi energy. The $\mathbf{q_1}$* values obtained from the integrated *g* images were 0.21 for the 0 T of HUD, 0.225 for the 13 T of HUD, and 0.225 for VR in the SUD $Bi_2Sr_2CaCu_2O_{8+\delta}$. This is slightly different from the CDW **q** value of 0.265 of $Bi_2Sr_2CuO_{6+\delta}$ or 0.3 of YBCO but almost the same as 0.23 of $La_{2-x}Ba_xCuO_4$. This result suggests that the *particle-hole* asymmetric DOSM I present in this chapter and the bilateral CDW reported in a wide range of cuprates [61–64], can be of the same origin.

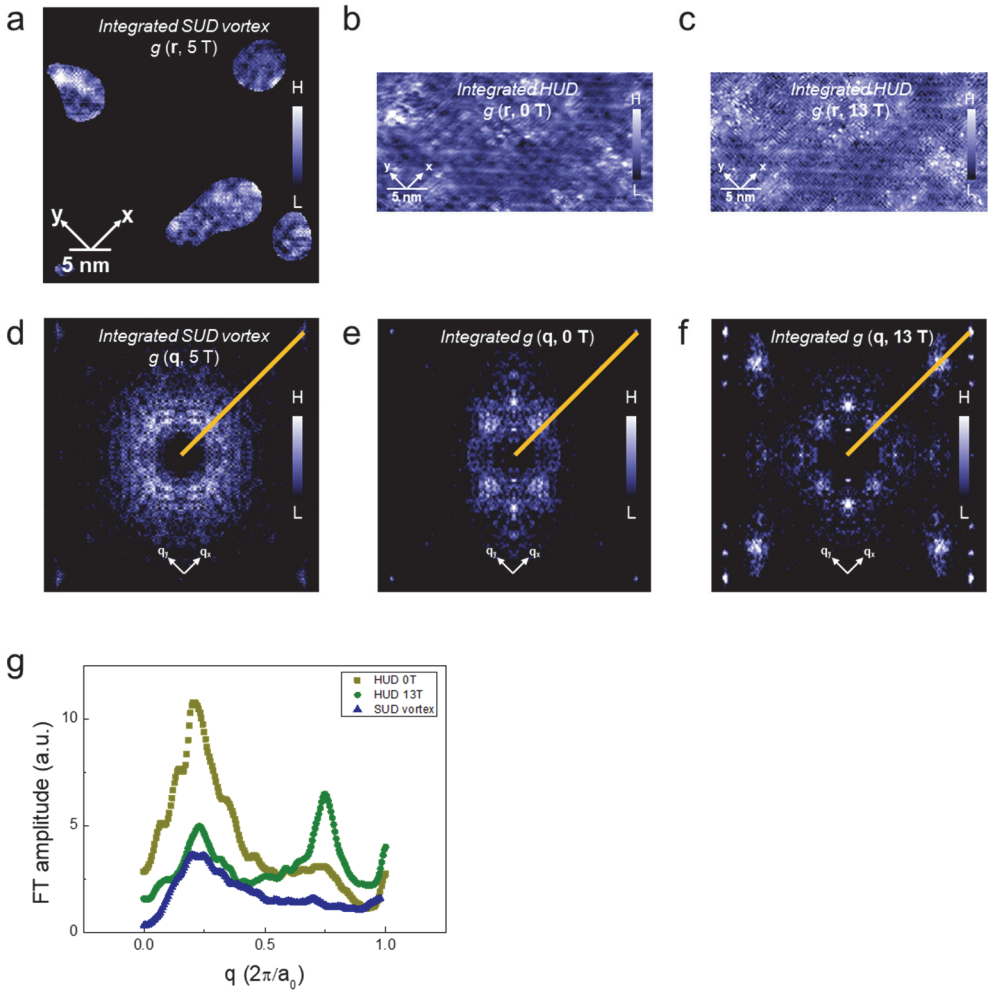

Figure 4.13: Images integrated from -30 meV to 0 meV that have *particle-hole* asymmetric q_1* peaks.

(a)-(c) Differential conductance images integrated with the negative energy of VR in the SUD $Bi_2Sr_2CaCu_2O_{8+\delta}$, 0 T and 13 T in the HUD $Bi_2Sr_2CaCu_2O_{8+\delta}$. (d)-(f) 2DFT images of (a)-(c). (g) Line-cut of (d)-(f). The directions of the line-cut are represented in (d)-(f). **q_1*** peaks are shown clearly in all data.

4.8. Summary

First, I performed magnetic field studies on $Bi_2Sr_2CaCu_2O_{8+\delta}$ with two different doping levels. When I applied the magnetic field to the SUD $Bi_2Sr_2CaCu_2O_{8+\delta}$, I could observe the vortex in the differential conductance images. I divided VR and NVR by filtering the *g* image. The electronic structure of the SUD $Bi_2Sr_2CaCu_2O_{8+\delta}$ was different inside and outside the vortex. Inside the vortex, the $\mathbf{q_1}$* modulation with a four-unit cell periodicity had a strong intensity and showed a *particle-hole* asymmetric energy-dependence. Especially, near the Fermi energy, $\mathbf{q_1}$* modulation showed the electron-like movement that increases with energy. I observed similar energy dependence of $\mathbf{q_1}$ in NVR: a *particle-hole* symmetric dispersion like BQPI from the no-field experiment.

Unlike SUD, there was no visible vortex sign when the magnetic field was applied to HUD. However, there were $\mathbf{q_1}$* and $\mathbf{q_5}$* modulations over a wide range in FOV, both with and without the magnetic fields. This $\mathbf{q_1}$* modulation had a similar property with that in SUD's vortex: a *particle-hole* asymmetric dispersion. Besides, as the magnetic field was applied, $\mathbf{q_1}$* and $\mathbf{q_5}$* modulation became stronger. From these two observations, I concluded that the modulation in the vortex of the SUD $Bi_2Sr_2CaCu_2O_{8+\delta}$ expanded to the broad area in the HUD $Bi_2Sr_2CaCu_2O_{8+\delta}$.

Chapter 5.

Real Space Model for Quantum Oscillations using Density of States Modulation on Cuprates

Two magneto-transport measurements reported in 2007 indicate the possibility of electron pockets on the Fermi surface in the low temperature and strong magnetic fields[65,66]. Various implications for the location of electron pockets have been suggested, but it is still controversial. To find the origin of quantum oscillations (QO) in cuprates, I introduce the real space model for QO in this chapter. Then, I introduce an alternative explanation of the QO results in terms of DOSM of $Bi_2Sr_2CaCu_2O_{8+\delta}$.

5.1. Quantum oscillations

QO is a series of experimental techniques that the physical properties of material oscillate in the presence of a strong magnetic field. In the case of resistance, it is called the Shubnikov-de Haas effect, and in the case of magnetic susceptibility, it is called the de Haas-van Alphen effect. The Landau quantization of Fermions that electron orbit quantized under the magnetic field is the cause of this phenomenon. Therefore, QO is a representative property of Fermi liquid that quasiparticles following the rules of Fermi-Dirac statistics.

5.1.1. Derivation

In general, one of QO, the de-Haas van Alphen effect, which is the oscillation of resistivity, introduced in the condensed matter book is as follows[67].

The energy of a free-electron is given by

$$\boldsymbol{p} = \hbar\boldsymbol{k}, \qquad \boldsymbol{E} = \frac{\boldsymbol{p}^2}{2m} = \frac{(\hbar\boldsymbol{k})^2}{2m} \quad \ldots \quad (5.1.1)$$

where $\boldsymbol{k}$ is a wave vector of an electron, m is an electron mass and $\hbar$ is a Planck constant. The equation of motion of a free-electron under the magnetic field $\boldsymbol{B}$ is given by

$$\frac{d\boldsymbol{p}}{dt} = \frac{d}{dt}(\hbar\boldsymbol{k}) = -\frac{e}{c}\boldsymbol{v} \times \boldsymbol{B} \quad \ldots \quad (5.1.2)$$

Assume that the electron is moving in an *x*-*y* plane and applying a magnetic field, $\boldsymbol{B}$, along the z-direction. In this situation, integrate both sides, and then I can obtain

$$\hbar\boldsymbol{k} = -\frac{e}{c}(\boldsymbol{r} - \boldsymbol{r_0}) \times \boldsymbol{B} \quad \ldots \quad (5.1.3)$$

Set, $\boldsymbol{r}_0 = 0$,

$$\boldsymbol{k} = -\frac{e}{\hbar c}\boldsymbol{r} \times \boldsymbol{B} \quad \ldots \quad (5.1.4)$$

Since $\boldsymbol{k}, \boldsymbol{r} \perp \boldsymbol{B}$, I can obtain a relation between an area of motion in real and momentum space,

$$A_k = \frac{e^2B^2}{\hbar^2c^2}A_r \quad \ldots \quad (5.1.5)$$

Using Bohr – Sommerfeld semi-classical quantization,

$$\oint [\hbar\boldsymbol{k} - \frac{e\boldsymbol{A}}{c}] \cdot d\boldsymbol{r} = (\mathrm{n}+\gamma)2\pi\hbar \quad \ldots \quad (5.1.6)$$

where $\nabla \times \boldsymbol{A} = \boldsymbol{B}$, $\boldsymbol{B} = B\ \hat{\boldsymbol{z}}$ and n is an integer. Substituting $\boldsymbol{k} = -\frac{e}{\hbar c}\boldsymbol{r} \times \boldsymbol{B}$, and using the Stokes theorem,

$$\oint \hbar\boldsymbol{k} \cdot d\boldsymbol{r} - \oint \frac{e\boldsymbol{A}}{c} \cdot d\boldsymbol{r} = \oint \hbar(-\frac{e}{\hbar c}\boldsymbol{r} \times \boldsymbol{B}) \cdot d\boldsymbol{r} - \iint_S \frac{e\boldsymbol{B}}{c} \cdot \boldsymbol{n}dS$$

$$= \frac{eB}{c}\oint \boldsymbol{r} \times d\boldsymbol{r} - \frac{eBA_r}{c} = \frac{eBA_r}{c} = (\mathrm{n}+\gamma)2\pi\hbar \quad \ldots \quad (5.1.7)$$

$$\Rightarrow BA_r = (\mathrm{n}+\gamma)\frac{2\pi\hbar c}{e} = (\mathrm{n}+\gamma)\Phi_0 \quad \ldots \quad (5.1.8)$$

where $\Phi_0 = 2\pi\hbar c/\mathrm{e}$ is the magnetic flux quantum. Define magnetic length as $l_B \equiv \sqrt{\frac{\hbar c}{eB}}$, and then *(*5.1.8) is given by

$$BA_r = BA_k {l_B}^4 = (\mathrm{n}+\gamma)\Phi_0 \quad \ldots \quad (5.1.9)$$

$$\Rightarrow A_k {l_B}^2 = 2\pi(\mathrm{n}+\gamma) \quad \ldots \quad (5.1.10)$$

Define A_F as an area of the Fermi surface, and then the *(*5.1.10) is given by,

$$\Delta({A_F}{l^2}_B) = 2\pi \Rightarrow \frac{1}{F} = \Delta\left(\frac{1}{B}\right) = \frac{2\pi e}{\hbar c}\frac{1}{A_F} \quad \ldots \quad (5.1.11)$$

This equation is called the Onsager relation. From this relation, I could get a Fermi surface area using the quantum oscillation frequency *F*.

5.1.2. Geometrical description of QO

When quantization number *n* is fixed, the radius of the Landau cylinder in **k** space becomes large as *B* is increased (Fig. 5.1). The number of the possible

DOS, $D(\varepsilon)d\varepsilon$, is proportional to the area where Landau cylinder and Fermi surface energy region, $\varepsilon_F + d\varepsilon$, overlap. When Landau orbit reaches extrema of the Fermi surface, then the number of DOS also reaches extrema. Therefore, participating electrons in the transport measurement become larger whenever Landau cylinders corresponding to the different quantization numbers reach the extremal orbit of the Fermi surface. The physical quantities (e.g., resistivity, magnetic susceptibility) related to DOS reach maxima, either.

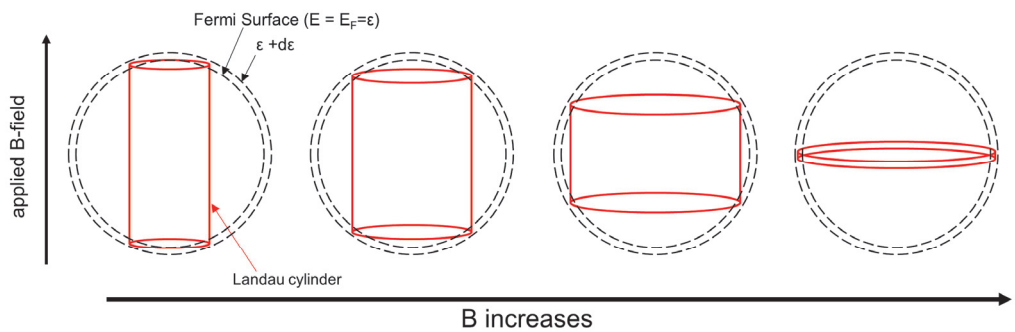

Figure 5.1: The Fermi surface and Landau cylinder under the magnetic field.
The radius of the Landau cylinder is changed by varying the magnetic fields. The farthest to the right image displays the extrema of the overlap region between the Landau cylinder and the Fermi surface.

5.2. Transport measurements on cuprates

In 2007, the Taillefer group reported for the first time that in-plane resistivity oscillates in the underdoped $YBa_2Cu_3O_{7-\delta}$ as the magnetic field increases[65].

After the first observation of QO on underdoped cuprates, QO has been reported from other cuprates, including underdoped $YBa_2Cu_3O_{7-\delta}$ of different doping levels[68], HBCCO[69], overdoped TBCO[70], and electron-doped PCCO[71]. The oscillatory behavior was observed in in-plane and out-of-plane resistivity, contactless resistivity[65,69,72–74] as well as magnetic torque measurements[75]. Previously, these QO phenomena in underdoped *p*-type cuprates were explained in terms of a reconstructed Fermi surface and conventional Fermi liquid theory[75]. Still, such explanations are in debate due to a lack of evidence of a closed Fermi surface in underdoped cuprates at the PG phase. ARPES measurements report a 'Fermi arc'[76–79], which makes a simple Fermi liquid interpretation challenging. In the next section, I suggest a simple but novel approach to explain the QO phenomena entirely in terms of the real space features such as DOSM I presented in the previous chapter. There is an example of the magnetic field dependent oscillations that originated from a real space modulation. Weiss oscillations or commensurability oscillations[80–82] is due to the interplay between the charge carriers' cyclotron orbit and the periodic potential, usually under a weaker magnetic field far before the formation of Landau Levels (LLs)[83]. However, such oscillations cannot explain the oscillations in magnetization observed in QO results on cuprates.

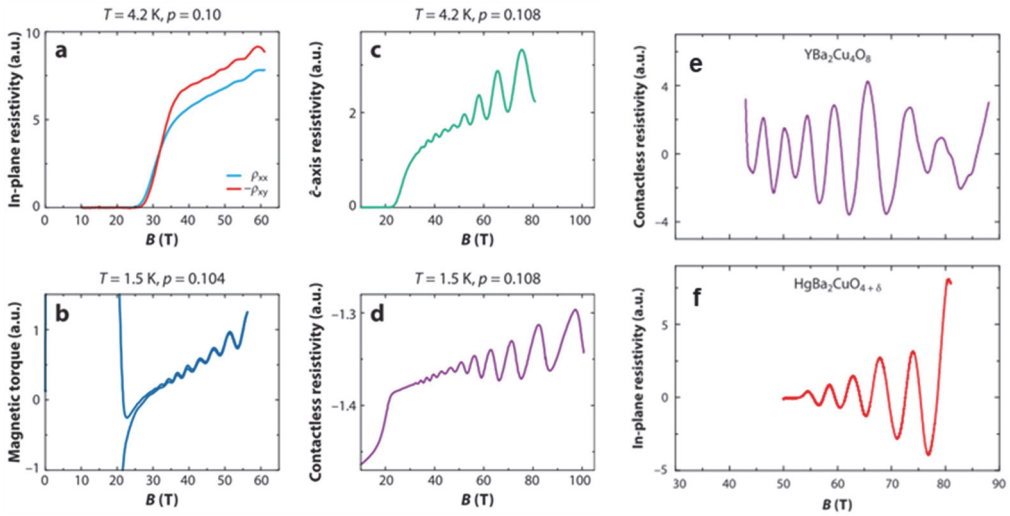

Figure 5.2: The reported QO on cuprates.

(a)–(d) QO results of $YBa_2Cu_3O_{7-\delta}$. (a) In-plane four contact resistivity, (b) magnetic torque, (c) c-axis four contact resistivity, and (d) contactless resistivity measured using a resonant proximity detection oscillator. QO results of (e) $YBa_2Cu_4O_8$, and (c) $HgBa_2CuO_{4+\delta}$. Reproduced from [84].

5.3. Real space model for QO

If the two-dimensional system is subjected to extremely low temperature –small thermal energy– and a strong magnetic field, the DOS of charged quasiparticle in a system is rearranged, as shown in Figure 5.2. In such circumstances, many phenomena, including the quantum Hall effect[85], the de Hass van-Alphen effect[86], and the Aharonov - Bohm effect[87], can emerge. In this section, I will introduce a very simple approach to how QO can be represented in real space.

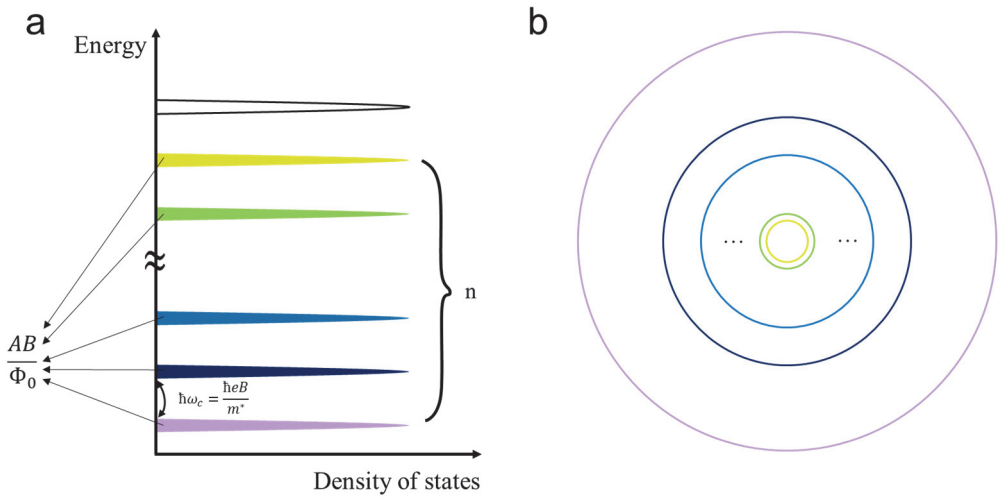

Figure 5.3: LLs with corresponding to Landau orbits of real space.

The higher LL has a smaller Landau orbit. (a) LLs and corresponding (b) Landau orbits are represented in the same colors.

As above, once the Landau quantization sets in cuprates, which are non-superconducting at a high magnetic field as in QO experiments, one needs to consider a new set of sum rules. In low temperatures, the charge carriers or quasiparticles fill-up the LLs starting from the lowest LL. At a given magnetic field B and a sample size of A, each LL has the number of occupiable states of $\frac{AB}{\Phi_0}$, where $\Phi_0 = \frac{h}{e}$ is a flux quantum. Then the total number of the quasiparticles N should satisfy

$$N = n\frac{AB}{\Phi_0} + m \quad \ldots \quad (5.3.1)$$

where n is the index of the highest occupied LL, and m is an integer satisfying $-\frac{AB}{2\Phi_0} \leq m(B) \leq \frac{AB}{2\Phi_0}$. That is, the occupation of the LLs is completely determined by two integers: n and m. Rearranging (5.3.1), I derive

$$A_{nm}\frac{n}{\Phi_0} = \frac{1}{B} \quad \ldots \quad (5.3.2)$$

where $A_{nm} \equiv \frac{A}{N-m}$ represents roughly an area per quasiparticle or size of an orbit of a quasiparticle in the n_{th} LL, which changes as n and m changes according to the variation of B (Fig. 5.4). If the orbit or circumference of the A_{nm} corresponds to a specific loop where the LDOS is high, the number of orbiting quasiparticles will increase greatly, resulting in an increase of the relevant magneto-transport quantities, including magnetization and in-plane conductivity. Let the area of such a high LDOS loop be A_{reson}. Varying n and B, I have a new resonance condition of $A_{reson} = A_{nm}$, or

$$A_{reson} = \Phi_0 \Delta\left(\frac{1}{B}\right) = \frac{\Phi_0}{F} \quad \ldots \quad (5.3.3)$$

where $F \equiv 1/\Delta\left(\frac{1}{B}\right)$ is a magneto frequency. From this relation, I can estimate the size of A_{reson}.

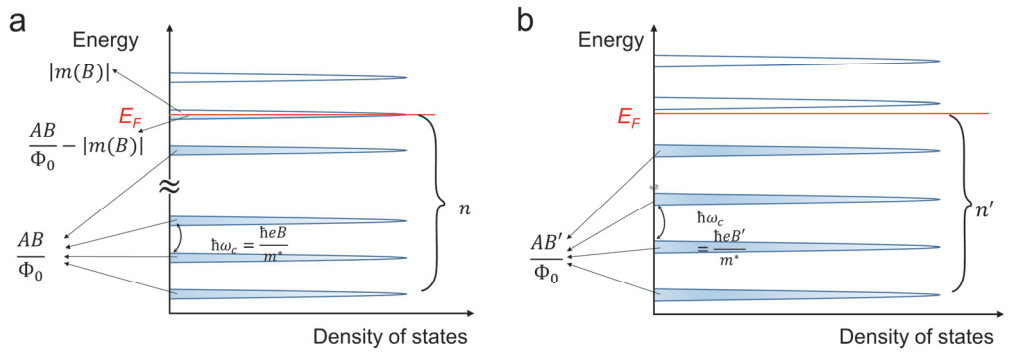

Figure 5.4: Cartoon images of the LLs.

The Fermi energy is at the n_{th} Landau quantization energy. Larger the magnetic field, the greater the number of density of states ($\frac{\boldsymbol{AB}}{\boldsymbol{\Phi_0}}$) of each LL, and the larger the energy interval between LLs ($\hbar\boldsymbol{\omega_c} = \frac{\hbar\boldsymbol{eB}}{\boldsymbol{m^*}}$). The increase of the magnetic field ($B < B'$) reduces the number of filled LLs ($\boldsymbol{n}$) since the total number of electrons N in the sample is fixed. Degeneracy of the electrons also increases as the magnetic field is increased.

5.4. Real space resonance orbits of cuprates

Using the (5.3.3) and the value of $F \sim 530$ T reported from the QO result on an underdoped $YBa_2Cu_3O_{7-\delta}$ [65], I obtain an area $7.8 \times 10^{-18}\ m^2$ for the A_{reson}. This value is comparable to an area of $8a_0 \times 8a_0$. This area corresponds to red squares in Fig. 5.6 in my data on $Bi_2Sr_2CaCu_2O_{8+\delta}$. The A_{reson} size fits remarkably well to a DOSM mesh, which is omnipresent in energy near the Fermi energy even at the magnetic field of 13 T in the HUD $Bi_2Sr_2CaCu_2O_{8+\delta}$, as shown in Fig. 4.9. The resonance between the high DOS area in the modulations and the Landau orbits is illustrated in Fig. 5.5, which show the orbit of a quasiparticle in the highest LL containing a Fermi level (black square)

coinciding with (Fig. 5.5a), and non-coinciding (Fig. 5.5b) with a given $8a_0 \times 8a_0$ pattern (red square). This simple model captures most of the features of QO results, including not limited to a dominating $\Delta\left(\frac{1}{B}\right)$, but an increase of the oscillation amplitude (due to the increasing of DOS of LL with increased B) without an assumption of a well-defined closed Fermi surface.

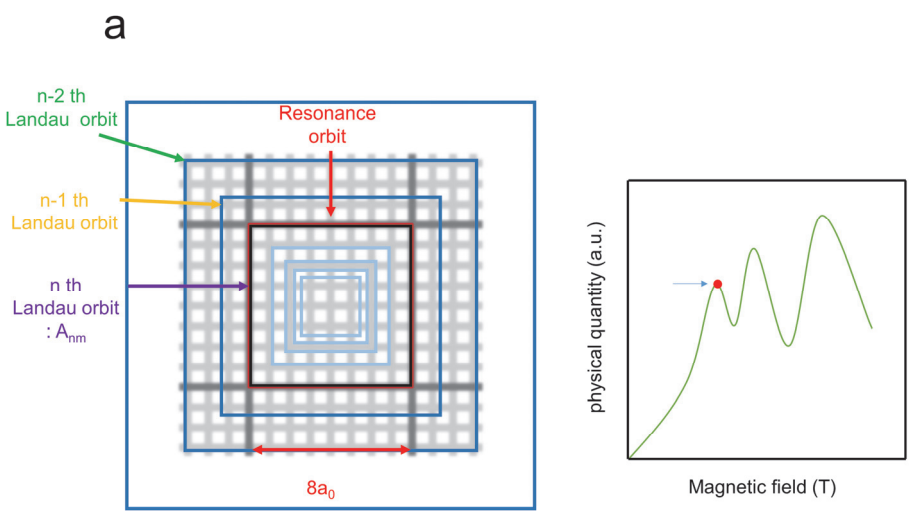

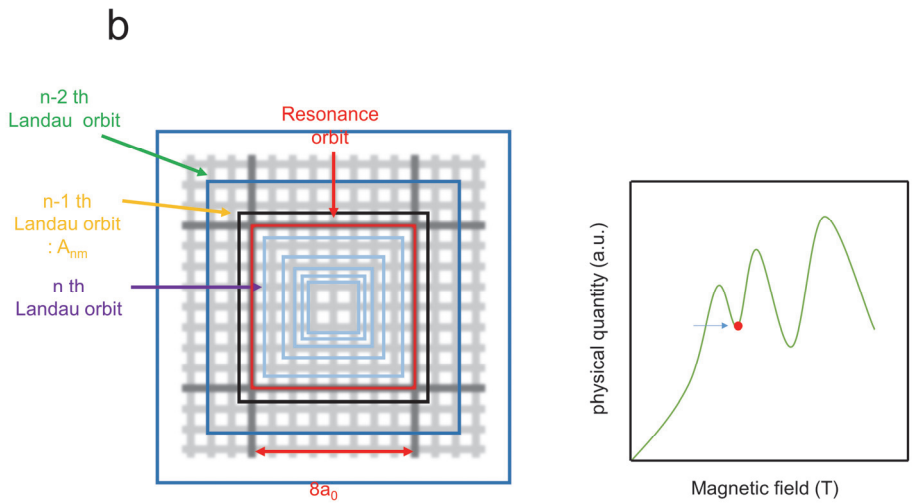

Figure 5.5: The Landau orbits and resonance orbits in real space.

As the Landau level number *n* increases, the area of the Landau orbits decreases as $\boldsymbol{A_{nm} \propto \frac{1}{n}}$ ((5.3.2)) at a fixed *B*. Since the orbit area is inversely proportional to the magnitude of the magnetic field, the higher the magnetic field, the smaller the orbit for a fixed $\boldsymbol{n}$. (a) When a Landau orbit (black square, $\boldsymbol{A_{nm}}$) coincides the resonance orbit in real space (red square, $\boldsymbol{A_{res}}$), the physical quantities related to the electron DOS can diverge, resulting in a local maximum of those quantities (a, small). (b) As the magnetic field continues to grow, the $\boldsymbol{n_{th}}$ Landau orbit moves inward from the resonance orbit, and the next $\boldsymbol{(n-1)_{th}}$ Landau orbit approaches the resonance orbit. When the resonance orbit is located between two Landau orbits, the value of the physical quantities is also located between the local maxima (b, small).

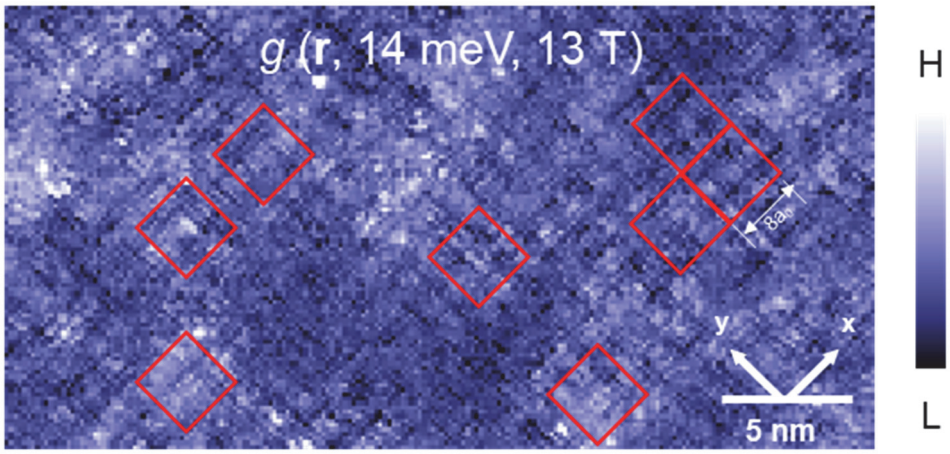

Figure 5.6: The resonance orbits on the *g*(r, 14 meV, 13 T) image of the HUD $Bi_2Sr_2CaCu_2O_{8+\delta}$ in the 13 T.

As the magnetic field goes beyond H_{c2}, the superconducting state will change to the normal state, and the patterns in vortices will cover the entire image. Then the resonance orbit appears throughout the image. Resonance orbits are indicated as red squares on a differential conductance image g (r, E = 14 meV, B = 13 T) of the HUD $Bi_2Sr_2CaCu_2O_{8+\delta}$.

5.5. Satellite peaks of QO

The FT of the QO data in cuprates often shows other auxiliary frequencies besides the primary frequency. In the case of $YBa_2Cu_3O_{7-\delta}$, there is a peak corresponding to the primary frequency (F) of 530 T, and small peaks corresponding to 440 T and 620 T on both sides of the primary F [84]. My model for QO could explain that even a cause of the reported small side oscillations[74,75,88]. As with the resonance orbit obtained by the primary F, the corresponding A_{res} can be obtained from both peaks, and the ratio of this

resonance area to the primary resonance area A_{res} is $\frac{53}{44}(\cong 1.2)$ and $\frac{53}{62}(\cong 0.84)$ for 440 T and 620 T respectively. This value is almost equal to the area ratio of the rectangle that adds or subtracts $\frac{4}{3}a_0$ of $\mathbf{q_5}$* to one side of the square corresponding to the resonance orbit of twice $\mathbf{q_1}$* DOSM (Fig. 5.7). Therefore, it is also possible to explain the presence of the auxiliary peaks by $\mathbf{q_5}$* DOSM.

There is yet another additional small peak, not a primary peak nor a satellite peak. In the case of $YBa_2Cu_3O_{7-\delta}$ of the doping levels around $p = 0.11$ or 0.125, the primary F of QO is reported to be 570 T, and the F of the small peak is also found around 250 T [68]. The ratio between primary and small peak is $\frac{570}{250} = 2.28$. It means that if the size of the resonance orbit corresponding to the primary F is a $8a_0 \times 8a_0$ (four by four of the four unit-cell checkerboard plaquettes), then the size of the orbit corresponding to the small F is $12a_0 \times 12a_0$ (nine by nine of the four unit-cell checkerboard plaquettes), as illustrated in Fig. 5.8. In this argument, my model not only explains the multiple QO frequencies but also predicts more frequencies unreported experimentally.

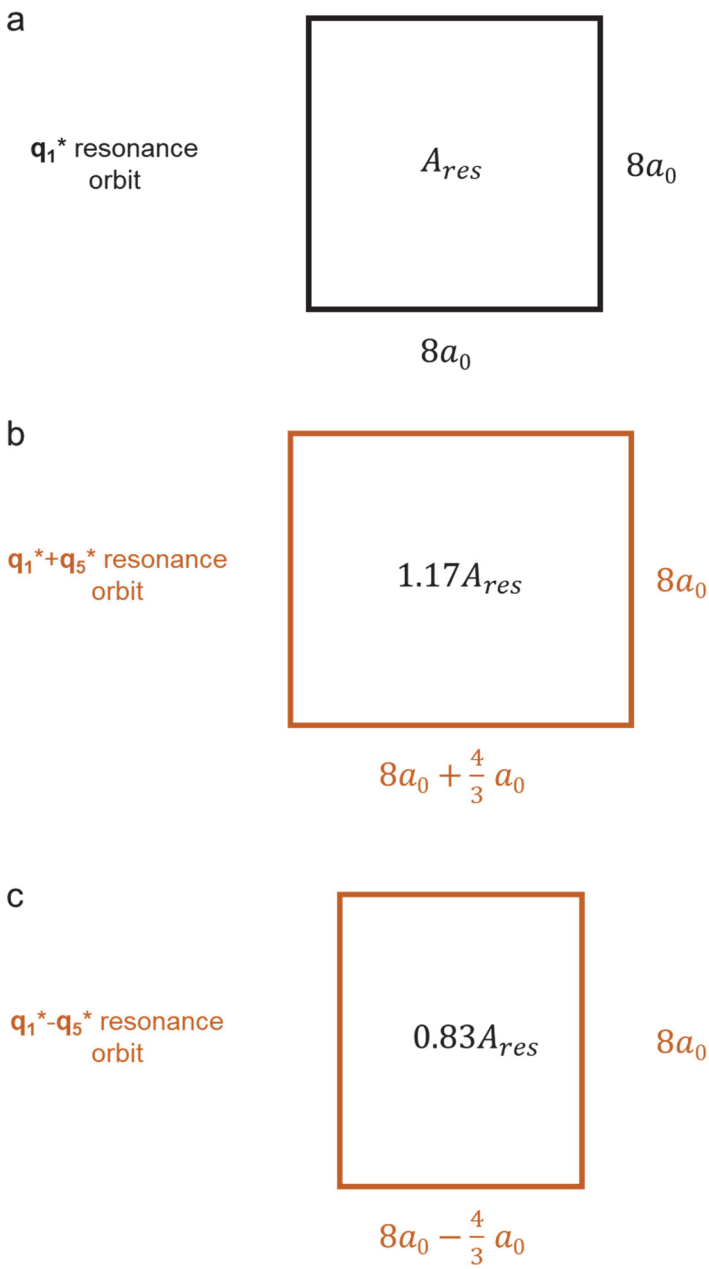

Figure 5.7: The resonance orbits for satellite peaks.

(a) The resonance orbit corresponding to the primary *F* 530 T. Resonance orbits corresponding to satellite peaks (b) 440 T and (c) 620 T

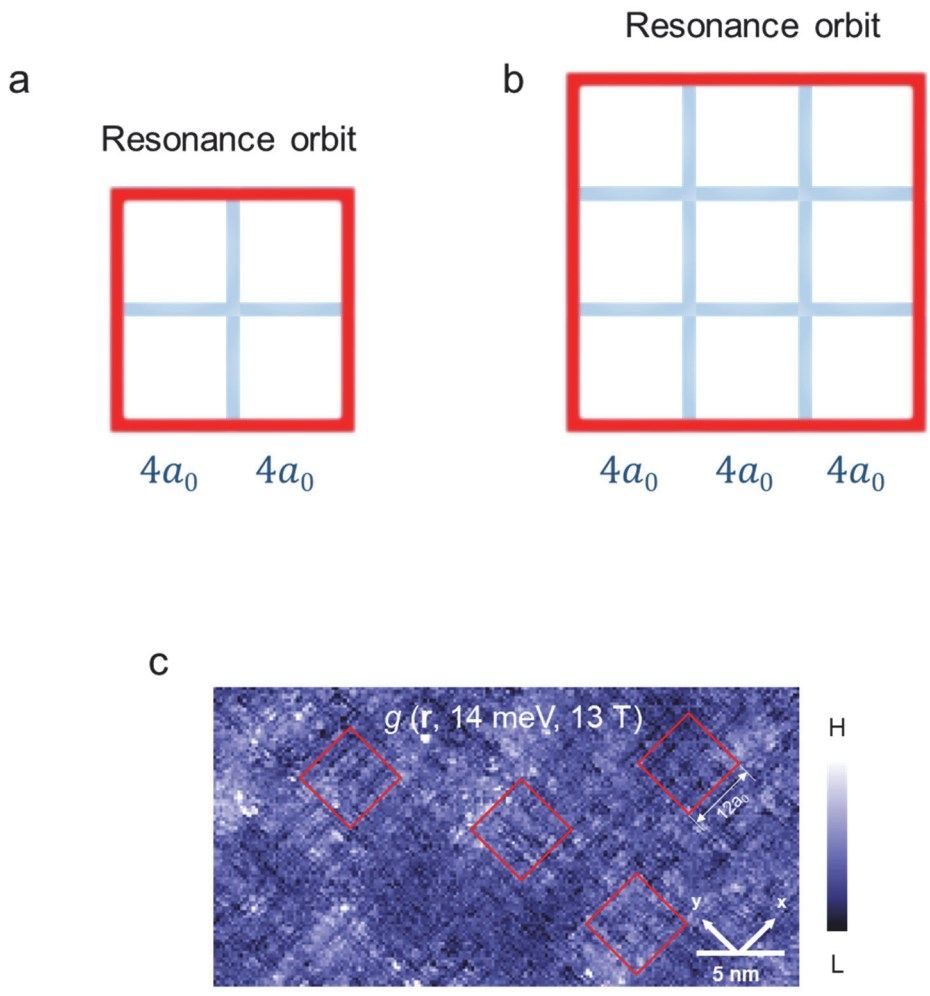

Figure 5.8: Cartoons of two different resonance orbits.

(a) A resonance orbit of the area $8a_0 \times 8a_0$, as in Fig. 5.5 containing four $4a_0$ plaquettes. (b) A resonance orbit of $12a_0 \times 12a_0$ containing nine $4a_0$ plaquettes. Such larger A_{res} corresponds to the small F = 250 T in [68]. (c) Resonance orbits of $12a_0 \times 12a_0$ are presented on a $g(\mathbf{r}, E = 14$ meV, $B = 13$ T) of the HUD $Bi_2Sr_2CaCu_2O_{8+\delta}$.

5.6. Summary

In the previous chapter, I observed a *particle-hole* asymmetric dispersing DOSM in the HUD $Bi_2Sr_2CaCu_2O_{8+\delta}$ under the magnetic field. In this chapter, I used this observation to build a model for describing QO in real space.

Several transport measurements, including QO, predict the presence of electron pockets on fermi surfaces predicted. However, it has not been well explained in **k** space because there is no spectroscopic evidence for electron pockets. For this reason, I suggested explaining QO in real space using DOSM. To do this, I first explained how QO appears in the model of real space. I showed that QO occurs when the resonance orbits and Landau cylinders in real space meet with magneto frequency *F*. Using this model, I calculated the resonance orbit area, A_{res} from the QO results. The orbit area was two times of DOSM I observed in the HUD $Bi_2Sr_2CaCu_2O_{8+\delta}$. The model also explained the results of the other auxiliary peaks observed in the transport measurements. Besides, the DOSM does not require a Fermi surface reconstruction nor closed Fermi surface as proposed previously.

Chapter 6.

Density of States Modulation on $Bi_2Sr_2CaCu_2O_{8+\delta}$ above T_c

STM measurements on high-T_c superconducting materials show a variety of modulations below and above T_c. It is well established that a QPI pattern is observed below T_c due to the scattering of the quasiparticles off the imperfections of the crystalline structure such as impurities and supermodulations[89]. However, above T_c at the PG distinctive modulation patterns were observed in cuprates[90,91] and in some ferropnictides[92] that are commonly referred to as CDW or spin density wave, which is static by energy. In this chapter, I introduce the DOSM of $Bi_2Sr_2CaCu_2O_{8+\delta}$ above T_c, which has a similar periodicity and features which are almost identical to those under magnetic fields. The DOSM above T_c has an energy dependency, resiliency to structural property and disorder, and semi long-range order. These features are distinctive features from those of CDW and normal QPI. Besides, I show the

correlation analysis to obtain the length scale of DOSM. This correlation results show that extinguished long-range order of patterns, the strongest and coherent patterns near Fermi energy, and continuously changing with energy. Moreover, I show the result of comparing the DOSM in $Bi_2Sr_2CaCu_2O_{8+\delta}$ to $Sr_3(Ru_{1-x}Ti_x)_2O_7$ which has the normal QPI.

6.1. SI-STM images above T_c

To observe and analyze the modulations in the PG phase more precisely, I used a variable temperature SI-STM. I performed the measurements on a HUD $Bi_2Sr_2CaCu_2O_{8+\delta}$ single crystal with a T_c of 40 K. The sample was cleaved in the cryogenic ultrahigh vacuum, and topographic and spectroscopic images were taken simultaneously at 55 K.

In Fig. 6.1, *dI/dV* images in real space, $g(\mathbf{r}, V)$ (Fig. 6.1a–f) and their FT image, $g(\mathbf{q}, V)$ (Fig 6.1g–l), of the HUD $Bi_2Sr_2CaCu_2O_{8+\delta}$ are shown in the bias range from 24 mV to -36 mV. For $g(\mathbf{r}, V)$, the most notable feature is a strong modulation in the LDOS along approximately 45 and 135 degrees to the horizontal direction *throughout* the FOV, despite their imperfect regularity. These sweeping patterns ($\mathbf{q_1}$* modulation) are shown not only in the particle state but in the hole state.

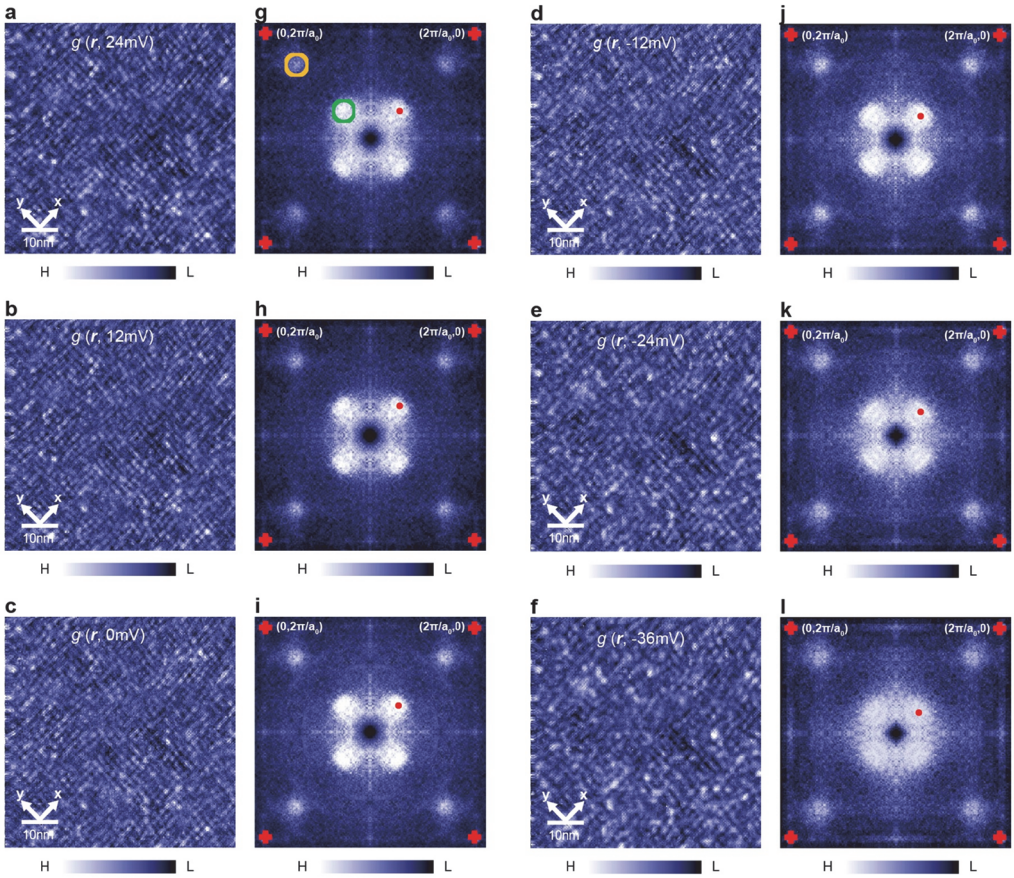

Figure 6.1: Differential conductance images in real space *g*(r, *V*) and its 2DFT images in q space *g*(q, *V*) of the HUD $Bi_2Sr_2CaCu_2O_{8+\delta}$

(a)-(f) *g*(**r**, *V*) with 54 nm × 54 nm FOV. Spatial resolution is approximately 2 Å. From (a) to (f)**,** the bias changes from 24 mV to -36 mV at 12 mV intervals. The DOSM is seen along with Cu-O-Cu bonding directions, *x* and *y*. These modulations are not perfectly uniform but spread across the whole FOV. H, high; L, low. (g)-(l). FT images of (a)-(f). Red crosses represent Bragg peaks (**q** = ($2\pi/a_0$, 0); (0, $2\pi/a_0$)). For clarity, the images were symmetrized in horizontal and vertical directions. There are two peaks, $\mathbf{q_1}$* (green circle in Fig. 6.1g, **q** ≈ 0.24 ($2\pi/a_0$, 0); 0.24 (0, $2\pi/a_0$)) and $\mathbf{q_5}$* (yellow circle in Fig. 6.1g, **q** ≈ 0.7 ($2\pi/a_0$, 0); 0.7 (0, $2\pi/a_0$)) along $\mathbf{q_x}$ and $\mathbf{q_y}$ directions. Since the corresponding signature of $\mathbf{q_5}$* is hardly found in real space image, I consider $\mathbf{q_1}$* only.

The peaks of Lorentzian fitting to $\mathbf{q_1}$* are shown as red dots. From 24 mV to -36 mV bias, $\mathbf{q_1}$* moves toward the center and shows a particle-hole asymmetric dispersion.

6.2. Properties of DOSM above T_c

After 2DFT analysis done on the SI-STM PG data, I have found $\mathbf{q_1}$* modulation has several unexpected properties, not like CDW or normal QPI.

6.2.1. Global character of DOSM

The nonlocality of the $\mathbf{q_1}$* patterns in the PG $Bi_2Sr_2CaCu_2O_{8+\delta}$ becomes more apparent when I compare them to the QPI patterns obtained from the $Sr_3(Ru_{1-x}Ti_x)_2O_7$[93]. Figure. 6.2 shows $g(\mathbf{r}, V)$ and $g(\mathbf{q}, V)$ of the $Sr_3(Ru_{1-x}Ti_x)_2O_7$ at 4.2 K. For $g(\mathbf{r}, V)$ (Fig. 6.2c), ripple-like patterns responsible for the peaks appearing in $g(\mathbf{q}, V)$ (Fig. 6.2d) exist only locally around the Ti impurities. Surprisingly, even with this local character of the patterns in the $Sr_3(Ru_{1-x}Ti_x)_2O_7$, four-fold symmetric peaks can be seen in $g(\mathbf{q}, V)$ as clearly as for the $Bi_2Sr_2CaCu_2O_{8+\delta}$ (Fig. 6.2b). This comparison between two oxides implies that only an analysis of the real space image $g(\mathbf{r}, V)$ can distinguish the non-local patterns, as observed for the PG $Bi_2Sr_2CaCu_2O_{8+\delta}$, from the highly local patterns, as observed for the $Sr_3(Ru_{1-x}Ti_x)_2O_7$ (Fig. 6.2c-d), whereas a $\mathbf{q}$ space analysis alone cannot be used for this task.

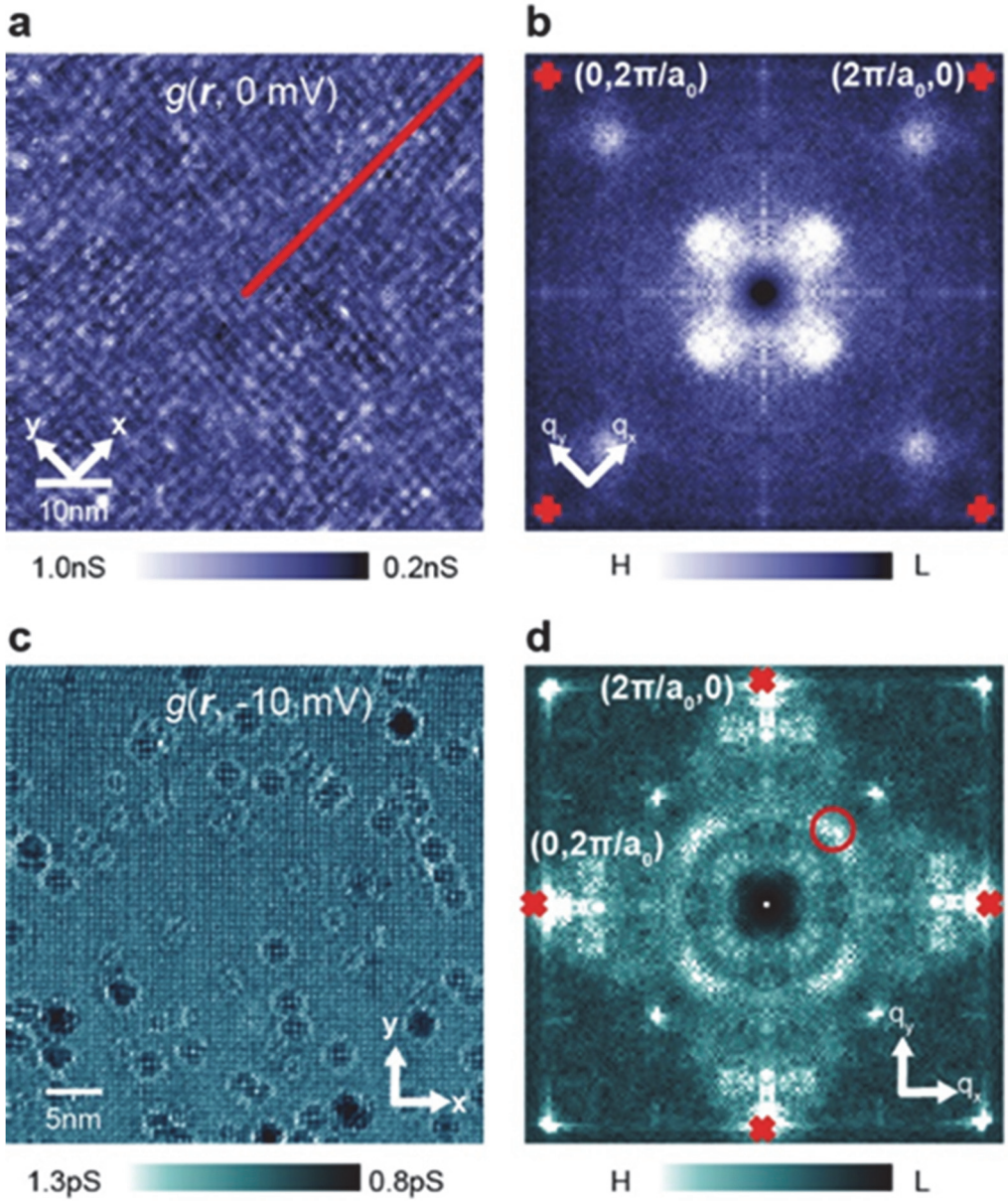

Figure 6.2: Images to compare a global DOSM of $Bi_2Sr_2CaCu_2O_{8+\delta}$ to a local QPI of the $Sr_3(Ru_{1-x}Ti_x)_2O_7$.

(a) The differential conductance image in real space, $g(\mathbf{r}, 0\text{ mV})$ of $Bi_2Sr_2CaCu_2O_{8+\delta}$ with a 54 nm *x* 54 nm FOV. Unlike for $Sr_3(Ru_{1-x}Ti_x)_2O_7$ (Fig. 6.2c), there is only global modulation without any local random impurity sign. There are no supermodulation or

impurities such as Zn that can be found in the superconducting phase at the Fermi level. (b) The FT image of (a). A center peak was removed by Gaussian subtraction. Four-fold symmetry peaks ($\mathbf{q_1}$* and $\mathbf{q_5}$*) are visible and match with the modulation in real space. (c) The differential conductance image in real space, $g(\mathbf{r}, -10\ \text{mV})$ of the $Sr_3(Ru_{1-x}Ti_x)_2O_7$ with a 29 nm *x* 29 nm FOV. Spatial resolution is approximately 1.1 Å. Circle patterns with white rings around Ti impurities are located randomly in the entire FOV. Impurity diameters are in a 15- 30 Å range, and with the size-dependent on the bias. (d) The FT image of (c). Red cross marks represent Bragg peaks. The red circle in the diagonal direction is associated with impurity patterns in real space[93]. These four-fold symmetry peaks vary depending on the energy as the size of the patterns changes. No indications can be observed for differentiating the global patterns and the local patterns in **q** space.

6.2.2. Energy dependence of DOSM

Another distinctiveness of the $\mathbf{q_1}$* modulation can be found from an examination of $g(\mathbf{q}, V)$. A clear dispersion of $\mathbf{q_1}$* peaks (red dots in Fig.6.1) is visible, and the dispersion shows a particle-hole asymmetry that is qualitatively different from the QPI features below T_c (Fig. 4a). Such asymmetric dispersion of the $\mathbf{q_1}$* suggests that the modulation in the PG $Bi_2Sr_2CaCu_2O_{8+\delta}$ is not a conventional CDW [6,90,94,95] , especially considering the occurrence of the patterns in the positive bias image (Fig. 6.1a and b) where no charge carriers are present, thus making a simple association of the $\mathbf{q_1}$* modulation in the positive bias side with the CDW unlikely[91].

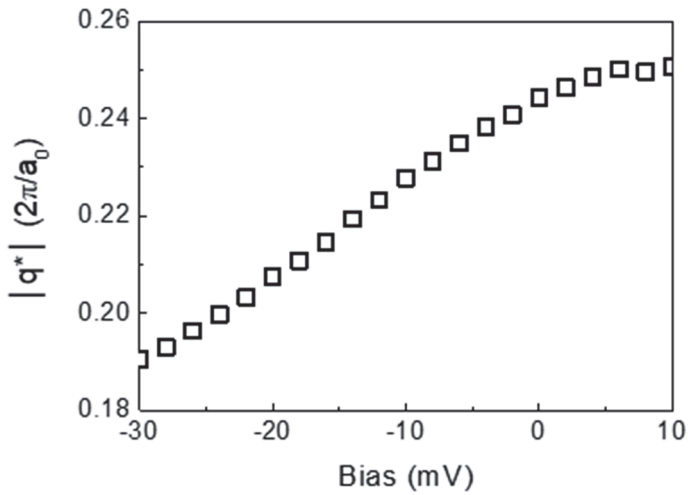

Figure 6.3: The energy dependence of $\mathbf{q_1}$*.

By increasing bias, $\mathbf{q_1}$* moves away from the center and reaches a maximum near the Fermi energy. Unlike the QPI in the superconducting phase, it shows an apparent particle-hole asymmetry.

6.2.3. Resiliency of DOSM

The next feature is that the $\mathbf{q_1}$* modulation is resilient to structural disturbance and other sources of disorders. First, I could not locate most of the impurity sites from the $g(\mathbf{r}, V)$ of the PG $Bi_2Sr_2CaCu_2O_{8+\delta}$. Natural impurities such as Zn are unavoidable in the process of a single crystalline $Bi_2Sr_2CaCu_2O_{8+\delta}$, and a few impurities are always visible when I examine the $g(\mathbf{r}, V)$ of a near-optimally doped $Bi_2Sr_2CaCu_2O_{8+\delta}$. To further investigate this point, I checked the $g(\mathbf{r}, V)$ from the HUD $Bi_2Sr_2CaCu_2O_{8+\delta}$ below T_c and found that I was unable to find Zn impurities from the "black regions"[17] where the local superconducting gaps

defined by the energy of the coherence peaks are relatively large (>70 meV). This global $\mathbf{q_1}$* modulation appears to ignore such local impurities simply.

Figure 6.4b and d are gap images of a near-optimally doped and HUD $Bi_2Sr_2CaCu_2O_{8+\delta}$ in the superconducting phase. Color scales representing 20 meV < Δ < 70 meV are chosen. As the hall doping of $Bi_2Sr_2CaCu_2O_{8+\delta}$ increases, the average gap value is reduced. In Fig. 6.3b, the black region is seldom visible, whereas in Fig. 6.4d, over half of the figure is covered by the black regions. Bright spots in Fig. 6.4a indicate Zn impurities. Comparing this with Fig. 6.4b shows that the sites of bright spots have lower gap values. Besides, impurities are almost invisible in Fig. 6.4c, which shows the image of the HUD $Bi_2Sr_2CaCu_2O_{8+\delta}$ at the zero bias, which is almost covered with black regions. The sign of impurities may be hidden where the superconducting phase is weakening locally.

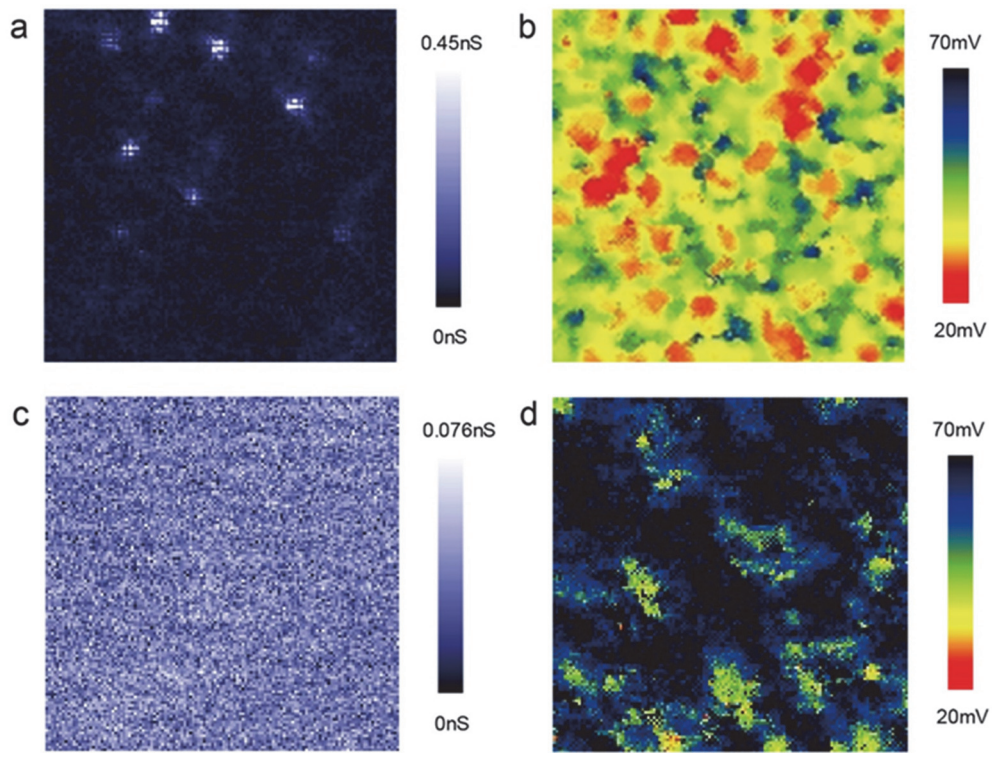

Figure 6.4: Gap and zero bias *g(*r, 0 mV) images with different doping levels.
(a) $g(\mathbf{r}, 0\ \text{mV})$ of the optimally doped $Bi_2Sr_2CaCu_2O_{8+\delta}$ below T_c White spots are Zn impurities. (b) A gap image of (a). Compared to Zn sites in (a), Zn is located where the gap value is not large. (c). $g(\mathbf{r}, 0\ \text{mV})$ of the HUD $Bi_2Sr_2CaCu_2O_{8+\delta}$ below T_c. No impurity sign is observed. (d) A gap image of (c).

I also found that the supermodulation, which is a strong structural property that even affects the gap size below T_c[41], is suppressed when the DOSM is shown. Figure 6.5 is $g(\mathbf{r}, E)$ images of the HUD $Bi_2Sr_2CaCu_2O_{8+\delta}$ above (Fig. 6.5a) and below T_c (Fig. 6.5b). There are clear perpendicular lines on the differential conductance image and its FT image below T_c. On the other hand, I cannot find any supermodulation sign in images above T_c.

In Fig. 6.6, there is no DOSM at -80 mV bias, although supermodulation and its corresponding peaks (red dots) in **q** space are visible. The relative intensity of supermodulation peaks to $\mathbf{q_1}$* peaks varies with energy (Fig. 6.6b). From -80 mV to 80 mV, the ratio between $\mathbf{q_1}$* and supermodulation peaks decreases until near the Fermi energy and then increases again (Fig. 6.6c). Since the supermodulation is due to a bulk property of a $Bi_2Sr_2CaCu_2O_{8+\delta}$[41], this may show that the DOSM above T_c is very resilient to suppress the crystalline structure.

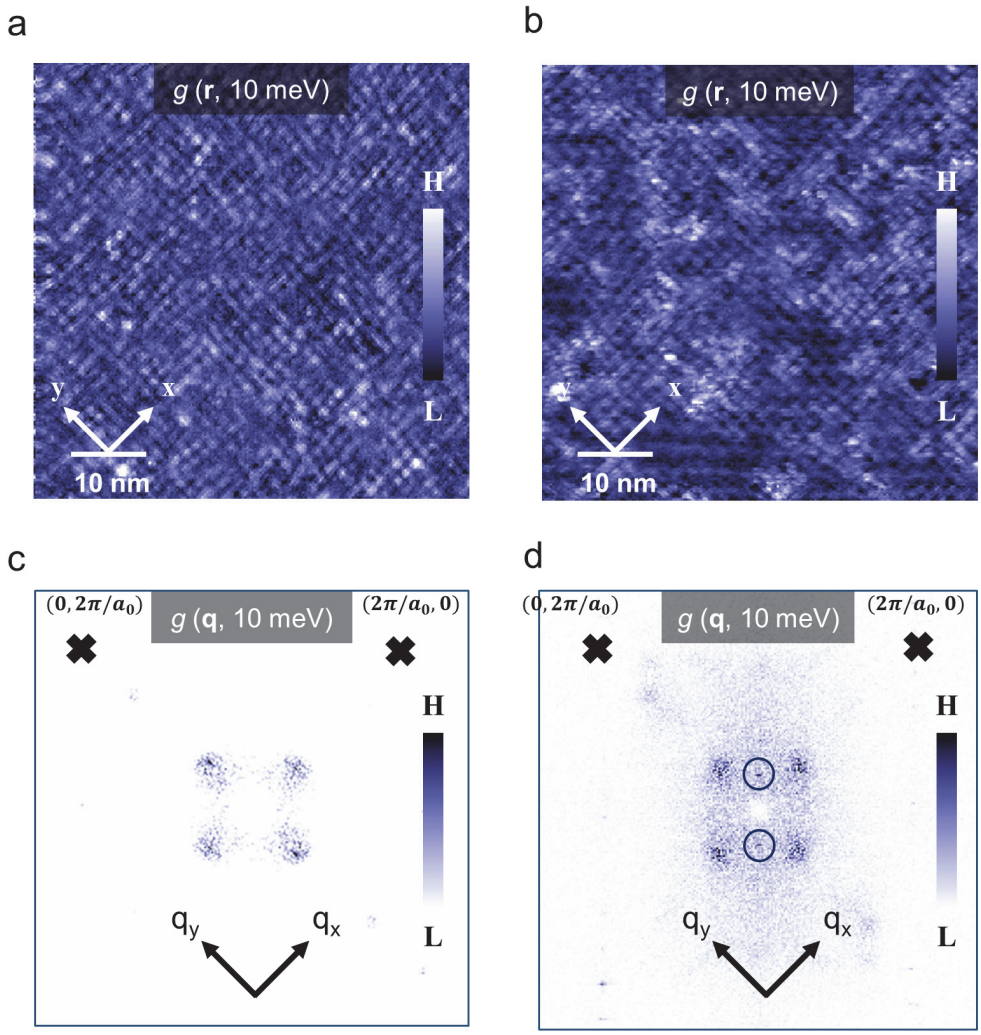

Figure 6.5: Differential conductance images and its 2DFT images with the same doping level below and above T_c at 10 meV.

Differential conductance images of the HUD $Bi_2Sr_2CaCu_2O_{8+\delta}$ (a) above T_c and (b) below T_c. (c) The 2DFT of (a). (d) The 2DFT of (b). The supermodulation, clear horizontal lines in g image (b) and its corresponding peaks in **q** space (d) are shown below T_c data. Contrarily, any sign of supermodulation does not appear above T_c data, (a) and (c). Bragg peaks are presented as black crosses in (c) and (d).

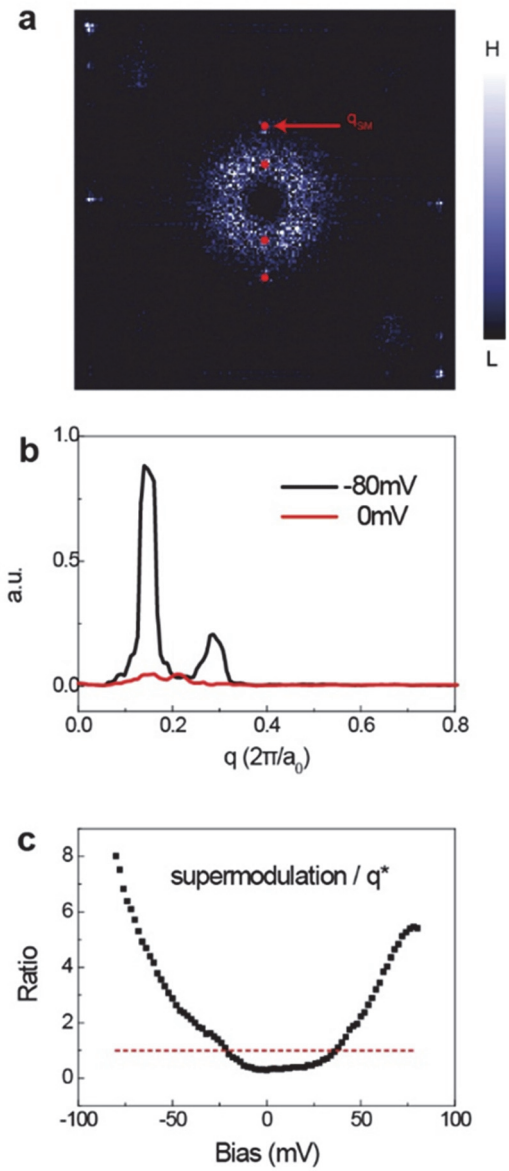

Figure 6.6: The relative intensity between supermodulation peaks and q_1*.

(a) The FT of the differential conductance image at -80 mV bias. There are clear supermodulation peaks and their harmonics, and there is not four-fold symmetry $\mathbf{q_1}$* peak. (b) The comparison of the amplitude of supermodulation peaks when -80 mV and 0 mV bias. Two peaks in -80 mV are peaks of supermodulation and their harmonics. No

definitive sign of supermodulation peak is found at zero bias. (c) The ratio between the intensity of $\mathbf{q_1}$* and supermodulation peaks. The red dotted line shows that $\mathbf{q_1}$* and supermodulation have the same magnitudes. It has a minimum near the Fermi energy, similar to the results of the correlation length analysis in chapter 6.7.

6.2.4. Similar features to DOSM in other conditions and materials

This $\mathbf{q_1}$* modulation shows a striking similarity to the modulation that is observed under the magnetic fields and from the "black regions" of the underdoped $Bi_2Sr_2CaCu_2O_{8+\delta}$ below T_c[17]. Moreover, a qualitatively similar pattern with a unidirectional character was observed in the ferropnictide $Ca(Fe_{1-x}Co_x)_2As_2$[92], implying that the global DOSM not only exists in cuprates but may also exist in other high-T_c materials as well. These observations indicate that when the superconductivity becomes weakened, the $\mathbf{q_1}$* patterns become more apparent and are ubiquitous in vortex cores, PG, underdoped and near parent materials. It seemingly suggests that these $\mathbf{q_1}$* modulations are a signature of a competing order rather than a superconducting order[59] However, recently a wave-like pattern with a nonzero **q** similar to the $\mathbf{q_1}$* was observed from the direct measurement of the Cooper-pair density by using scanning Josephson tunneling microscopy[96]. The comparative study of these PDW below T_c and the $\mathbf{q_1}$* modulation above T_c in the same sample and on the same FOV has not yet been reported, but, remarkably, both modulations occur at the similar **q** vectors (~0.25 $2\pi/a_0$) and exhibit non-locality. Striking differences between PDW and the $\mathbf{q_1}$* modulation are also evident. Although the Zn impurities can be located in PDW (measured at the Fermi level) by the suppressed pair density,

they are not above T_c.

6.3. DOSM: not the octet model of Bogoliubov QPI

The dispersion and incommensurate behavior indicate that the $\mathbf{q_1}$* modulation is also coupled to the **k** space electronic structure. The most common interpretation to date is that the $\mathbf{q_1}$* modulation is caused by the interference between the endpoints of the Fermi arcs[62]. The value of the $\mathbf{q_1}$* is similar to the distance between the endpoints of the nearest neighbor Fermi arcs. This explanation is an identical logical structure to that of the octet model of Bogoliubov QPI in the superconducting phase[8]. Since ARPES measurements of PG cuprates show a disappearance of spectral weights near the anti-nodal region in **k** space or "Fermi arcs"[76–79], it seems natural to exclude the involvement of the anti-nodal quasiparticles from the interpretation of the $\mathbf{q_1}$* modulations. However, the lack of the possible interference peaks other than the $\mathbf{q_1}$* or $\mathbf{q_5}$* peaks between the tips of the Fermi arcs (Fig 6.7) can hardly be ignored, in fact, it significantly weakens such arguments. In conclusion, the **k** space origin of the DOSM above T_c needs further study.

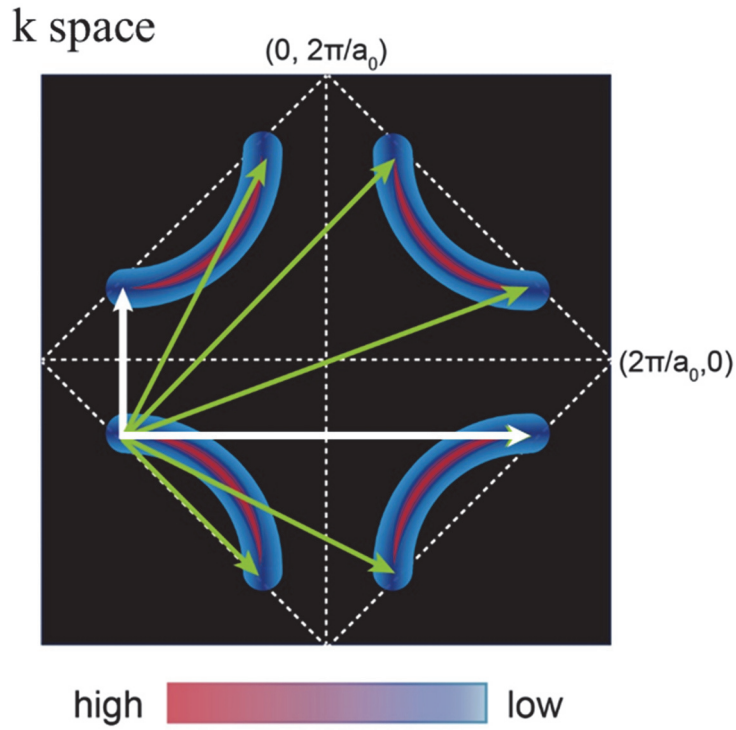

Figure 6.7: Possible interference vectors of the Fermi arcs.

White arrows are regarded as the origin of DOSM $\mathbf{q_1}$* (short) and $\mathbf{q_5}$* (long). The other five green arrows are not shown in the PG data of SI-STM.

6.4. Ordered State

Dispersiveness of DOSM is a representative property that is distinguished from the CDW. As has been mentioned, it is a different kind of modulation from the octet model QPI. Then, is this modulation a new order or a kind of interference? I found that there is a simple definition of the long-range order state from the statistical book of James Sethna[97]. If the value of the correlation function of a

system decays exponentially to non-zero, then this system has a long-range order with correlation length ξ. Similarly, I can define a disordered system or quasi-long-range ordered system if the correlation function decays exponentially to zero or to zero following a power-law. A well-known example of the long-range order system is the ferromagnetic or antiferromagnetic sample below T_{Curie} (Fig 7.1).

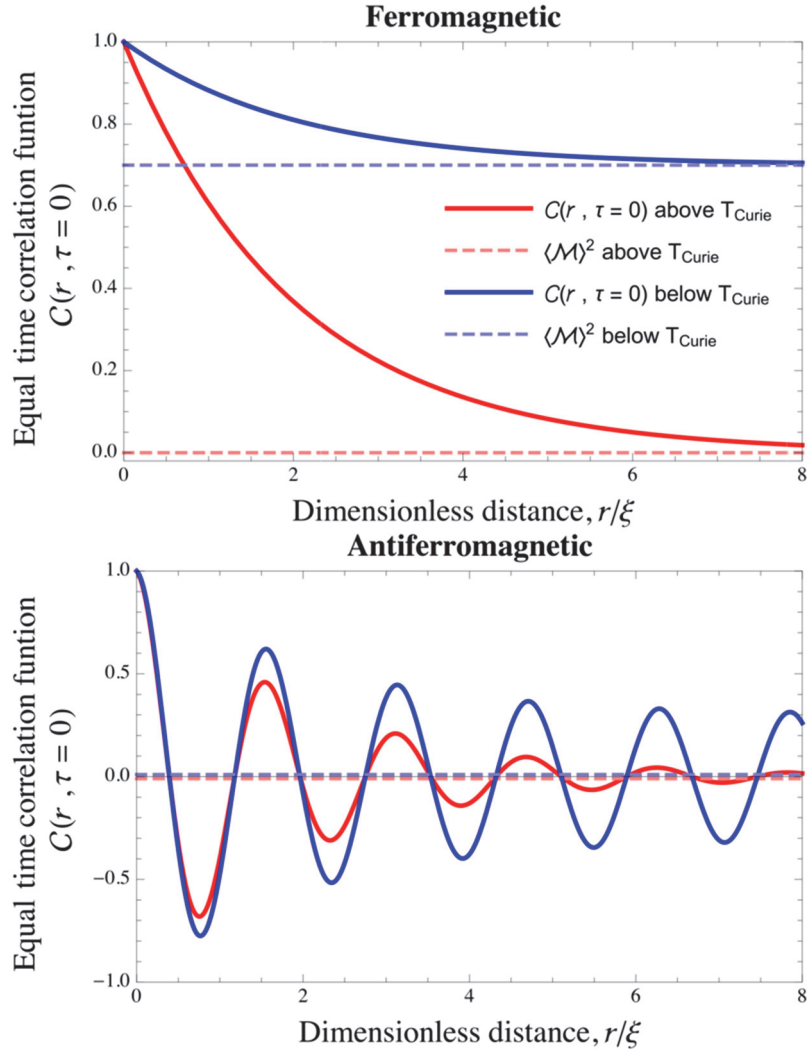

Figure 6.8: An equal time spin-spin correlation function of the ferromagnetic and antiferromagnetic sample.

Above T_{Curie}, the functions decay exponentially to zero. On the other hand, the functions decay to non-zero below T_{Curie}.

6.5. Autocorrelation

To understand the non-locality of the $\mathbf{q_1}$* modulation and check whether it has a long-range order, I performed an autocorrelation (AC) analysis to my data. The AC method is useful for visualization of the periodicity and the correlation between repeating structures. Since one of the strengths of the STM is its direct measurement of spectral modulations, AC is suitable to analyze the STM data.

6.5.1. Structure factor

In scattering experiments using neutrons or *X*-rays, the measured physical quantity is the structure factor S($\mathbf{q}$, ω), which is the FT of the density-density correlation function. S($\mathbf{q}$, ω) becomes strong when there is a correlation over a sizable length scale[67], which makes scattering experiments a powerful tool for characterizing non-local orders. S($\mathbf{q}$, ω) is given by

$$S(\boldsymbol{q},\omega) = \frac{1}{N}\sum_{ll'} e^{i\boldsymbol{q}\cdot\left(\boldsymbol{R}^l-\boldsymbol{R}^{l'}\right)} \int \frac{dt}{2\pi} e^{i\omega t} \langle e^{-i\boldsymbol{q}\cdot\boldsymbol{u}^{l'}} e^{i\boldsymbol{q}\cdot\boldsymbol{u}^{l'}(t)}\rangle$$

$$= \frac{1}{N}\int d\boldsymbol{r}d\boldsymbol{r}'\frac{dt}{2\pi} e^{i\boldsymbol{q}\cdot(\boldsymbol{r}-\boldsymbol{r}')} e^{i\omega t} \sum_{ll'} \langle \delta(\boldsymbol{r}-\boldsymbol{R}^l-\boldsymbol{u}^l)\delta\left(\boldsymbol{r}'-\boldsymbol{R}^{l'} - \boldsymbol{u}^{l'}(t)\right)\rangle \quad \ldots (6.5.1)$$

where $\boldsymbol{u}$ is the displacement vector from each ion's equilibrium position $\boldsymbol{R}$, and $\mathbf{q}$ is the difference between the momentum $\boldsymbol{k}$ of the incoming and the outgoing particles of the scattering. This formula for the structure factor can be applied to my STM measurements as well because the structure factor can be obtained from

the FT of the density-density correlation function.

6.5.2. Two different ways of calculating AC

There are two approaches to computational AC calculation. The first is the direct calculation AC in real space (ACR), and the other is AC obtained using FT (ACF). Since the spatial dimension of my SI-STM data is two, I did the two-dimensional spatial AC to my differential conductance data of $Bi_2Sr_2CaCu_2O_{8+\delta}$ above T_c. The equation of two dimensional ACR is given by

$$ACR\big(f(r)\big) = \int_0^{L_x}\int_0^{L_y} dxdyf(x_1+x, y_1, +y)f(x_1, y_1) \times \frac{1}{(L_x - x)\times\big(L_y - y\big)} \quad \ldots \quad (6.5.2)$$

where $L_{x(y)}$ is the length of one side of the data, and the last term is for the normalization. Next, the equation of ACF comes from the Wiener-Khinchin theorem[98,99]. The derivation of this theorem is as follows. A definition of AC is given by

$$ACF(f(r)) = \int_{-\infty}^{\infty} \bar{f}(t)f(r+t)dt \quad \ldots \quad (6.5.3)$$

and the FT of $f(r)$ and its complex conjugate are written by

$$f(r) = \int_{-\infty}^{\infty} f(q)e^{-2\pi irq}dr \quad \ldots \quad (6.5.4)$$

$$\bar{f}(r) = \int_{-\infty}^{\infty} \bar{f}(q)e^{2\pi irq}dr \quad \ldots \quad (6.5.5)$$

Substituting these to AC function then I can obtain

$$ACF(f(r)) = \int_{-\infty}^{\infty} \bar{f}(t)f(t+r)dt$$

$$= \int_{-\infty}^{\infty} \left[\int_{-\infty}^{\infty} \bar{f}(q)e^{2\pi iqt}dq\right]\left[\int_{-\infty}^{\infty} f(q')e^{-2\pi iq'(t+r)}dq'\right]dt$$

$$= \int_{-\infty}^{\infty}\int_{-\infty}^{\infty}\int_{-\infty}^{\infty} \bar{f}(q)e^{2\pi iqt}f(q')e^{-2\pi iq'(t+r)}dq\,dq'\,dt$$

$$= \int_{-\infty}^{\infty}\int_{-\infty}^{\infty} \bar{f}(q)\,f(q')e^{-2\pi it(q'-q)t}e^{-2\pi iq'r}dqdq'dt$$

$$= \int_{-\infty}^{\infty}\int_{-\infty}^{\infty} \bar{f}(q)\,f(q')\delta(q'-q)e^{-2\pi iq'r}dqdq'$$

$$= \int_{-\infty}^{\infty} \bar{f}(q)f(q)e^{-2\pi iqr}dq$$

$$= \int_{-\infty}^{\infty} |f(q)|^2 e^{-2\pi iqr}dq$$

$$= F[|f(q)|^2](r) \quad \dots \quad (6.5.6)$$

AC of $f(r)$ can be calculated by FT of the absolute square of $f(q)$, which is the inverse FT of $f(t)$.

In the case of ACR, as the overlapping area decreases, the calculation error increases with inverse proportional to the overlapping area (Fig. 6.9). Besides, when calculating a two-dimensional data with $N \times N$ pixels, ACR requires computational time on the order of N^2, but ACF requires time on the order of $N\log N$[100]. For these reasons, I used the ACF method. As shown in Fig. 6.10, the results of both calculations do not seem to be significant. Both figures show the non-vanishing checkerboard patterns over the entire FOV. Figure. 6.10a-f show AC images from 24 mV to -36 mV and Fig. 6.10g-l are their FTs. As the energy decreases, the DOSM becomes blurry, and $|\mathbf{q_1}^*|$ (red circle in Fig 6.10) decreases.

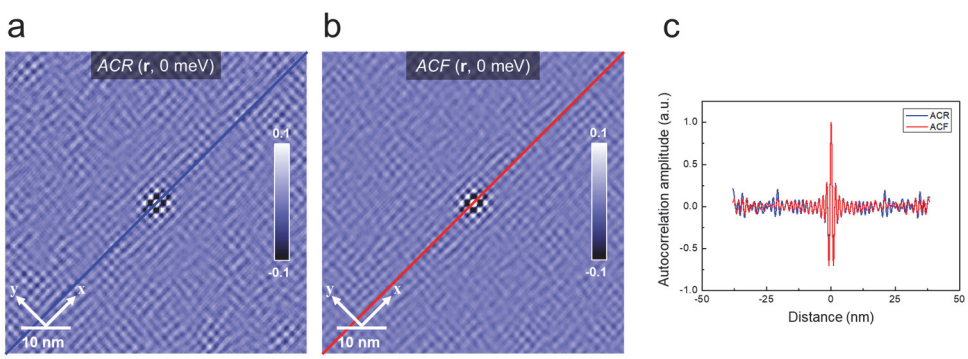

Figure 6.9: Different ways of calculating AC

(a) AC result of a real space calculation, (b) AC result using the FT. Both results show similar non-vanishing patterns. (c) Diagonal line cuts of (a) and (b). Line-cut of ACR varies more by the distance.

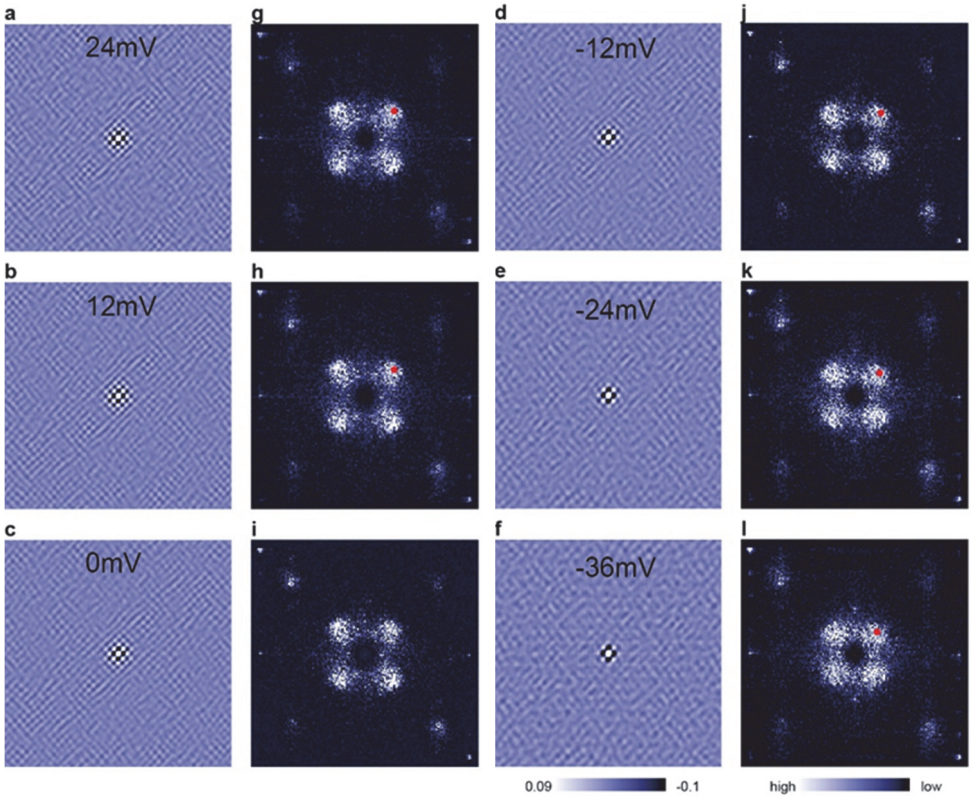

Figure 6.10: AC images of the HUD $Bi_2Sr_2CaCu_2O_{8+\delta}$.

(a)-(f) AC images of the HUD $Bi_2Sr_2CaCu_2O_{8+\delta}$ from 24 mV to -36 mV. The modulation pattern diminishes as energy decreases. (g)-(l) 2DFT images of (a)-(f) These images are directly related to the structure factor S(**q**, ω). Red dots represent the peak locations from the Lorentzian fitting to the $\mathbf{q}_1$*.

6.6. AC result

To obtain the S(**q**, ω) from my SI-STM data, I applied the AC technique to my data. A conventional way to deduce a length scale from an ordered state is to fit

the correlation function to an exponential function or its variant[101]. In Fig. 6.11a and b, a two-dimensional AC image of $\mathbf{q_1}$* modulations of $Bi_2Sr_2CaCu_2O_{8+\delta}$ and its 2DFT in the PG phase are shown, respectively. In Fig. 6.11e and f, a two-dimensional AC image of standard QPI patterns and its 2DFT of the $Sr_3(Ru_{1-x}Ti_x)_2O_7$ are shown, respectively. It is clear that the AC analysis can indeed successfully discern the local interference in the case of the $Sr_3(Ru_{1-x}Ti_x)_2O_7$ (Fig. 6.11) from the global pattern (Fig. 6.11a) by noting that in $Bi_2Sr_2CaCu_2O_{8+\delta}$, the $\mathbf{q_1}$* modulation pattern continues to exist up to the edge of the AC image (Fig. 6.11c) while in the $Sr_3(Ru_{1-x}Ti_x)_2O_7$, a few ripples appear only around the origin (Fig. 6.11g). To determine the correlation length scale of the $\mathbf{q_1}$* modulation, I tried a conventional fitting from the line-cut of the two-dimensional AC results to an exponential, a power-law and a power-law multiplied by an exponential function, none of which were successful due to a non-vanishing tail part (Fig. 6.11d) that reached approximately 400 Å. It is very likely that this non-vanishing tail would continue to more than a few thousand Å if I had data with a larger FOV. Therefore, I used a different approach to do fitting in the PG $Bi_2Sr_2CaCu_2O_{8+\delta}$.

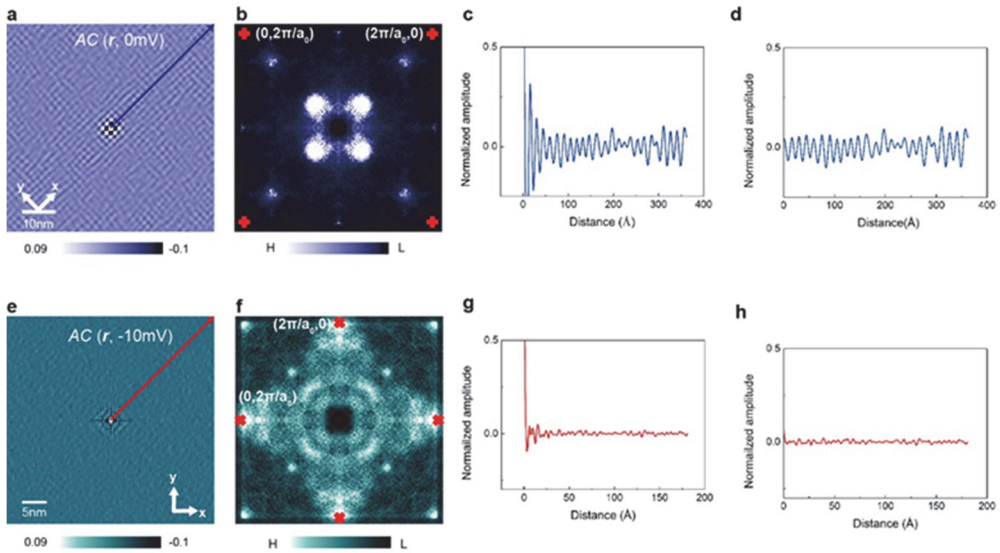

Figure 6.11: Normalized AC images of a *g*(*r*, *V*) of the HUD $Bi_2Sr_2CaCu_2O_{8+\delta}$ and $Sr_3(Ru_{1-x}Ti_x)_2O_7$ and q space images.

(a) A normalized AC image of *g*(**r**, 0 mV) of the HUD $Bi_2Sr_2CaCu_2O_{8+\delta}$, where the amplitude of the center peak has a value of 1. Before doing AC, Gaussian subtraction was performed to show the DOSM more clearly. There are also modulations to *x* and *y* directions in the entire FOV. Without several peaks near the center, there are $\mathbf{q_1}$* modulations in the entire FOV with magnitudes of approximately 5% of the center peak magnitude. (b) The FT of (a). It can be directly compared with scattering instrument results. All **q** space analysis has been done using the FT of the AC image, not that of the original images. (c) The AC line-cut to the *x* direction of the HUD $Bi_2Sr_2CaCu_2O_{8+\delta}$ at 0 mV bias (blue line in (a)). From the center to 60 Å, it decreases exponentially. However, from this point (approximately 60 Å from the center), the amplitude of the modulation appears to be constant. There are non-zero periodic fluctuations in the tail region, and it cannot be fitted in a conventional way. (d) The non-vanishing part of (c). Line-cut in (c) can be written as the sum of an exponential decay function and a constant function multiplied by a sinusoidal function: $(\boldsymbol{C_1 e^{-ax} + C_2})\boldsymbol{e^{iq_0 x}}$. The line-cut in (c) divided by the envelope fitting of (c) gives the sinusoidal function and multiplication of the constant function. (e) Normalized AC image of *g*(**r**, -10 mV) of the $Sr_3(Ru_{1-x}Ti_x)_2O_7$.

Unlike (a), there is no modulation but instead a few ripples with a center peak. It shows the power of AC to distinguish local and global patterns. (f) The FT of (b). I cannot compare the correlation length obtained from **q** space with that obtained in real space. (g) The AC line-cut to the diagonal direction of the $Sr_3(Ru_{1-x}Ti_x)_2O_7$ at -10 mV bias (red line in (b)). Only a center peak is presented with no exponential decay or periodic modulation. Moreover, the amplitude of the line-cut is much smaller than that of $Bi_2Sr_2CaCu_2O_{8+\delta}$. (h) Using the same procedure as in (d), (h) is extracted from (g). In (h), the modulation is barely seen, unlike in (d), and magnitudes of modulations in (h) are approximately 1/10 of that in (d).

6.7. AC data fitting

I assume that there is an aforementioned long-range order, relevant to the $\mathbf{q_1}$* modulation of the PG $Bi_2Sr_2CaCu_2O_{8+\delta}$. Thus, I set a fitting equation as follows

$$f(x) = \left(C_1 e^{-\frac{x}{\xi}} + C_2\right) e^{iq_0 x} \quad \ldots \quad (6.7.1)$$

where ξ is a conventional correlation length of DOSM, and C_2 is a constant value for non-vanishing tail parts. Using this equation, I tried to fit the line-cut from the AC profile along the Cu-O-Cu bonding direction. ξ is related to the center around $\mathbf{q_1}$* peaks and has a length scale of approximately 15 Å, while C_2 is related to the tail part and has a long-range order (Fig. 6.11). While the ξ value matches very well with the correlation length estimated from the half-width at half maximum (HWHM) of the $\mathbf{q_1}$* peak (Fig. 6.12), C_2 cannot be deduced

from the FT analysis alone. According to the usual definition of *coherence*, such a long-range order strongly supports the emergence of *coherence* among the quasiparticles in the PG phase.

6.7.1. Correlation length: real space vs. **q** space

To obtain a correlation length ξ directly in real space and compare them with the result obtained in **q** space, I used an exponential function as a fitting function. First, I performed the FT to an exponential function.

(2

$$\mathcal{F}_x[e^{-ax}] = \int_{-\infty}^{\infty} e^{-ax}e^{-iqx}dx = \frac{2a}{a^2+q^2} \quad \ldots \quad (6.7.2)$$

There is the DOSM in real space AC image, and the fitting function of AC line-cut of DOSM is written as

$$C_1 e^{-ax}e^{iq_0x} \quad \ldots \quad (6.7.3)$$

where q_0 = the periodicity of the modulation or the amplitude of $\mathbf{q_1}^*$ vector in **q** space. The FT of the AC function in **q** space is

$$\mathcal{F}_x\left[e^{-ax}e^{-iq_0x}\right] = \frac{2a}{(q-q_0)^2+a^2} \quad \ldots \quad (6.7.4)$$

Using this formula and the exponential fitting of AC, I can compare the correlation length of real space and **q** space directly. The correlation length of

DOSM in real space is $1/a$ and that of **q** space is HWHM with the unit of $2\pi/a_0$ of the Lorentzian function with a peak at q_0. Figure 6.12a and b show the correlation length ξ from the exponential fitting in real space and the Lorentzian fitting in **q** space. Both results are well matched, and the figure shows the correlation length ξ plotted versus V. Within the error bar, ξ becomes larger around the Fermi level and follows $\xi \propto -|V - V_F|^{\alpha_1}$ where α_1 is approximately two

Since $Sr_3(Ru_{1-x}Ti_x)_2O_7$ has a local random impurities pattern, it does not have the e^{iq_0x} term. Therefore, in this case, the correlation length from an exponential fitting in real space cannot be matched with a **q** space peak width. The information of the real space correlation length of impurities hides in the center peak in **q** space. Therefore, I cannot obtain a correlation length from the real space fitting directly. In this case, **q** space analysis is the only way to obtain the correlation length of the local impurity patterns. AC is not a suitable method to compare the local patterns of the real and **q** space data.

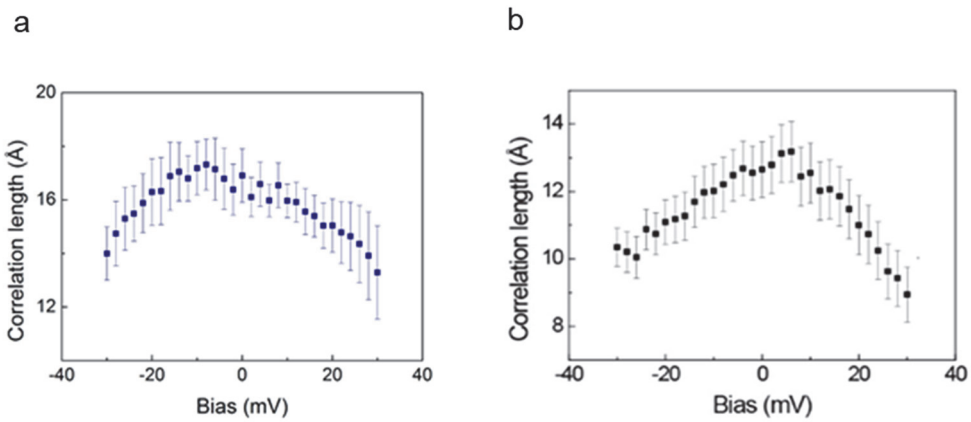

Figure 6.12: The correlation lengths in real and q space.

(a) The correlation length, ξ obtained from the real space fitting versus bias. Fitting performed from the center peaks to the fourth peaks (before the amplitude becomes constant). (b) The correlation length obtained from HWHM of $\mathbf{q}_1$* peaks in **q** space. Both results are parabolic graphs dependent on the bias with the maximum near the Fermi energy.

6.7.2. Semi long-range order

Next, the tail part, related to, C_2 also has an additional phase term, is given by

$$C_2 e^{-i(\boldsymbol{q}_0+\boldsymbol{q}_\varphi)x} \quad \ldots \quad (6.7.5)$$

In the same way, a correlation length corresponding to the tail part is related to the HWHM of the **q** space peak at $\mathbf{q} = \mathbf{q}_0 + \mathbf{q}_\varphi$. However, the amplitude of the tail part is much smaller than that of ξ. This makes it impossible to find a suitable peak of the tail part in **q** space. Therefore, real space analysis in the sole

approach for analyzing the non-vanishing tails. However, in this case, I cannot obtain the length scale directly because the amplitude of the tail part hardly decreases until 400 Å, and it increases again even further from the center (Fig. 6.11c). Therefore, I expect that the length scale of DOSM is a considerable value that is more than just a few nanometers. Although the FOV of my data is not sufficiently large to verify this hypothesis, these modulations may reach at least hundreds of nanometers.

Since I could not obtain a length scale of the non-vanishing tail part due to this part far away over than my FOV size, I plotted the average amplitude of C_2 vs energy E. The average amplitude of C_2 also becomes larger around the Fermi level and follows, $C_2 \propto -|E - E_F|^{\alpha}$, where α is also approximately two .

From the AC analysis in real space and the HWHM analysis in **q** space, it is clear that the PG $Bi_2Sr_2CaCu_2O_{8+\delta}$ has a very unconventional length scale that cannot be fit into a conventional correlation model.

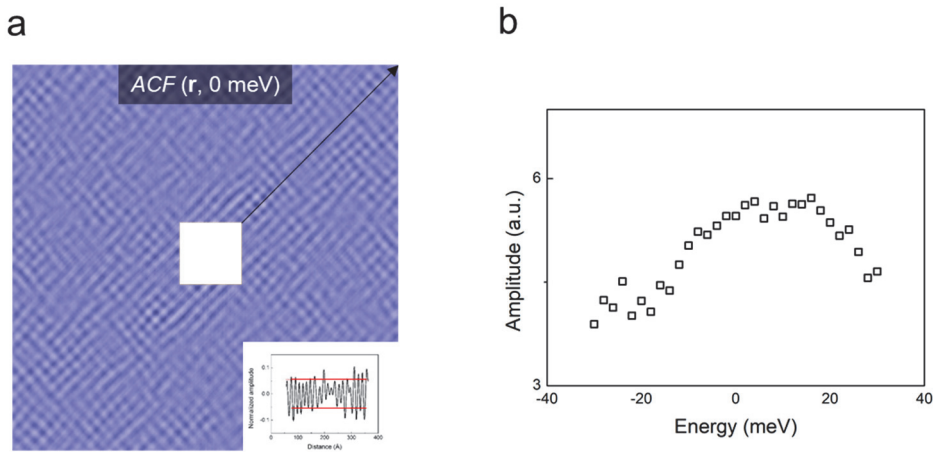

Figure 6.13: The intensity of DOSM as a function of the energy.

(a) The differential conductance, $g(\mathbf{r}, 0\ \text{meV})$ image, which center peaks are removed from the original image. To find the energy dependence of DOSM, I did line-cut to the x direction (black arrow in a). Line-cut data and its average intensity (red line) are shown. (a, inset) (b) The energy dependence of the average intensity of DOSM. The results show a parabolic dependence on energy with the maximum near the Fermi energy.

6.8. Summary

In this chapter, I showed the DOSM of the HUD $Bi_2Sr_2CaCu_2O_8$ above T_c. The DOSM above T_c has a global characteristic of all FOV of about four-unit cell periodicity. I described the unique properties of DOSM in the PG phase, not the reported CDW on underdoped cuprates. The properties of DOSM are dispersions in real space, semi long-range order and resiliency to disturbances. For comparison, I presented an SI-STM study of a non-superconducting perovskite oxide, $Sr_3(Ru_{1-x}Ti_x)_2O_7$, to show that the DOSM in the PG is distinguished from a usual QPI by a pronounced spatial correlation. My observations suggest that

the DOSM in the PG is a manifestation of a novel electronic coherent state of matter.

Chapter 7.

Conclusion

In this thesis, I have talked about the magnetic field and above T_c studies of the cuprate superconductor $Bi_2Sr_2CaCu_2O_{8+\delta}$ using SI-STM. I found a similar DOSM, which are four-unit cell periodicity and a particle-hole asymmetry, in two different experiments. The characteristic vector of DOSM with approximately 0.25 $2\pi/a_0$ in this thesis appears to be ubiquitous in $Bi_2Sr_2CaCu_2O_{8+\delta}$. – not only vortex and above T_c studies using SI-STM, but also the study of REXS[62,102], and SJTM[96], and it can even be obtained from the d^2I/dV^2 measurements[103]. I analyzed the DOSM by various analysis methods - FT, masking and AC.

In chapter 4, I analyze the characteristics of DOSM observed in magnetic field experiments, and in chapter 5, I build a model of the QO in real space using the results of magnetic field experiments. In chapter 6, I introduce the characteristics and correlation analysis of DOSM above T_c.

In the magnetic field experiments, I discovered a *particle-hole* asymmetric dispersion of DOSM inside the superconducting vortices on an SUD $Bi_2Sr_2CaCu_2O_{8+\delta}$, and the dispersion was electron-like, unlike a conventional CDW. On the HUD $Bi_2Sr_2CaCu_2O_{8+\delta}$, I could not find any sign of vortices up to 13 T, but I found a globally expanded DOSM displaying the same particle-hole asymmetric, electron-like dispersion as the patterns inside the vortices in the SUD $Bi_2Sr_2CaCu_2O_{8+\delta}$. Due to the lack of direct spectroscopic evidence of small electron-like pockets on hole underdoped cuprates and based on my observations, I proposed an alternative model of QO results on hole underdoped cuprates in a simple picture of the commensurate resonance between the possible quasiparticle orbit due to the magnetic field and DOSM, which does not require a Fermi surface reconstruction nor a closed Fermi surface as proposed previously. My result implies that the dispersive DOSM can impose a significant impact on magneto-transport properties as well as spectroscopic features.

In the above T_c experiment, DOSM has unique properties that have not yet been observed in any other matter. Here, I observed purely electronic spatial incommensurate modulations in DOS with a semi long-range order, the periodicity of which changes according to the energy, suppressing the underlying crystalline structures and disorders. I tried to find what this modulation is to compare to previous SI-STM results of a usual QPI. First, a simple picture of the QPI due to impurities as in the octet QPI below T_c cannot be applied because the $\mathbf{q_1}$* modulation has semi long-range order. Second, a conventional CDW model cannot explain the DOSM I observed either, especially considering the dispersiveness and the appearance of the patterns in the positive bias. From my analysis, I can only conclude that in the PG phase of $Bi_2Sr_2CaCu_2O_{8+\delta}$, some form of a strong coherence emerges in the LDOS (not charges).

Bibliography

[1] Binnig G and Rohrer H 1982 Scanning tunnelling microscopy *Surf. Sci.* **126** 236–44

[2] Giaever I 1960 Energy Gap in Superconductors Measured by Electron Tunneling *Phys. Rev. Lett.* **5** 147–8

[3] Tersoff J and Hamann D R 1983 Theory and Application for the Scanning Tunneling Microscope *Phys. Rev. Lett.* **50** 1998–2001

[4] Chen C J 2007 *Introduction to Scanning Tunneling Microscopy* (Oxford University Press)

[5] Fang A, Ru N, Fisher I R and Kapitulnik A 2007 STM Studies of TbTe3: Evidence for a Fully Incommensurate Charge Density Wave *Phys. Rev. Lett.* **99** 6–9

[6] Arguello C J, Chockalingam S P, Rosenthal E P, Zhao L, Gutiérrez C, Kang J H, Chung W C, Fernandes R M, Jia S, Millis A J, Cava R J and Pasupathy A N 2014 Visualizing the charge density wave transition in 2H - NbSe2 in real space *Phys. Rev. B - Condens. Matter Mater. Phys.* **89** 1–9

[7] Hoffman J E, McElroy K, Lee D-H H, Lang K M, Eisaki H, Uchida S and Davis J C 2002 Imaging Quasiparticle Interference in Bi2Sr2CaCu2O8+δ *Science (80-.).* **297** 1148 LP – 1151

[8] McElroy K, Simmonds R W, Hoffman J E, Lee D-H H, Orenstein J, Eisaki H, Uchida S and Davis J C 2003 Relating atomic-scale electronic phenomena to wave-like quasiparticle states in superconducting Bi2Sr2CaCu2O8+δ *Nature* **422** 592–6

[9] Hanaguri T, Kohsaka Y, Davis J C, Lupien C, Yamada I, Azuma M, Takano M, Ohishi K, Ono M and Takagi H 2007 Quasiparticle interference and superconducting gap in Ca 2-x Na x CuO 2 Cl 2 *Nat. Phys.* **3** 865–71

[10] Pan S H, Hudson E W, Lang K M, Eisaki H, Uchida S and Davis J C 2000 Imaging the effects of individual zinc impurity atoms on superconductivity in Bi2Sr2CaCu2O8+δ *Nature* **403** 746–50

[11] Hudson E W, Lang K M, Madhavan V, Pan S H, Eisaki H, Uchida S and Davis J C 2001 Interplay of magnetism and high-Tc superconductivity at individual Ni impurity atoms in Bi2Sr2CaCu2O8+δ *Nature* **411** 920–4

[12] Renner C, Revaz B, Kadowaki K, Maggio-Aprile I and Fischer Ø 1998 Observation of the Low Temperature Pseudogap in the Vortex Cores of Bi2Sr2CaCu2O8+δ *Phys. Rev. Lett.* **80** 3606–9

[13] Pan S H, Hudson E W, Gupta A K, Ng K-W, Eisaki H, Uchida S and Davis J C 2000 STM Studies of the Electronic Structure of of vortex cores in Bi_2 Sr_2 Ca Cu_2 O_8+delta *Phys. Rev. Lett.* **85**

[14] Hoffman J E, Hudson E W, Lang K M, Madhavan V, Eisaki H, Uchida S and Davis J C 2002 A four unit cell periodic pattern of quasi-particle states surrounding vortex cores in Bi2Sr2CaCu2O8+?? *Science (80-.).* **295** 466–9

[15] McElroy K, Lee J, Slezak J A, Lee D-H, Eisaki H, Uchida S and Davis J C 2005 Atomic-Scale Sources and Mechanism of Nanoscale Electronic Disorder in Bi_2Sr_2CaCu_2O_8+δ *Science (80-.).* **309** 1048 LP – 1052

[16] Zeljkovic I, Xu Z, Wen J, Gu G, Markiewicz R S and Hoffman J E 2012 Imaging the Impact of Single Oxygen Atoms on Superconducting Bi_{2+y}Sr_{2–y}CaCu₂O_{8+x} *Science (80-.).* **337** 320 LP – 323

[17] Mcelroy K, Lee D H, Hoffman J E, Lang K M, Lee J, Hudson E W, Eisaki H, Uchida S and Davis J C 2005 Coincidence of checkerboard charge order and antinodal state decoherence in strongly underdoped superconducting Bi2Sr2CaCu2O8+δ *Phys. Rev. Lett.* **94** 1–4

[18] Pan S H, Hudson E W and Davis J C 1999 3He refrigerator based very low temperature scanning tunneling microscope *Rev. Sci. Instrum.* **70** 1459–63

[19] Kim J-J J, Joo S H, Lee K S, Yoo J H, Park M S, Kwak J S and Lee J 2017 Improved design for a low temperature scanning tunneling microscope with an *in situ* tip treatment stage *Rev. Sci. Instrum.* **88** 043702

[20] Onnes H K 1911 The Superconductivity of Mercury *Comm. Phys. Lab. Univ., Leiden* 122b, 122b, 124c

[21] Gavaler J R 1973 Superconductivity in Nb–Ge films above 22 K *Appl. Phys. Lett.* **23** 480–2

[22] Bednorz J G and Miiller K A 1986 Possible High T c Superconductivity in the Ba - La- Cu- 0 System *Zeitschrift f˙ur Phys. B Condens. Matter 64* 189–93

[23] Ashburn J R, Wu M K and Torng C J 1987 Superconductivity at 93K in a new mixed-phase Y-Ba-Cu-O compound system *Phys. Rev. Lett.* **58** 908–10

[24] Gao L, Xue Y Y, Chen F, Xiong Q, Meng R L, Ramirez D and Chu C W 1994 Superconductivity up to 164 K in HgBaCaO under quasihydrostatic pressures *Phys. Rev. B* **50** 4260–3

[25] Monteverde M, Acha C, Núñez-Regueiro M, Pavlov D A, Lokshin K A, Putilin S N and Antipov E V 2005 High-pressure effects in fluorinated HgBa2Ca2Cu3O8 + δ *Europhys. Lett.* **72** 458–64

[26] Kamihara Y, Watanabe T, Hirano M and Hosono H 2008 Iron-Based Layered Superconductor La[O1-xFx]FeAs (x = 0.05−0.12) with Tc = 26 K *J. Am. Chem. Soc.* **130** 3296–7

[27] Rotter M, Tegel M and Johrendt D 2008 Superconductivity at 38 K in the iron arsenide (Ba1-xKx)Fe2As2 *Phys. Rev. Lett.* **101** 4–7

[28] Paglione J and Greene R L 2010 High-temperature superconductivity in iron-based materials *Nat. Phys.* **6** 645–58

[29] Ge J-F, Liu Z-L, Liu C, Gao C-L, Qian D, Xue Q-K, Liu Y and Jia J-F 2015 Superconductivity above 100 K in single-layer FeSe films on doped SrTiO3 *Nat. Mater.* **14** 285–9

[30] Cao Y, Fatemi V, Fang S, Watanabe K, Taniguchi T, Kaxiras E and

Jarillo-Herrero P 2018 Unconventional superconductivity in magic-angle graphene superlattices *Nature* **556** 43–50

[31] Drozdov A P, Eremets M I, Troyan I A, Ksenofontov V and Shylin S I 2015 Conventional superconductivity at 203 kelvin at high pressures in the sulfur hydride system *Nature* **525** 73–6

[32] Drozdov A P, Kong P P, Minkov V S, Besedin S P, Kuzovnikov M A, Mozaffari S, Balicas L, Balakirev F F, Graf D E, Prakapenka V B, Greenberg E, Knyazev D A, Tkacz M and Eremets M I 2019 Superconductivity at 250 K in lanthanum hydride under high pressures *Nature* **569** 528–31

[33] Sheng Z Z and Hermann A M 1988 Bulk superconductivity at 120 K in the Tl–Ca/Ba–Cu–O system *Nature* **332** 138–9

[34] Maeda H, Tanaka Y, Fukutomi M and Asano T 1988 A New High-TcOxide Superconductor without a Rare Earth Element *Jpn. J. Appl. Phys.* **27** L209–10

[35] Maeda H, Tanaka Y, Fukutomi M and Asano T 1988 A New High-TcOxide Superconductor without a Rare Earth Element *Jpn. J. Appl. Phys.* **27** L209–10

[36] Kinoda G, Hasegawa T, Nakao S, Hanaguri T, Kitazawa K, Shimizu K, Shimoyama J and Kishio K 2003 Observations of electronic inhomogeneity in heavily Pb-doped Bi_2 Sr_2 Ca Cu_2 O_y single crystals by scanning tunneling microscopy *Phys. Rev. B* **67** 224509

[37] Kirk M D, Nogami J, Baski A A, Mitzi D B, Kapitulnik A, Geballe T H

and Quate C F 1988 The Origin of the Superstructure in Bi_2 Sr_2 Ca Cu_2 O_8+δ as Revealed by Scanning Tunneling Microscopy *Science (80-.).* **242** 1673 LP – 1675

[38] Inoue A, Mukaida H, Nakao M and Yoshizaki R 1994 Study on the cleaved surface structure of Bi2Sr2CaCu2O8+δ by scanning tunneling microscopy *Phys. C Supercond.* **233** 49–54

[39] Zandbergen H W, Groen W A, Mijlhoff F C, van Tendeloo G and Amelinckx S 1988 Models for the modulation in A2B2CanCu1+nO6+2n, A, B=Bi, Sr OR Tl, Ba and n=0, 1, 2 *Phys. C Supercond.* **156** 325–54

[40] Gladyshevskii R, Musolino N and Flükiger R 2004 Structural origin of the low superconducting anisotropy of Bi_1.7 Pb_0.4 Sr_2 Ca_0.9 Cu_2 O_8 crystals *Phys. Rev. B* **70** 184522

[41] Slezak J A, Lee J, Wang M, McElroy K, Fujita K, Andersen B M, Hirschfeld P J, Eisaki H, Uchida S and Davis J C 2008 Imaging the impact on cuprate superconductivity of varying the interatomic distances within individual crystal unit cells *Proc. Natl. Acad. Sci.* **105** 3203–8

[42] Meissner W and Ochsenfeld R 1933 Ein neuer Effekt bei Eintritt der Supraleitf□higkeit *Naturwissenschaften* **21** 787–8

[43] Abrikosov A A 1957 The magnetic properties of superconducting alloys *J. Phys. Chem. Solids* **2** 199–208

[44] Tinkham M 2004 *Introduction to Superconductivity* (Mineola, New York: Dover Publications)

[45] Welp U, Kwok W K, Crabtree G W, Vandervoort K G and Liu J Z 1989

Magnetic measurements of the upper critical field of YBa2Cu3O7- delta single crystals *Phys. Rev. Lett.* **62** 1908–11

[46] Hao Z, Clem J R, McElfresh M W, Civale L, Malozemoff A P and Holtzberg F 1991 Model for the reversible magnetization of high-κ type-II superconductors: Application to high-Tc superconductors *Phys. Rev. B* **43** 2844–52

[47] Li Q, Suenaga M, Hikata T and Sato K 1992 Two-dimensional fluctuations in the magnetization of Bi2Sr2Ca2Cu3O10 *Phys. Rev. B* **46** 5857–60

[48] Brandstätter G, Sauerzopf F M, Weber H W, Ladenberger F and Schwarzmann E 1994 Upper critical field, penetration depth, and GL parameter of Tl-2223 single crystals *Phys. C Supercond.* **235**–**240** 1845–6

[49] Prozorov R and Giannetta R W 2006 Magnetic penetration depth in unconventional superconductors *Supercond. Sci. Technol.* **19** R41–67

[50] Wells F S, Pan A V, Wang X R, Fedoseev S A and Hilgenkamp H 2015 Analysis of low-field isotropic vortex glass containing vortex groups in YBa2Cu3O7−x thin films visualized by scanning SQUID microscopy *Sci. Rep.* **5** 8677

[51] Berthod C, Maggio-Aprile I, Bruér J, Erb A and Renner C 2017 Observation of Caroli–de Gennes–Matricon Vortex States in YBa2Cu3O7−δ *Phys. Rev. Lett.* **119** 237001

[52] Hess H F, Robinson R B, Dynes R C, Valles J M and Waszczak J V.

1989 Scanning-Tunneling-Microscope Observation of the Abrikosov Flux Lattice and the Density of States near and inside a Fluxoid *Phys. Rev. Lett.* **62** 214–6

[53] Caroli C, De Gennes P G and Matricon J 1964 Bound Fermion states on a vortex line in a type II superconductor *Phys. Lett.* **9** 307–9

[54] Machida T, Kohsaka Y, Matsuoka K, Iwaya K, Hanaguri T and Tamegai T 2016 Bipartite electronic superstructures in the vortex core of Bi2Sr2CaCu2O8+δ *Nat. Commun.* **7** 11747

[55] Edkins S D, Kostin A, Fujita K, Mackenzie A P, Eisaki H, Uchida S, Sachdev S, Lawler M J, Kim E-A, Séamus Davis J C and Hamidian M H 2019 Magnetic field–induced pair density wave state in the cuprate vortex halo *Science (80-.).* **364** 976–80

[56] Matsuba K, Yoshizawa S, Mochizuki Y, Mochiku T, Hirata K and Nishida N 2007 Anti-phase Modulation of Electron- and Hole-like States in Vortex Core of Bi 2 Sr 2 CaCu 2 O x Probed by Scanning Tunneling Spectroscopy *J. Phys. Soc. Japan* **76** 063704

[57] Yoshizawa S, Koseki T, Matsuba K, Mochiku T, Hirata K and Nishida N 2013 High-resolution scanning tunneling spectroscopy of vortex cores in inhomogeneous electronic states of Bi2Sr2CaCu 2Ox *J. Phys. Soc. Japan* **82** 1–5

[58] Wu T, Mayaffre H, Krämer S, Horvatić M, Berthier C, Kuhns P L, Reyes A P, Liang R, Hardy W N, Bonn D A and Julien M-H 2013 Emergence of charge order from the vortex state of a high-temperature superconductor *Nat. Commun.* **4** 2113

[59] Parker C V., Aynajian P, da Silva Neto E H, Pushp A, Ono S, Wen J, Xu Z, Gu G and Yazdani A 2010 Fluctuating stripes at the onset of the pseudogap in the high-Tc superconductor Bi2Sr2CaCu2O8+x *Nature* **468** 677–80

[60] Chang J, Blackburn E, Holmes A T, Christensen N B, Larsen J, Mesot J, Liang R, Bonn D A, Hardy W N, Watenphul A, Zimmermann M V., Forgan E M and Hayden S M 2012 Direct observation of competition between superconductivity and charge density wave order in YBa2Cu3O6.67 *Nat. Phys.* **8** 871–6

[61] Achkar A J, He F, Sutarto R, McMahon C, Zwiebler M, Hücker M, Gu G D, Liang R, Bonn D A, Hardy W N, Geck J and Hawthorn D G 2016 Orbital symmetry of charge-density-wave order in La1.875Ba0.125CuO4 and YBa2Cu3O6.67 *Nat. Mater.* **15** 616–20

[62] Comin R, Frano A, Yee M M, Yoshida Y, Eisaki H, Schierle E, Weschke E, Sutarto R, He F, Soumyanarayanan A, He Y, Le Tacon M, Elfimov I S, Hoffman J E, Sawatzky G A, Keimer B and Damascelli A 2014 Charge order driven by fermi-arc instability in Bi2Sr2-xlaxCuO6+δ *Science (80-.).* **343** 390–2

[63] Hanaguri T, Lupien C, Kohsaka Y, Lee D-H, Azuma M, Takano M, Takagi H and Davis J C 2004 A ‘checkerboard’ electronic crystal state in lightly hole-doped Ca2-xNaxCuO2Cl2 *Nature* **430** 1001–5

[64] Jang H, Lee W S, Nojiri H, Matsuzawa S, Yasumura H, Nie L, Maharaj A V., Gerber S, Liu Y J, Mehta A, Bonn D A, Liang R, Hardy W N, Burns C A, Islam Z, Song S, Hastings J, Devereaux T P, Shen Z X, Kivelson S

A, Kao C C, Zhu D and Lee J S 2016 Ideal charge-density-wave order in the high-field state of superconducting YBCO *Proc. Natl. Acad. Sci. U. S. A.* **113** 14645–50

[65] Doiron-Leyraud N, Proust C, LeBoeuf D, Levallois J, Bonnemaison J-B, Liang R, Bonn D A, Hardy W N and Taillefer L 2007 Quantum oscillations and the Fermi surface in an underdoped high-Tc superconductor *Nature* **447** 565–8

[66] LeBoeuf D, Doiron-Leyraud N, Levallois J, Daou R, Bonnemaison J-B, Hussey N E, Balicas L, Ramshaw B J, Liang R, Bonn D A, Hardy W N, Adachi S, Proust C and Taillefer L 2007 Electron pockets in the Fermi surface of hole-doped high-Tc superconductors *Nature* **450** 533–6

[67] Marder M P 2010 *Condensed Matter Physics* (Hoboken, NJ, USA: John Wiley & Sons, Inc.)

[68] Singleton J, De La Cruz C, McDonald R D, Li S, Altarawneh M, Goddard P, Franke I, Rickel D, Mielke C H, Yao X and Dai P 2010 Magnetic quantum oscillations in YBa2Cu3O6.61 and YBa2Cu3O6.69 in fields of up to 85 T: Patching the hole in the roof of the superconducting dome *Phys. Rev. Lett.* **104** 5–8

[69] Barišić N, Badoux S, Chan M K, Dorow C, Tabis W, Vignolle B, Yu G, Béard J, Zhao X, Proust C and Greven M 2013 Universal quantum oscillations in the underdoped cuprate superconductors *Nat. Phys.* **9** 761–4

[70] Vignolle B, Carrington A, Cooper R A, French M M J, Mackenzie A P, Jaudet C, Vignolles D, Proust C and Hussey N E 2008 Quantum

oscillations in an overdoped high-Tc superconductor *Nature* **455** 952–5

[71] Breznay N P, Hayes I M, Ramshaw B J, McDonald R D, Krockenberger Y, Ikeda A, Irie H, Yamamoto H and Analytis J G 2016 Shubnikov-de Haas quantum oscillations reveal a reconstructed Fermi surface near optimal doping in a thin film of the cuprate superconductor Pr1.86Ce0.14CuO4±δ *Phys. Rev. B* **94** 104514

[72] Jaudet C, Levallois J, Audouard A, Vignolles D, Vignolle B, Liang R, Bonn D A, Hardy W N, Hussey N E, Taillefer L and Proust C 2009 Quantum oscillations in underdoped *Phys. B Condens. Matter* **404** 354–6

[73] Vignolle B, Vignolles D, Julien M-H H and Proust C 2013 From quantum oscillations to charge order in high-Tc copper oxides in high magnetic fields *Comptes Rendus Phys.* **14** 39–52

[74] Sebastian S E, Harrison N, Liang R, Bonn D A, Hardy W N, Mielke C H and Lonzarich G G 2012 Quantum Oscillations from Nodal Bilayer Magnetic Breakdown in the Underdoped High Temperature Superconductor ${\mathrm{YBa}}_{2}{\mathrm{Cu}}_{3}{\mathrm{O}}_{6+x}$ *Phys. Rev. Lett.* **108** 196403

[75] Audouard A, Jaudet C, Vignolles D, Liang R, Bonn D A, Hardy W N, Taillefer L and Proust C 2009 Multiple Quantum Oscillations in the de Haas--van Alphen Spectra of the Underdoped High-Temperature Superconductor ${\mathrm{YBa}}_{2}{\mathrm{Cu}}_{3}{\mathbf{O}}_{6.5}$ *Phys. Rev. Lett.* **103** 157003

[76] Ding H, Yokoya T, Campuzano J C, Takahashi T, Randeria M, Norman M R, Mochiku T, Kadowaki K and Giapintzakis J 1996 Spectroscopic evidence for a pseudogap in the normal state of underdoped high-Tc superconductors *Nature* **382** 51–4

[77] Loeser A G, Shen Z-X, Dessau D S, Marshall D S, Park C H, Fournier P and Kapitulnik A 1996 Excitation Gap in the Normal State of Underdoped Bi2Sr2CaCu2O8+delta *Science (80-.).* **273** 325–9

[78] Norman M R, Ding H, Randeria M, Campuzano J C, Yokoya T, Takeuchi T, Takahashi T, Mochiku T, Kadowaki K, Guptasarma P and Hinks D G 1998 Destruction of the Fermi surface in underdoped high-Tc superconductors *Nature* **392** 157–60

[79] Shen K M, Ronning F, Lu D H, Baumberger F, Ingle N J C, Lee W S, Meevasana W, Kohsaka Y, Azuma M, Takano M, Takagi H and Shen Z-X 2005 Nodal Quasiparticles and Antinodal Charge Ordering in Ca2-xNaxCuO2Cl2 *Science (80-.).* **307** 901–4

[80] Weiss D, Klitzing K V., Ploog K and Weimann G 1989 Magnetoresistance Oscillations in a Two-Dimensional Electron Gas Induced by a Submicrometer Periodic Potential *Europhys. Lett.* **8** 179–84

[81] Weiss D, Roukes M L, Menschig A, Grambow P, von Klitzing K and Weimann G 1991 Electron pinball and commensurate orbits in a periodic array of scatterers *Phys. Rev. Lett.* **66** 2790–3

[82] Beenakker C W J and van Houten H 1991 Quantum Transport in Semiconductor Nanostructures *Semiconductor Heterostructures and Nanostructures* vol 44, ed H Ehrenreich and D B T-S S P Turnbull

(Academic Press) pp 1–228

[83] Drienovsky M, Joachimsmeyer J, Sandner A, Liu M H, Taniguchi T, Watanabe K, Richter K, Weiss D and Eroms J 2018 Commensurability Oscillations in One-Dimensional Graphene Superlattices *Phys. Rev. Lett.* **121** 26806

[84] Sebastian S E and Proust C 2015 Quantum Oscillations in Hole-Doped Cuprates *Annu. Rev. Condens. Matter Phys.* **6** 411–30

[85] Haldane F D M 1988 Model for a Quantum Hall Effect without Landau Levels: Condensed-Matter Realization of the "Parity Anomaly" *Phys. Rev. Lett.* **61** 2015–8

[86] de Haas W Y and van Alphen P M 1930 The dependence of the susceptibility of diamagnetic metals upon the field *Proc. Acad. Sci. Amsterdam* **33** 1106–18

[87] Aharonov Y and Bohm D 1959 Significance of Electromagnetic Potentials in the Quantum Theory *Phys. Rev.* **115** 485–91

[88] Vignolle B, Vignolles D, Julien M H and Proust C 2013 From quantum oscillations to charge order in high-Tc copper oxides in high magnetic fields *Comptes Rendus Phys.* **14** 39–52

[89] Wang Q H and Lee D H 2003 Quasiparticle scattering interference in high-temperature superconductors *Phys. Rev. B - Condens. Matter Mater. Phys.* **67** 1–4

[90] Vershinin M, Misra S, Ono S, Abe Y, Ando Y and Yazdani A 2004 Local Ordering in the Pseudogap State of the High-TcSuperconductor

Bi2Sr2CaCu2O8+δ *Science (80-.).* **303** 1995–8

[91] Da Silva Neto E H, Aynajian P, Frano A, Comin R, Schierle E, Weschke E, Gyenis A, Wen J, Schneeloch J, Xu Z, Ono S, Gu G, Le Tacon M, Yazdani A, Eduardo H, Neto S, Aynajian P, Frano A, Comin R, Schierle E, Weschke E, Gyenis A, Wen J, Schneeloch J, Xu Z, Ono S, Gu G, Tacon M Le and Yazdani A 2014 Ubiquitous Interplay Between Charge Ordering and High-Temperature Superconductivity in Cuprates *Science (80-.).* **343** 393–6

[92] Chuang T, Allan M P, Lee J, Xie Y, Ni N, Bud S L, Boebinger G S, Canfield P C and Davis J C 2010 Nematic Electronic Structure in the "parent" state of the Iron-Based Superconductor Ca(Fe1–xCox)2As2 *Science (80-.).* **327** 181–5

[93] Lee J, Allan M P, Wang M A, Farrell J, Grigera S A, Baumberger F, Davis J C and Mackenzie A P 2009 Heavy d-electron quasiparticle interference and real-space electronic structure of Sr3Ru2O7 *Nat. Phys.* **5** 800–4

[94] Wise W D, Boyer M C, Chatterjee K, Kondo T, Takeuchi T, Ikuta H, Wang Y and Hudson E W 2008 Charge-density-wave origin of cuprate checkerboard visualized by scanning tunnelling microscopy *Nat. Phys.* **4** 696–9

[95] Gao S, Flicker F, Sankar R, Zhao H, Ren Z, Rachmilowitz B, Balachandar S, Chou F, Burch K S, Wang Z, van Wezel J and Zeljkovic I 2018 Atomic-scale strain manipulation of a charge density wave *Proc. Natl. Acad. Sci. U. S. A.* **115** 6986–90

[96] Hamidian M H, Edkins S D, Joo S H, Kostin A, Eisaki H, Uchida S, Lawler M J, Kim E A, Mackenzie A P, Fujita K, Lee J and Davis J C S 2016 Detection of a Cooper-pair density wave in Bi2Sr2CaCu2O8+x *Nature* **532** 343–7

[97] Sethna J P 2006 *Statistical Mechanics: Entropy, Order Parameters and Complexity* (oxford: Oxford University Press)

[98] Wiener N 1930 Generalized harmonic analysis *Acta Math.* **55** 117–258

[99] Khintchine A 1934 Korrelationstheorie der station□ren stochastischen Prozesse *Math. Ann.* **109** 604–15

[100] Cooley J W and Tukey J W 1965 An Algorithm for the Machine Calculation of Complex Fourier Series *Math. Comput.* **19** 297–301

[101] Goldenfeld N 1992 *Lectures On Phase Transitions And The Renormalization Group* (Boca Raton: CRC Press)

[102] Blanco-Canosa S, Frano A, Schierle E, Porras J, Loew T, Minola M, Bluschke M, Weschke E, Keimer B and Le Tacon M 2014 Resonant X-ray Scattering Study of Charge Density Wave Correlations in YBa2Cu3O6+x *Phys. Rev. B* **90** 54513

[103] Lee J, Fujita K, McElroy K, Slezak J A, Wang M, Aiura Y, Bando H, Ishikado M, Masui T, Zhu J-X, Balatsky A V, Eisaki H, Uchida S and Davis J C 2006 Interplay of electron–lattice interactions and superconductivity in Bi2Sr2CaCu2O8+δ *Nature* **442** 546–50

국문초록

1986년에 처음으로 발견 된 고온 초전도는, 발견 이후 응집 물질 물리의 매우 중요한 연구 주제였습니다. 고온 초전도의 원리를 이해할 수 있는 한 가지 방법은 초전도가 깨지는 곳을 연구하는 것입니다. 이 논문에서 저는 서로 다른 두 가지 조건으로 초전도가 깨지는 곳에서의 연구 결과를 이야기하려 합니다.

첫 번째는 초전도에 강한 자기장을 걸어 실험한 결과입니다. 저희는 두 가지 다른 도핑의 $Bi_2Sr_2CaCu_2O_{8+\delta}$에서 자기장을 변화해 가며 원자 단위의 해상도의 분광 이미징 주사 터널 현미경 (spectroscopic imaging scanning tunneling microscopy: SI-STM) 실험을 하였습니다. 약하게 저도핑 된 $Bi_2Sr_2CaCu_2O_{8+\delta}$의 초전도 소용돌이와 강하게 저도핑 된 $Bi_2Sr_2CaCu_2O_{8+\delta}$의 대부분의 영역에서 비슷한 상태 밀도 변조 (density of states modulation: DOSM)를 발견하였습니다. 저는 이 실험결과로부터, 양자 진동 (quantum oscillations)의 실제 공간의 모델을 DOSM 을 이용해 제안하고, 서로 다른 장비들 간의 실험 결과를 통합할 것입니다.

두 번째는 초전도 임계 온도 위에서 시행한 연구입니다. 강하게 저도핑 된 $Bi_2Sr_2CaCu_2O_{8+\delta}$를 유사갭 (pseudogap: PG) 상태에서 SI-STM을 이용하여 측정하였을 때, 나는 자기장 실험에서 관찰한 DOSM과 유사한 특징을 가지는 DOSM을 전체 측정 영역에서 발견하였습니다. 임계 온도 위의 DOSM은 CDW 및 QPI와는 다른 특징을 가지고 있었습니다.

주요단어: 고온 초전도체, 상태 밀도 변조, 유사갭, 자기장(within 6 words)

학번: 2012-20377

감사의 말

저의 박사 학위는 온전히 저의 노력으로 이루어진 것이 아닌 주변 많은 사람의 도움으로 이루어진 것입니다. 이 자리를 빌어 그 분들에게 감사의 인사를 드립니다.

먼저 이진호 교수님께 감사의 인사를 드립니다. 연구가 뭔지도 모르던 저에게 연구가 어떤 것인지 연구자의 삶이란 어떤 것인지를 가르쳐 주셨습니다. 또한, 제가 실수를 해도 주어진 일을 완벽하게 하지 못해도 언제나 침착하고 인내심 있게 저를 배려하며 존중하는 모습에서 많은 것을 느끼고 배울 수 있었습니다. 그 결과 제가 무사히 박사 졸업을 할 수 있었기 때문에 감사의 인사를 드립니다.

그 다음으로 저와 함께 많은 고생을 했던 연구실 사람들에게 감사의 인사를 하고 싶습니다. 처음 연구실에 들어와 생각지도 못한 공사로 같은 고생을 한 꼼꼼한 민석이 형과 STM 1 팀원으로 낮과 밤, 주일과 주말을 가리지 않고 동고동락하며, 셋업부터 결과가 나올 때까지 같이 고생 한 재준이와 상현이에게 매우 고맙습니다. 혼자라면 아직도 셋업을 마치지 못했을 것입니다. 또한, 연구실 초기에 많은 도움을 주셨던 박수현 박사님께도 감사합니다. 그리고 연구실의 다른 멤버인 정훈이 형, 정수, 세계 에게도 고맙다는 말을 하고 싶습니다.

저희 부부의 새로운 시작을 함께해 주셨던 박제근 교수님께도 감사의 인사를 드립니다. 결혼식 주례 때, 교수님께서 말씀하신 내용을 지키려고 노력하는 과정에서 화목한 가정을 이룰 수 있었습니다.

다음으로 20대와 30대 초반의 청춘을 같이 보낸 저의 친구들에게도 고마움을 표시하고 싶습니다. 간단한 잡담부터 연구에 대한 이야기까지

많은 대화를 나누었던 물리학과 친구들, 짱구, 거북과 7년을 넘게 같이 살며 가족보다 많은 시간을 보낸 조랭과 대학 졸업하고 나서도 삶의 한 부분을 차지한 ISA 친구들, 아범, 현재에게 특히 고맙습니다. 그 외에도 선욱이 형, 애송, 피하, 주모, 호구, 진용, 찬용, 지강, 성대, 지현이 에게 감사의 말을 전하며 더불어 오랜 시간 함께 공을 차며 스트레스 해소에 도움을 주었던 자연대 축구부와 풋샤. 기존 프레셔 팀원들 에게도 고맙다는 말을 하고 싶습니다.

오랜 기간 제 밥 벌이도 못했던 저를 묵묵히 지원해주신 어머니, 아버지, 야무진 동생 지예와 착한 막내 동생 지석이 에게도 고맙다는 말을 전하고 싶습니다. 그리고 언제나 사위인 저를 아들처럼 아껴주시는 장모님, 장인 어른과 손위 처남인 태우 형님 에게도 감사하다는 말을 하고 싶습니다.

마지막으로, 저의 사랑하는 아내 태경이와 은호에게 고맙다는 말을 하려고 합니다. 어린 나이에 대학원생인 저를 만나고, 결혼해서 고생한 태경이 에게 고마움을 많이 느낍니다. 태경이가 기다리는 가정이 없었다면 힘든 대학원생활을 무사히 마치기 힘들었을 것입니다. 그리고 졸업 마지막 학기에 태어나 존재만으로도 아빠에게 힘을 준 우리 아들 은호 에게도 고맙다는 말을 하고 싶습니다.

또한, 여기에 담지 못한 많은 분들에게도 감사의 인사를 드립니다. 저의 물리학 박사 학위는 제가 혼자 노력하여 받은 것이 아닌 저의 주변 모든 사람의 도움으로 얻은 결과라고 생각하고 앞으로도 부족하지 않은 사람이 되도록 열심히 노력하겠습니다. 감사합니다.